Physik Department

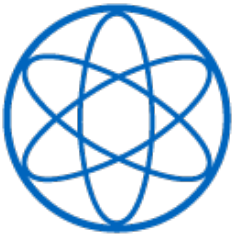

Accelerator Mass Spectrometry Relevant for Nuclear Waste Transmutation

Master‘s Thesis

by Karin Hain

October 2011

Technische Universität München

Abstract

Within the scope of this Master's thesis Accelerator Mass Spectrometry (AMS) was chosen for the detection of long-living fission products. For this purpose, two different approaches have been tested: at first, Time-of-Flight measurements using a passive absorber and additionally, experiments with the Gas-filled Analyzing Magnet System (GAMS) setup were done. In order to develop both techniques, the example of ^{93}Zr was used, the fission product which is most challenging for AMS, due to its isotopic and isobaric background.

In the first experiments with the GAMS the background was characterized and the suppression of the isobar ^{93}Nb was tested at varying gas pressures in the Gas-filled Magnet and in the ionization chamber, and at different energies of the ions. The best background suppression resulted in a detection limit of c(^{93}Zr)/c(Zr)=$3 \cdot 10^{-7}$.

The preparation of the experiment using the passive absorber included the choice of the material and the thickness of the passive absorber in order to achieve a maximal separation of ^{93}Zr and its isobar ^{93}Nb. For this purpose, simulations with SRIM03 and CORTEO were performed. The interpretation of the simulation results required an intensive study of energy loss and energy straggling theory. By the comparison of the stopping power curves for ^{93}Zr and ^{93}Nb in silicon nitride (SiN) and beryllium (Be) obtained from the simulations with those, which were calculated with the help of stopping power tables, a severe difference was discovered, having a considerable influence on the experimental conditions. Due to the shortcomings of the simulations, the optimal thickness of the absorber had to be determined experimentally.

In contrast to what was expected from the simulations, the experiment showed a much higher energy straggling when Be was used as passive absorber instead of SiN. Consequently, we were able to confirm the high degree of uniformity of SiN foils which lead to the better performance with regard to energy straggling. In order to determine the transmission of the setup, a standard sample of ZrF_4 with two different concentrations of ^{93}Zr was produced from an irradiated, metallic Zr plate with a defined concentration of ^{93}Zr which we had received from the Radiochemistry Munich (RCM). Due to a very unstable performance of the ion source caused by the Fluoride ions, no ^{93}Zr events from the standard sample could be detected. Therefore, a different method for the determination of the transmission was developed which is based on the ^{93}Nb concentration in the sample. From the measurements a ^{93}Nb concentration of (15.0 ± 8.3) ppm in ZrO_2 was deduced. With this information an upper detection limit of c(^{93}Zr)/c(Zr)=$6 \cdot 10^{-9}$ for the use of SiN foils as passive absorbers could be established. The current data suggest a stopping power curve as the one implemented in the simulation programs.

Contents

1. Introduction

One major argument which supporters of the immediate nuclear phaseout often put forward, are the extremely long storage times of radioactive waste until the activity has dropped considerably. Apart from other minor producers, such as medicine, military or research, the largest fraction of nuclear waste originates from nuclear power plants. Radioactive waste can be divided into three categories depending on the radioactivity: Low Level Waste (LLW), Intermediate Level Waste (ILW)and High Level Waste (HLW). Responsible for the long time-scales of more than 10^5 years [1] are ILW and LLW which produce only little heat, but have a very long half-life. Nuclear waste, which belongs to those two categories, presents only 1% of the overall radioactivity but 90% of the volume of the total accumulated waste [2]. Since every year 2500 t[1] of spent fuel accumulate in the EU [3], it is obvious, that solving the nuclear waste problem is one of the most challenging and urgent tasks of our days.

The problem of the already vigorously debated geologic repositories is that it is hardly possible to guarantee their safety on the required timescales. Furthermore, the majority of the population has serious concerns about final storage and incidents like in the repository 'Asse' [4], where final storage is tested, reduce the confidence in this procedure even further. Therefore, a number of institutes and cooperations around the world do research on the concept of 'Partioning and Transmutation', in order to decrease the timescales on which nuclear waste has to be isolated from the biosphere. This is to be achieved by converting the long-living isotopes into nuclei with shorter half-lives with the help of nuclear fission or neutron capture.

With this background, the "Bundesministerium für Bildung und Forschung" (BMBF) approved the joint research project "Transmutationsrelevante kernphysikalische Untersuchungen langlebiger Aktinide" (TRAKULA), in which several universities and institutes throughout Germany participate. In addition to the development of a Compton Camera, the Technische Universität München (TUM) has to demonstrate the feasibility of measuring small amounts of long-lived isotopes by Accelerator Mass Spectrometry (AMS) in order to be able to characterize the composition of the nuclear waste in the long run.

The complete characterization of the nuclear waste is essential for the process of trans-

[1] In 2003.

mutation, since the several components of the waste have to be separated radiochemically and the neutron spectrum has to be adjusted in order to obtain a maximum transmutation to isotopes with shorter half-lives either by neutron absorption or by fission. However, especially long-lived isotopes, which cause the main fraction of the long term radiotoxicity, are hard to detect by conventional methods such as decay counting. By contrast, the highly sensitive method of AMS does not depend on the half-life of the isotope, but simply counts the single ions which are present in the sample.

Aim of this Master's thesis was the development and testing of methods for AMS to be able to detect those long-living isotopes using the example of the abundant fission product ^{93}Zr, which was declared to have high priority for Transmutation Research (ch. 2). Regarding the background due to neighboring stable isotopes and isobars, ^{93}Zr is the most challenging isotope to be measured with AMS compared to other long-living fission products. Consequently, the successful approach in detecting ^{93}Zr can also be applied to other isotopes in this mass range, such as ^{99}Tc for example. The measurements were performed at the Maier-Leibnitz-Laboratory (MLL) of the Ludwigs-Maximilians-Universität and the Technische Universität München, where a complete setup for AMS is available. The ^{93}Zr samples were produced by neutron capture on ^{92}Zr at the Forschungsreaktor München II (FRMII).

After a short introduction to Transmutation Research (ch. 2), the general characteristics of Zirconium and the production ways of ^{93}Zr in a Nuclear Power Plant are explained (ch. 3). This is followed by a description of AMS and the present setup at the MLL (ch. 4). Then, the production of the standard samples is shown (ch. 5) and afterwards the two detection methods and the measurement are presented where the results are compared and discussed (ch. 6 and ch. 7). Finally, the findings of this Master Thesis are summarized and an outlook to future projects in using AMS as a tool for research in Nuclear Waste Transmutation is given (ch. 8).

2. Transmutation Research

This chapter shall give a motivation, why the characterization of the long-living isotopes, which are present in the nuclear waste, is necessary for transmutation. For that reason, a general, but short overview of transmutation is presented covering the questions: What is transmutation?, Why do we think, that we need transmutation? and How does it work?. Furthermore, it is to be shown, that only a few selected isotopes are considered to be transmutated in the near future, so that a complex partitioning process is needed which, in turn, requires a good knowledge of the components of the radioactive waste.

2.1. The Nuclear Waste Problem

Every year, 10500 tHM (tones of heavy metal [1]) [5] of spent fuels from Nuclear Power Plants (NPP) accumulate worldwide, which can be divided into High Level Waste (HLW) and Low Level Waste (LLW), where the latter represents around 90 % of the total volume. Although, 94.5 wt%[2] of the spent fuel is made up of Uranium with a concentration of 0.7 wt% of fissile ^{235}U [6], which could be separated and reused, only a few countries, such as France or Great Britain, operate reprocessing plants. Thus, the other nations have to store the complete amount of discharged spent fuel, if they cannot send their nuclear waste to the few existing reprocessing plants. At first, the waste is stored in temporary repositories which are often on-site and have a limited capacity. This means, that in certain cases the repositories are gradually running out of space. Thus, all countries using Nuclear Power have to find a final storage, where the waste is separated from the biosphere until its activity has decreased at least to the activity of the initial, natural Uranium ore. Fig. 2.1, in which the radiotoxity of several components of the nuclear waste depending on time is plotted, shows that this is the case after more than 10^5 years [7]. More pessimistic estimations even arrive at a timescale of more than 10^6 years, in which the waste must not have contact with the environment [6, 8].

From Fig. 2.1 it is obvious, that the Actinides and especially the transuranic elements (TRU), e.g. Plutonium, are responsible for the long-term radiotoxicity, whereas

[1] Contains all actinides and fission products, but not for example the Zirconium of the cladding of the fuel rods.

[2] wt%: weight percent.

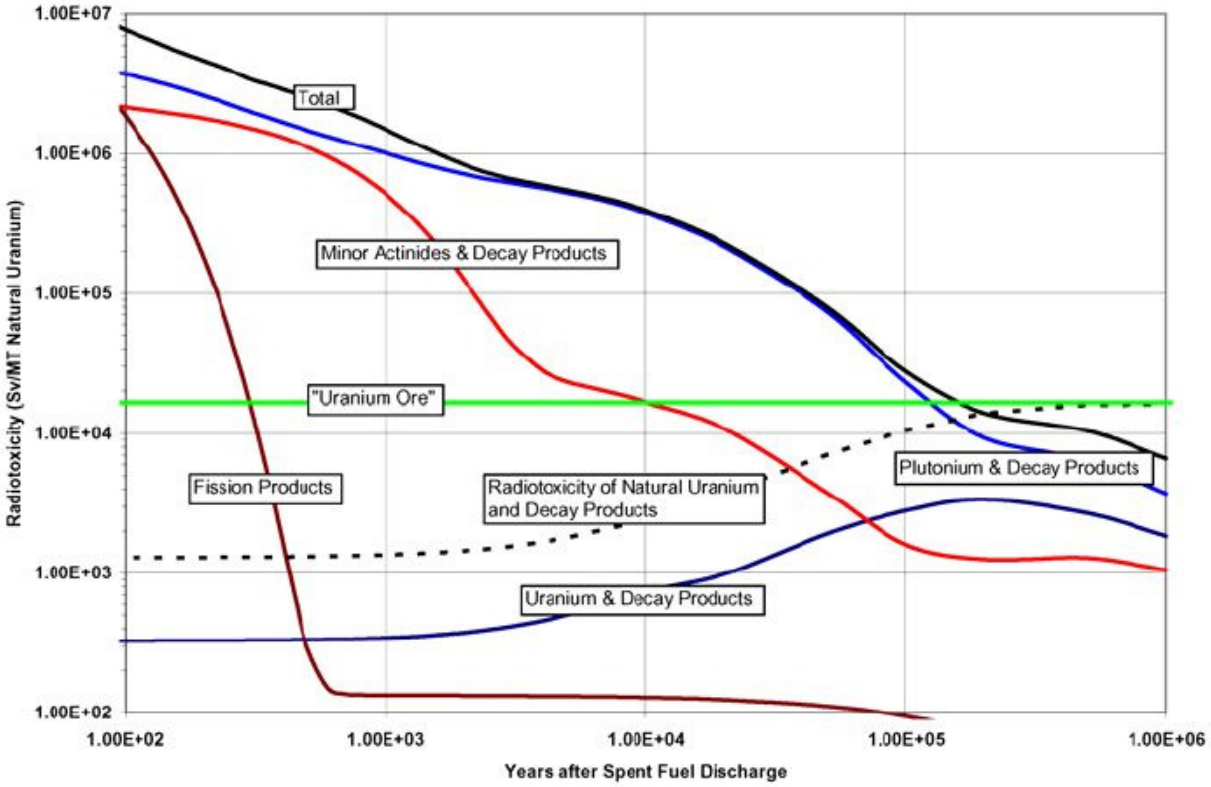

Figure 2.1.: Radiotoxicity of different components of the radioactive waste in comparison depending on the time after discharge from the Nuclear Power Plant. The long term radiotoxicity of the TRU are responsible for the storage times in the order of 10^5 to 10^6 years until the radioactivity has decayed to the magnitude of the Uranium ore. Source [7].

the fission produts (FP) decay rather quickly. However, there also exist long-living fission products in the radioactive waste, such as ^{129}I, ^{93}Zr or ^{99}Tc, which also have a half-life in the order of 10^6 years. Furthermore, some of those fission products, e.g. ^{129}I and ^{99}Tc, have a much higher mobility than the heavy actinides, so that there is a elevated risk that those isotopes leak from the containers and can reach the groundwater [3]. Therefore, it is essential to shorten the storage times of the nuclear waste in order to reduce the risk and the burden of future generations due to the radioactive waste originating from our present electricity production.

One possible solution for this problem, which is currently investigated by many different nations (amongst others China, Europe, Russia and USA [9–12]) is the transmutation of the long-living TRU and FP into isotopes with shorter half-lives, which is explained in the following section in more detail.

2.2. General Principle of Transmutation

Transmutation shall be achieved by neutron absorption in the case of the FP, and via fission in the case of the TRU, leading to a nuclide with a shorter half-life or even a stable isotope. In this way, the storage time shall be reduced by a factor of 100, to approximately 10^4 a [7], which would be an enormous progress in the radioactive waste management. Fig. 2.2 compares the time evolution of the radiotoxicity in case of direct storage with an expected, theoretical dose evolution after transmutation which clearly indicates a reduced dose in the second case.

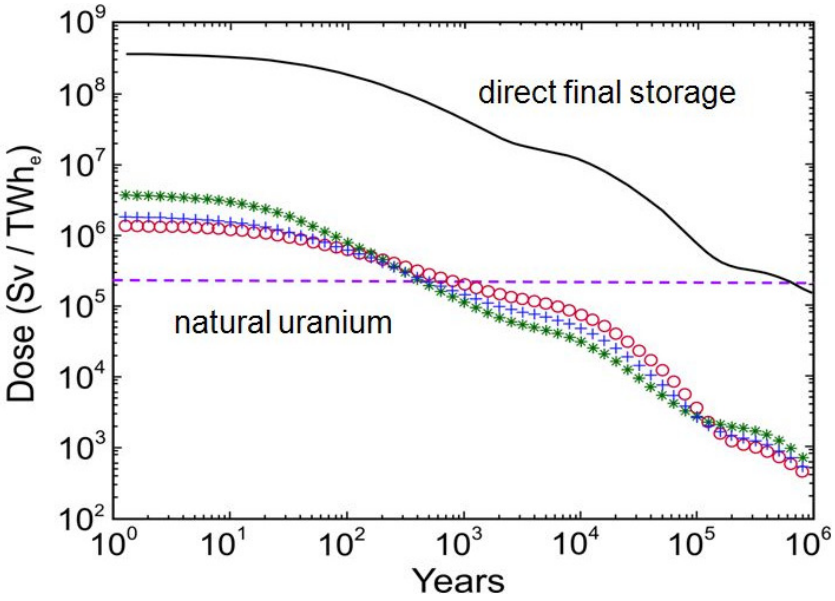

Figure 2.2.: Comparison of the time evolution of the radiotoxicity of nuclear waste directly stored after discharge on the one hand and of nuclear waste having been treated by transmutation. Different symbols represent different transmutation scenarios (compare text). Source [7].

The symbols in Fig. 2.2 represent different transmutation scenarios, since there is a multitude of different concepts concerning the technical realization of the transmutation process. A major distinction is drawn between the two most promising types of neutron sources in which the nuclear reactions for the conversion of the isotopes take place: a critical Fast Reactor (FR) or a sub-critical Accelerator Driven System (ADS). In both cases, a fast neutron spectrum has to be used to obtain a reasonable fission rate of the TRU [8], since most of the fission cross-sections for thermal neutrons are only in the order of 0.04 to 1 b[3]. In the case of ^{237}Np for example, the fission cross-section can be increased by a factor of 100 if fast neutrons are used [13, 14]. The FR uses a self-sustaining chain-reaction for the burning of the nuclear waste with several of the

[3]There are TRU, such as ^{239}Pu which have a high fission probability for thermal neutrons ($\sigma_f \approx 700b$).

inherent safety features of a thermal reactor not being implemented due to the missing moderator. By contrast, ADS is operated with an effective neutron multiplication factor (k_{eff}) which is smaller than one by construction. In general, k_{eff} is around 0.95-0.97 [1, 8], which means that there is no possibility for a nuclear runaway and a subsequent uncontrolled chain-reaction.

As it is obvious from the name, the ADS produces the neutrons necessary for the fission reactions in the core, by a proton beam which is accelerated to an energy of 1 GeV and then hits a target (usually Pb or Pb-Bi eutectic) from which neutrons are emitted via spallation processes. In the case of the ADS presented schematically in Fig. 2.3, the coolant of the reactor serves also as the target. Lead is reasonable as coolant, because neutrons which collide with this heavy nucleus loose only little of their initial velocity (energy and momentum conservation) and thus, the fast neutron spectrum can be maintained.

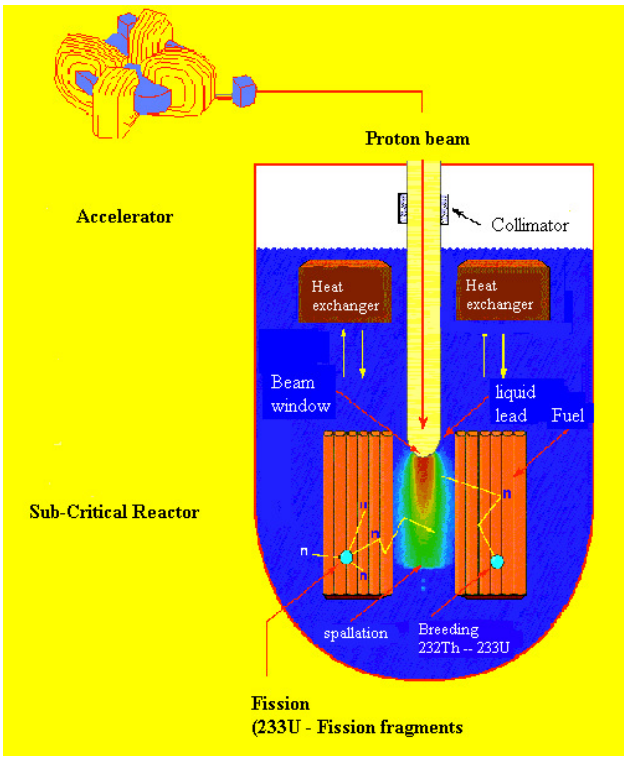

Figure 2.3.: Schematic of an accelerator driven system, which uses Pb as coolant and ^{233}U as fuel which is bred from the fertile material ^{232}Th by neutron absorption. Source [1].

The schematic in Fig. 2.3 shows the ADS design strongly supported by the EU by now, which was proposed by C.Rubbia in his work on the Energy Amplifier [15]. The basic concept of the Energy Amplifier was to use ^{232}Th/^{233}U as fuel which is needed as a startup for the system [8]. Of course, the major part of the energy should be provided by the burning of the nuclear waste, especially of the TRU, in order to make

the ADS also economically interesting. The ^{232}Th serves as fertile material from which the fissile ^{233}U is bred by neutron absorption. This idea is now also supported by the IAEA [16], since ^{233}U has the advantage that there is a larger mass difference to the Minor Actinides (MA) and TRU than in MOX (Mixed Oxide) fuel , which one actually wants to destroy in the ADS. Thus, there is a lower probability that those nuclides are built up by neutron absorption during the operation of the ADS, so that more TRU are destroyed than are produced. Furthermore, ^{232}Th has a large abundance in the earths crust [8], which means that it will be available for quite a period of time.

Since 99.995% of the long-lasting radiotoxicity is represented by only 1% of the spent fuel [8], it does not make sense to insert the whole radioactive waste into a transmutation system. By contrast, this could make things even worse as initially stable or short-lived nuclei may absorb neutrons in the transmutation reactor and thus also become long-lived nuclei increasing the long-living waste. To prevent this, the nuclides to be transmutated have to be carefully separated from the rest of the nuclear waste. However, since most of the separation processes are extremely complex, the transmutation of only a few nuclides have been given top priority. But which nuclides are most important and most promising for transmutation?

2.3. Candidates for Transmutation

The choice of the candidates for transmutation critically depends on the following characteristics: The radiotoxicity, the mobility, the feasibility of partitioning and fuel production from this isotope and the heat output. Partitioning here denotes the generalization of reprocessing in order to extract not only U and Pu from the nuclear waste but also to recover entirely the TRU and FP for transmutation. It is obvious from Fig. 2.1, that with regard to the overall radiotoxicity the most pressing nuclides to be transmutated are the TRU. However, the development of the partitioning processes in order to recover the most important TRU (Pu, Np, Am, Cm) is quite advanced. The extraction of U and Pu by the PUREX process [17] for example is a standard procedure, which is already applied in the reprocessing plants La Hague and Sellafield. Also the other TRU mentioned can be already recovered to about 99.5% [5] by methods which are already available such as the advanced PUREX process.

Thus, the rest of this section is dedicated to the FP since they turn out to be an elevated risk for the population, though the major part of it is decayed after 300 to 500 years. This is because of the already mentioned high mobility of those isotopes in geologic repositories. Some working groups also concentrate their attention on the short-lived FP ^{137}Cs, ^{90}Sr which are responsible to a large fraction of the heat output of the nuclear waste and Mo which decreases the durability of the vitrified HLW [18]. Both characteristics lead to a challenging situation with regard to the final disposal.

However, most efforts are made in order to investigate the feasibility of partitioning and transmutation (P&T) for the long-lived fission products (LLFP) ^{129}I, ^{99}Tc, ^{93}Zr, ^{135}Cs and the activation products ^{36}Cl ($T_{1/2} = 3.01 \cdot 10^5\,a$) and ^{14}C ($T_{1/2} = 5.7 \cdot 10^3\,a$). Tab. 2.1 gives an overview of the critical characteristics of the mentioned LLFP which have to be considered to estimate the risk for humans.

Isotope	**half-life (a)**	**mass (g/tUranium)**	**activity (Bq/tUranium)**
^{93}Zr	$1.6 \cdot 10^6$	1056	$9.8 \cdot 10^{10}$
^{99}Tc	$2.1 \cdot 10^5$	1115	$7.0 \cdot 10^{11}$
^{129}I	$1.7 \cdot 10^7$	263	$1.7 \cdot 10^9$
^{135}Cs	$2 \cdot 10^6$	531	$2.3 \cdot 10^{10}$

Table 2.1.: Half-life, accumulated amount and activity after 1000 years of decay time of the most important LLFP in spent fuel. Source [19].

The table shows that ^{93}Zr and ^{99}Tc represent the largest part of the LLFP in spent fuel, both regarding the accumulated mass and the activity. Although ^{129}I accumulates to a much lower extent than ^{93}Zr it has been given a higher priority for transmutation Research since similar to Technetium, Iodine is readily soluble in water whereas Zirconium is not. Consequently, there is an increased risk that atoms of those two isotopes reach the groundwater and thus the food chain if there is water penetrating into the final repository. Whereas there already exist highly developed partition schemes for ^{99}Tc and ^{129}I, the situation is much more complex for ^{93}Zr and ^{135}Cs. Both require an isotopic separation which is not available, yet. This is especially problematic for ^{135}Cs since it occurs in company with the very radioactive isotope ^{137}Cs ($T_{1/2} = 30\,a$) which makes the handling extremely difficult [5]. Since there is no partitioning process for ^{135}Cs available yet, this isotope is consequently not considered for transmutation at present. Conditions are a little bit different for the separation of ^{93}Zr which is discussed in the next section.

Summing up, P&T is reasonable and feasible only for a few selected LLFP. Due to the varying neutron absorption cross-sections of the different isotopes, a certain amount of the LLFP is left behind after one passage of the P&T process. In order to arrive at the goal of destroying at least 95% of the LLFP, the waste has to circulate through this P&T loop. Thus, the characterization of the complete radioactive waste, before and after each P&T step is essential. Especially after a run through the loop, an activity measurement to determine the remaining concentrations of the radioisotopes is not the optimal choice, as the long half-lives of the isotopes of interest lead to a rather low activity. Therefore, efforts are made to establish the activity-independent method of Accelerator Mass Spectrometry (AMS) to perform this task. This is also the case for the Germany-wide project TRAKULA (**tra**nsmutationsrelevante **k**ernphysikalische **U**ntersuchungen **l**anglebiger **A**ktinide) in which the TUM participates. One of the goals of this project is to show the feasibility of the detection of the LLFP by AMS using the example of ^{93}Zr which is explained in the following chapters.

3. Zirconium (Zr)

It was shown in the previous chapter that Zirconium is an essential component of the nuclear waste, since relatively large amounts of ^{93}Zr accumulate in a nuclear reactor. But what are the reasons for this high concentrations of Zr in general and what are the production paths of ^{93}Zr? This chapter shall give an overview of the most important characteristics of Zirconium which lead to the usage of Zirconium in nuclear engineering and to the high production rate in a reactor during operation. Furthermore, it has to be discussed why ^{93}Zr was chosen for the demonstration measurement with AMS although it is not the most pressing isotope regarding the radiotoxicity.

3.1. General Characteristics Zr

Zirconium, the 40th element of the periodic table, abbreviated by Zr, is a rather soft, ductile, lustrous silver-gray metal, which is remarkably heat and corrosion resistant [20]. Fig. 3.1 shows a photo of a metallic Zr rod. An overview of the most important physical characteristics is given in Tab. 3.1. Zr has 5 stable isotopes, with ^{90}Zr being the most abundant one, making up more than half of the total Zr resources.

Figure 3.1.: Photography of a metallic Zr rod. Source [21].

In nature, Zr appears most commonly as Zirconiumsilicate ($ZrSiO_4$) which is often referred to as zircon, or it can be mined as Zirconiumdioxide (ZrO_2). Both compounds are mechanically, thermally and chemically very resistant and thus are often utilized for

atomic number	40
atomic weight	91.224 amu
electronic configuration	$[Kr]4d^2 5s^2$
density	6.508 g/cm^3
melting T	2128 °C
boiling T	3578 °C
stable isotopes	^{90}Zr (51.45%) ^{91}Zr (11.22%) ^{92}Zr (17.15%) ^{94}Zr (17.38%) ^{96}Zr (2.80%)

Table 3.1.: Important characteristics of Zr. Source [20].

the production of chemical equipment [20]. Synthetically produced cubic ZrO_2 often serves as a cheap alternative for diamond in jewelry. Another remarkable property of ZrO_2 is its electrical conductivity at temperatures higher than 600°C [22]. Due to the electronic configuration given in Tab. 3.1, Zr frequently appears in compounds with the oxidation degree IV, but smaller oxidation degrees are also possible [20].

Elementary Zr is obtained from the reduction of ZrI_4 at high temperatures which is produced in the reaction of ZrO_2, I_2 and coal [20]:

$$ZrO_2 + 2\,I_2 + 2\,C \longrightarrow ZrI_4 + 2\,CO_2$$

Since Zr, especially Zr powder, can be easily oxidized back to an Oxide or a Nitride by the reaction with Oxygen and Nitrogen from air, Zr is often in use as getter material in getter pumps which are needed for high-vacuum installations. At normal pressure, the reaction of Zr powder with air can be violent leading to a spontaneous ignition of the Zr powder [23]. This reaction can be aggravated, if pressure is imposed upon the Zr powder. Thus Zr powder needs to be handled with care, particularly during the sample preparation for AMS, where the material is hammered into the holder (compare ch. 5&6). Until now, Zr and its salts are considered as non-toxic for humans, since most of the up taken Zr is eliminated from the human body without being absorbed, so that an accumulation of this heavy metal takes place only to a small extent [23, 24].

Zirconium cannot be dissolved by most of the usual solvents but is rapidly attacked by Hydrofluoric Acid (HF) and Aqua Regia, a mixture of concentrated hydrochloric acid and nitric acid at the ratio of 3:1. Besides, with a melting temperature of 2128°C Zr is extremely heat resistant and it has a thermal conductivity more than 30% higher than stainless steel [25]. These two characteristics and above all the very low absorption cross-section for thermal neutrons of 100 mb (90Zr) and 250 mb (^{92}Zr) [14] render Zr especially interesting for nuclear engineering in thermal NPPs, where as little neutrons

as possible may be lost. Thus, Zr is the main component of Zircaloy, a Zirconium alloy from which the fuel rod cladding of Nuclear Power Plants is made up. Apart from more than 95 % Zr, Zircaloy-2 which is widely used in Boiling Water Reactors, consists of the alloying materials Sn (1.5%), Fe (0.15%), Cr (0.1%) and Ni (0.05%). In Pressurized Water Reactors the cladding consists of Zircaloy-4, which has a similar composition as Zicaloy-2 but with Ni left out and an increased Fe content [25]. A huge disadvantage of Zr in nuclear industry is the reaction of hot Zr with water producing hydrogen:

$$\mathrm{Zr} + \mathrm{H_2O} \longrightarrow \mathrm{ZrO_2} + 2\,\mathrm{H_2}$$

In case of a so-called Loss-of-Coolant-Accident, where the cooling of the fuel rods cannot be sustained, the Zr cladding heats up, which leads to a high rate of the given reaction. Thus, hydrogen accumulates in the reactor causing an overpressure which may result in an explosion as it happened in the case of the Fukushima accident in spring 2011.

In spite of the small neutron absorption cross-sections, a certain percentage of the stable Zr in a NPP will be transmutated into radioactive nuclei by the irradiation with neutrons, with ^{95}Zr and ^{93}Zr being the two most important ones (compare Fig. 5.1). However, this is not the most important production way of radioactive Zr isotopes, which is then an essential component of the radioactive waste accumulated in a NPP. The second production way as well as the relevance of ^{93}Zr for the disposal of the nuclear waste is discussed in the next section. Since ^{95}Zr has a quite short half-live of $T_{1/2} = 65.5\,d$, it is highly radioactive indeed, but will have decayed to a negligible level while the fuel rods are stored in the spent fuel pool near the reactor core. Consequently, it does not pose a problem for the final storage in a geological repository and thus, has not to be considered for Transmutation.

3.2. ^{93}Zr: a long-living component of the Nuclear Waste

^{93}Zr has a half-life of $1.61 \cdot 10^6$a [26] and is therefore only weakly radioactive compared to most other isotopes if related to an unit mass. It decays via β^- emission:

$$^{93}\mathrm{Zr} \longrightarrow {}^{93\mathrm{m}}\mathrm{Nb} + \mathrm{e}^- + \overline{\nu}$$

with the metastable state ^{93m}Nb decaying by the isomeric transition

$$^{93\mathrm{m}}\mathrm{Nb} \longrightarrow {}^{93}\mathrm{Zr} + \gamma + 1.9\,\mathrm{keV}$$

Whereas the half-life of ^{93}Zr given in both pictures of Fig. 3.2 and the value stated above deviate only negligibly from each other, the branching ratio of a β^- decay to ^{93m}Nb compared to a direct decay to ^{93}Nb of formerly $(97.5 \pm 2.5\%)$ had been revised in a recent publication. The authors indicate a considerably lower branching ratio of $(73 \pm 6\%)$ [27]. The corresponding decay schemes are given in Fig. 3.2. This discrepancy, however, is of no concern for the present work.

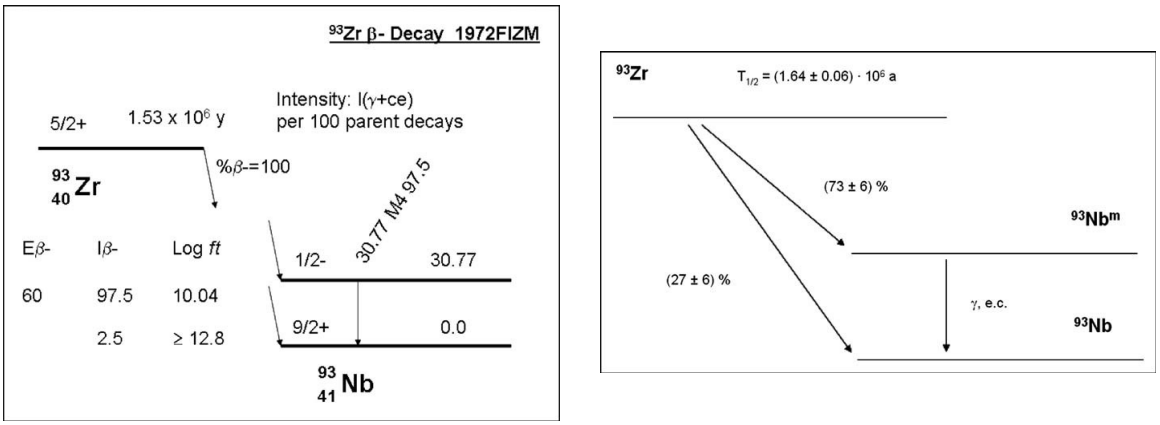

Figure 3.2.: Left: Decay scheme of ^{93}Zr presented in Nuclear Data Sheet 1997 by Argonne National Laboratory (ANL). Right: Decay scheme of ^{93}Zr published in 2010. Source [27].

In nature, ^{93}Zr occurs only in traces, mainly originating from nuclear fallout. However, it can also be present in the soil near NPPs and reprocessing plants [28], as it is accumulated in the radioactive waste to a rather high extent.

There are in general two production ways of this nuclide in a nuclear reactor: The neutron absorption of ^{92}Zr which is present in the Zircaloy cladding of the fuel rods (compare ch. 4.1) and directly by fission of ^{235}U. Due to the low cross-section of only 0.25 b for the reaction $^{92}Zr(n,\gamma)^{93}$Zr, the reaction rate caused by absorption is rather low. However, since large amounts of Zr are installed in NPPs, the ^{93}Zr produced in this way is considerably large.

The significant fraction of ^{93}Zr in nuclear waste can be found in the spent fuel. The fission yield of ^{93}Zr from the fission of ^{235}U is around 6 % and thus relatively high compared to that of ^{129}I (0.71 %) [29]. The reason for the high yield is the asymmetric fission of ^{235}U in a lighter and a heavier fragment leading to two maxima in the mass distribution of the fission products. This is represented graphically by the plot in Fig. 3.3 where the fission yield depending on the mass of the FP is shown. ^{93}Zr as well as ^{99}Tc are apparently located in the maximum of the lighter fragement whereas ^{129}I has a mass below the second maximum.

Although the produced amount of ^{99}Tc is even larger than that of ^{93}Zr (compare Tab 2.1), the elementary ratio of Zr and Tc is the other way round: 11.54 % of all

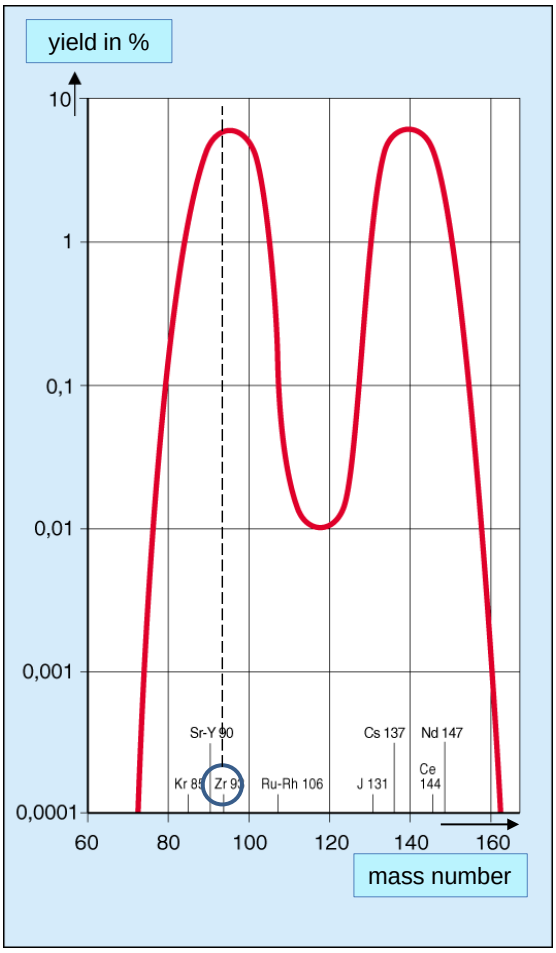

Figure 3.3.: Mass distribution of the Fission Products from the thermal fission of ^{235}U. Source [30], modified.

fission products after 1000 a of decay is Zr whereas Tc accounts for only 2.15 % [19]. This reveals an enormous difficulty which is associated with the P&T of ^{93}Zr: This isotope is always accompanied by a large quantity of stable Zr which means that an isotopic separation process is necessary. The ^{93}Zr/Zr ratio becomes even more unfavourable, if the Zircaloy is considered, where the ^{93}Zr atoms are embedded in an almost entirely stable Zr matrix. Therefore, this obstacle of developing an applicable partitioning process has to be overcome before the Transmutation of ^{93}Zr can be tackled. Along with the low mobility of ^{93}Zr this is the reason why the Transmutation of ^{93}Zr is deferred.

However, ^{93}Zr was chosen by the TRAKULA project to show, that Accelerator Mass Spectroscopy is able to measure even small concentrations of this isotope in relation to stable Zr. This choice was determined to a lesser extent by the importance of this isotope for Transmutation than by the challenges it poses to the methodology of AMS. The difficulty of detecting ^{93}Zr is that it is surrounded by two stable isotopes and one

stable isobar (^{93}Nb) which cause an increased background during the measurements with AMS. Consequently, a methodology developed for the detection of ^{93}Zr, can easily be applied to the other LLFP which were mentioned previously, since demands on the setup are not that high for those isotopes. A more detailed explanation will be given in the next chapter.

3.3. Further applications of ^{93}Zr

Apart from the importance of the detection of ^{93}Zr for Transmutation Research, the development of a method to detect smallest concentrations of ^{93}Zr is also relevant for environmental aspects, i.e. the tracing of the North Atlantic Current and for a better understanding of the stellar nucleosynthesis in Astrophysics.

3.3.1. Seacurrent Tracing

Several publications claim to have observed a weakening of the North Atlantic Current as a consequence of the present climate change [31, 32]. This could be confirmed experimentally by using long-living radioisotopes such as ^{93}Zr, ^{99}Tc and ^{129}I emitted into the sea by the reprocessing plants La Hague (France) and Sellafield (Great Britain) as tracers. This is possible because the emission pattern of the two reprocessing plants are very well known and the change in concentration due to radioactive decay is negligible. Thus, peaks in the emission such as that of ^{99}Tc in the case of Sellafield in the late 1990s [33] can be traced over several decades. To diminish uncertainties because of mixing of the water it is more reasonable to measure a ratio of two radioisotopes such as ^{99}Tc/^{93}Zr instead of the ratio ^{93}Zr/Zr. Regarding the low activity and concentrations in the sea water of those isotopes, AMS lends itself to determine those concentrations. If conventional methods such as decay counting are used instead, large quantities of seawater (80-100 liters) [33] have to be gathered for each measuring point to obtain sufficient statistics. With AMS this could be reduced to 1 liter per measuring point, which means, that more samples could be taken from different positions in the sea, thus, improving the data on the dispersion of the radioisotopes. Therefore a method for AMS in order to detect low concentrations of ^{93}Zr and with it, of ^{99}Tc has to be established.

3.3.2. Astrophysics

Elements heavier than iron are not built up by stellar burning but predominantly by neutron capture processes, i.e. by the so-called s- and r-process, where 's' denotes slow

and 'r' rapid. This means, that in the first case the neutron capture happens quite slowly, so that a large fraction of the nuclei has decayed via β^- emission before another neutron is captured. Consequently, the s-process closely follows the valley of stability which is indicated in Fig. 3.4 by the solid red arrow. By contrast, in the r-process an additional neutron is captured with a high probability before the nuclide has decayed. Thus, very neutron rich nuclei far away from the valley of stability can be built up. However, for the neutron capture to happen very fast, a high neutron density and high temperatures are required. Therefore, the r-process is believed to take place primarily in supernovae, whereas for the s-process more moderate environments are sufficient, like in the He-core or C-shell burning of massive stars or the Asymptotic Giant Branch (AGB) phase of low- and intermediate mass stars.

^{93}Zr, however, has a half-life which is comparable to the timescales of the s-process, so that nucleosynthesis either follows the successive neutron capture to ^{94}Zr or the β^- decay to ^{93}Nb, which is demonstrated in Fig. 3.4. Thus, ^{93}Zr is referred to as (weak) branching point. As a consequence, the s-process has a small contribution to the production of nuclides which are predominantly built up by the p-process[1], e.g. ^{94}Mo. In order to predict the production rates of those isotopes in the stars correctly, it is essential to know the $^{92}Zr(n,\gamma)^{93}Zr$ cross section. However, there are considerable discrepancies in the experimentally determined cross sections of this reaction where the method of choice was activation and successive TOF measurements [34]. A complementary investigation of this cross section by AMS is therefore recommendable to obtain a result which is independent from the TOF measurements.

[1]Nucleosynthesis process which builds up the proton rich nuclei.

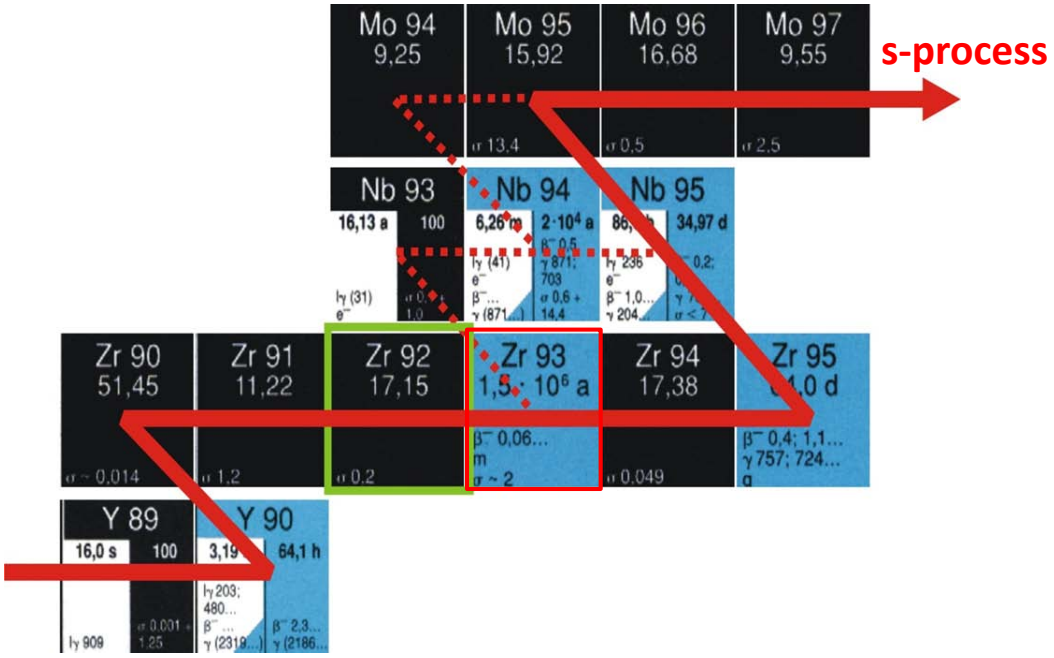

Figure 3.4.: Path of the s-process in the Zirconium region (solid red arrow). Despite the long half-life of ^{93}Zr, a small fraction decays to ^{93}Nb and thus opening a second branch of the s-process. Source [35], modified.

4. Accelerator Mass Spectrometry (AMS)

4.1. Introduction to AMS

AMS is an ultra-sensitive method to detect small concentrations of not necessarily radioactive isotopes. To determine the concentration of isotopes with short half-lives, activity counting is the detection method of choice. It has the advantage, that it is a cheap and simple method which does not need a large setup containing an accelerator. However, the activity of isotopes with half-lives in the order of thousands of years is accordingly low, which limits the application of this detection method. By contrast, AMS does not detect the decay products of the isotope of interest but directly counts the ions itself. In addition to each measurement of the radioisotope, the current of a macroscopically occurring isotope is also recorded, to which the events corresponding to the radioisotope in the detector are normalized. Thus, a concentration of the radioisotope in the sample is obtained which is independent of the measuring time. In this way, concentrations down to $N_{\mathrm{rad}}/N_{\mathrm{stable}} \approx 10^{-16}$ as in the case of ^{60}Fe/Fe, can be detected [36].

Similar to usual mass spectrometry (MS), AMS uses different electrical and magnetic components to filter or to suppress the interfering background. One main difference to MS is the energy of the ions, which is around several MeV in AMS compared to only keVs in the case of MS. The high energies of AMS enable the separation of ions with an identical mass [37] in the first place. Whereas first AMS test measurements in the 1970s used a cyclotron (Berkeley) for the acceleration of the ions, subsequent experiments dedicated to ^{14}C dating showed the superiority of electrostatic Tandem Accelerators [38]. The use of this type of accelerator leads to efficient suppression of the molecular background (compare ch.4.2.2) and thus, an even higher sensitivity is achieved. Furthermore, the extraction of single negatively charged ions from the ion source leads in some cases (e.g.^{14}C) to an additional suppression of background, since not all atoms form negative ions (e.g.^{14}N). Consequently, AMS has the advantage for longer lived radioisotopes that often less sample material has to be employed which can be investigated in a shorter time compared to MS or decay counting [38].

Though ^{14}C dating remained the driving force for the fast development of AMS, this technique was then also successfully applied to other isotopes. The isotopes already detected by AMS until now are marked in Fig. 4.1 which plots the half-life depending on the mass of the isotopes. The different colours represent different eras in the development of AMS, starting with the light isotopes of ^{10}Be, ^{26}Al, ^{36}Cl apart from ^{14}C. Whereas ^{14}C is attaining an increasing relevance in the field of biomedicine and environmental science [38], the other three isotopes have a great importance for geophysics. Their concentration in rocks, for example, contains useful information about the timescale the rocks were exposed to cosmic radiation and thus were uncovered (e.g. by a glacier). More recently, methods were developed to measure also Actinides by AMS which are marked in blue in Fig.4.1. The determination of the relevant cross sections enables us to gain insight into nucleosynthesis processes of heavy nuclides in stars and especially supernovae. Furthermore, the detection of Actinides is also relevant for the observation of emissions of nuclear facilities and for transmutation research (see ch. 1).

Since the beginnings in the late '70s, AMS has been applied to many different scientific problems [1] but with an increasing relevance for environmental science. As an example the detection of ^{14}C in atmospheric science can be mentioned, which is used to study CO_2, CO or CH_4 production rates in the atmosphere in order to comprehend the reasons for the climate change [37]. Another field of application is the investigation of possible consequences of the climate change, as for example expected effects on the sea currents. As already mentioned (see ch. 3.3.1), ^{93}Zr would be suited for this task, apart from ^{129}I. However, Fig. 4.1 shows that ^{93}Zr has not been successfully measured, yet, owing to the challenges it poses to AMS. Therefore, changes to a conventional AMS setup, as it is presented in the next chapter by using the example of the setup at the MLL, had to be tested within the scope of this Master's Thesis.

4.2. Setup at the Maier-Leibnitz-Laboratory (MLL)

An overview of the complete AMS setup at the MLL is given in Fig. 4.2. The ions have to pass several mass and velocity filters in order to get rid of the background which are magnetic and/or electric. Furthermore, the beamline is equipped with several Faraday cups to measure the ion current and hence, to monitor the guiding and focusing of the beam, which is done by several dipole and quadrupole lenses.
The following sections describe the different components and the beam guiding system in more detail.

[1] An extensive discussion of the applications of AMS can be found in [37].

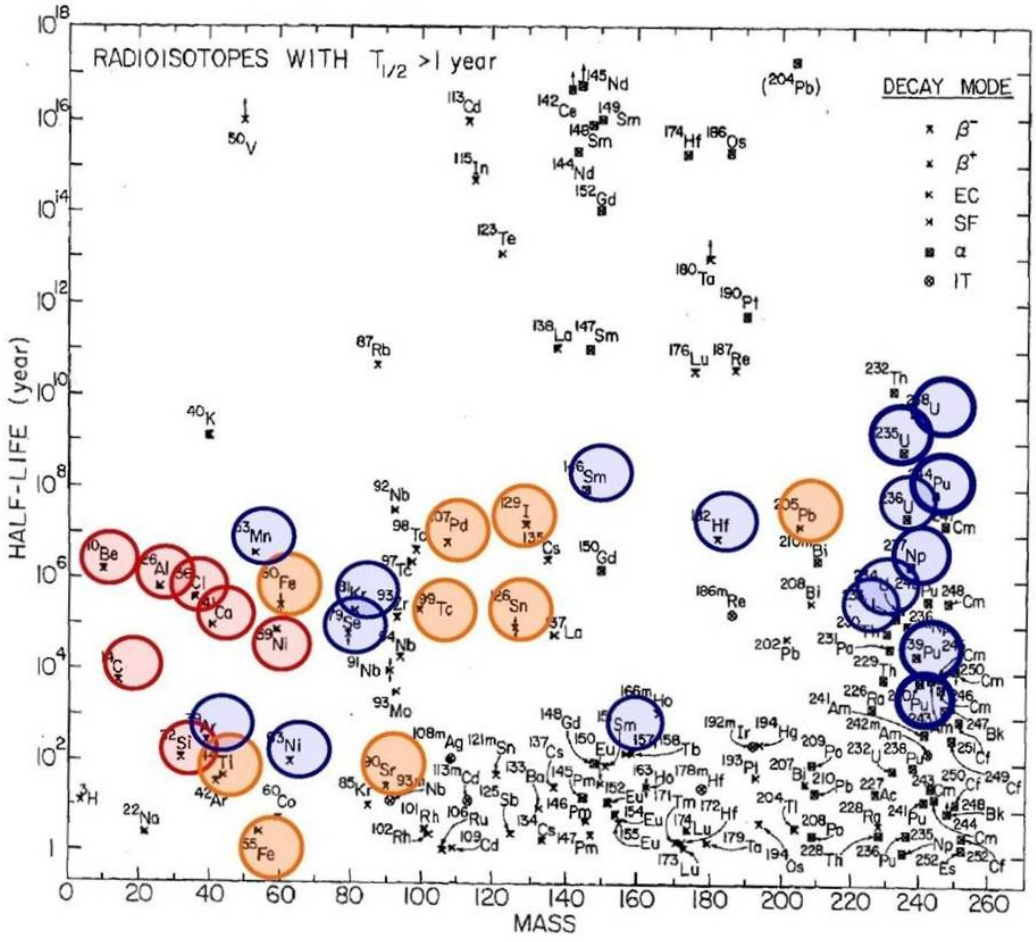

Figure 4.1.: Diagram showing various isotopes which are plotted depending on their mass and their half-life. The isotopes already studied by AMS are highlighted by coloured circles. The three colours represent different eras in the history of AMS. Red: detected until 1981, orange: detected until 1996, Blue: detected until 2008. Source [39].

4.2.1. Low Energy Components

The section of the beamline which is located in front of the accelerator is referred to as low energy side. The two most important components in this section are the ion source on the one hand and the Injection Magnet on the other hand.

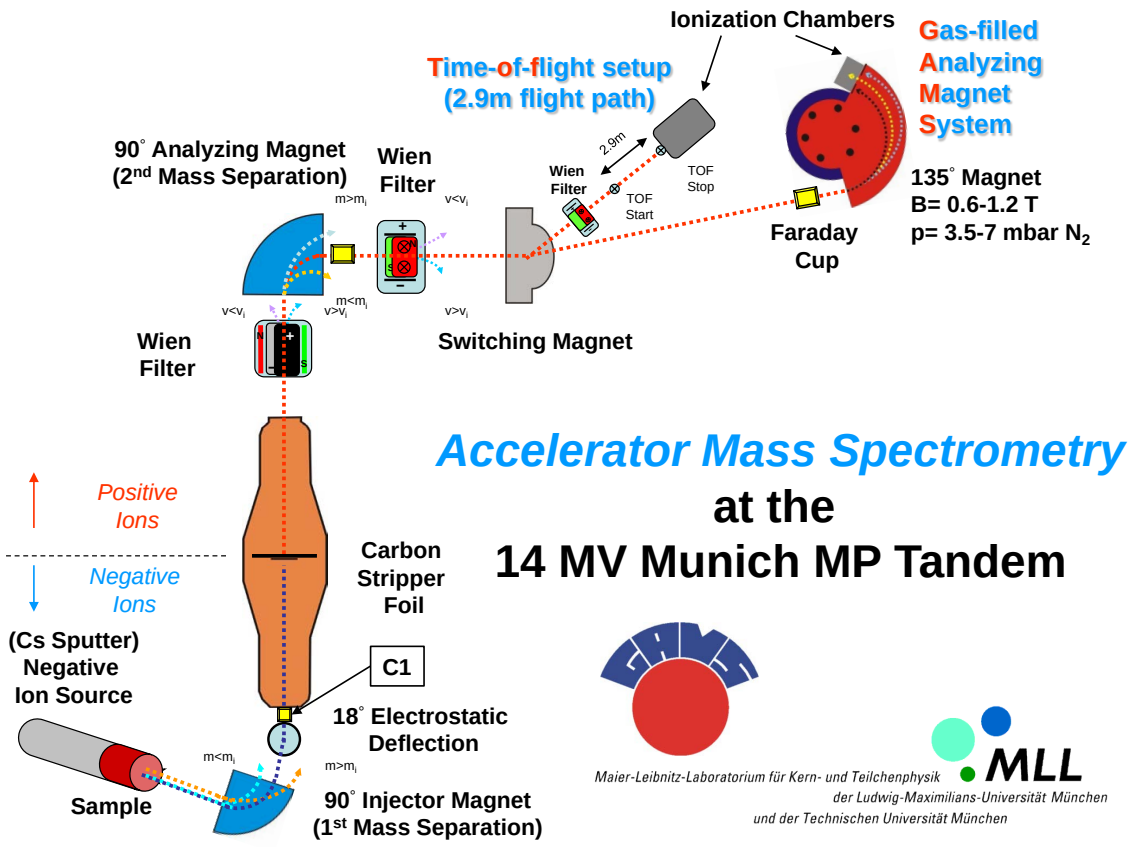

Figure 4.2.: Schematical drawing of the AMS setup at the MLL.

Ion source

To produce single charged ions from the sample material, a modified negative ion source of the Middleton type [40, 41] is used, whose schematic setup is presented in Fig.4.3. In the source, positively charged Cs ions sputter ions, atoms and molecules from the sample. The sample material, which has been chemically prepared if necessary, is hammered into the sample holder and placed into the ion source. To increase the thermal and electrical conductivity, the material is usually mixed with Ag or Cu powder with a volume ratio of 1:1. In order to sputter material from the samples the cesium reservoir has to be heated, so that Cs evaporates and arrives at the spherical ionizer. There, the Cs atoms are ionized at the approximately 1000°C hot Tantalum surface of the Ionizer. Besides, Cs atoms are deposited on the water cooled sample surface, so that a Cs layer on the sample is formed. The Cs^+ ions are then accelerated onto the sample surface by a voltage of 6 kV. The resulting kinetic energy is sufficient to knock out single ions, but also metallic clusters or molecules from the sample material. The sputter products may be positively or negatively charged, but the majority of the particles will be neutral. However, the produced ions have to cross the layer of Cs which has a very

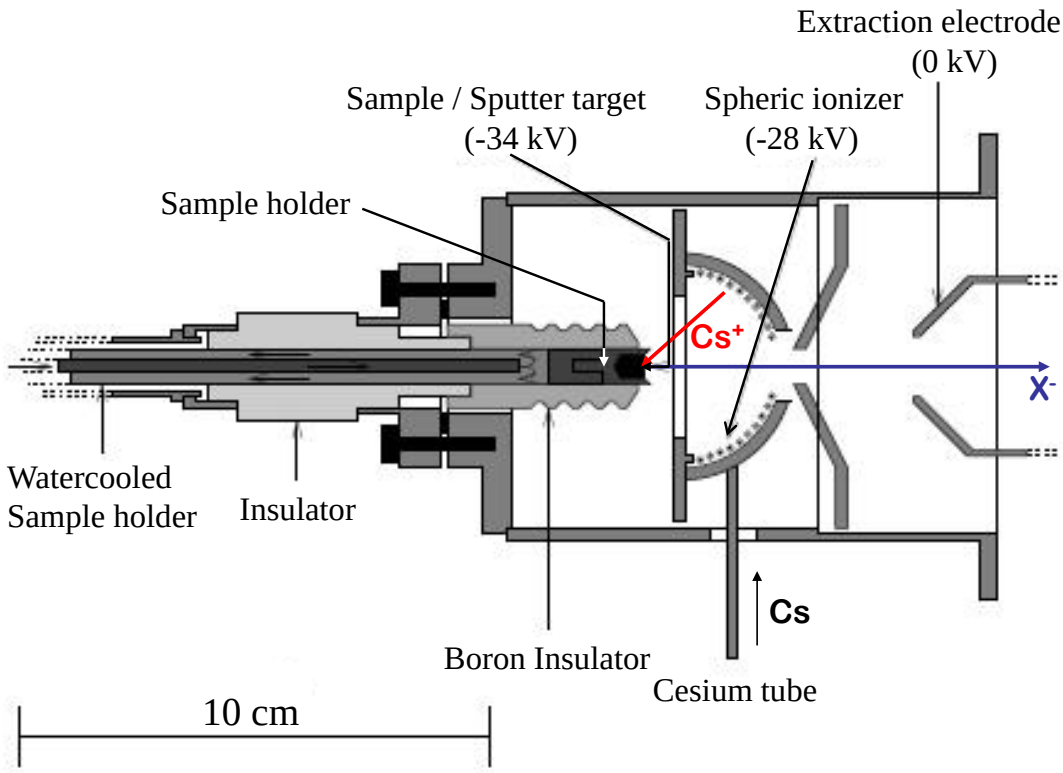

Figure 4.3.: Schematical drawing of the negative ion source used for the AMS measurements. X^- denotes all negative sputter products, accelerated out of the source. A description of the sputtering process is given in the text. Source [42], modified.

low work function. Hence, Cs tends to donate electrons to the sputter products, causing a higher yield of negative ions/molecules which increases the overall efficiency of the ion source. Those particles which are now single negatively charged are then extracted by a voltage of 28 kV and subsequently enter the Injector magnet. By contrast, owing to the electric potentials, positive ions cannot leave the source and therefore remain available for further sputtering and charge transfer processes. Neutral atoms or molecules, which are sputtered off the sample holder are lost from the experiment.

In order to increase the produced particle current, it is sometimes much more convenient to extract a single negatively charged molecule of the isotope of interest instead of using the atomic ion. For instance, preliminary measurements have shown, that the current of $^{92}Zr^-$ is in the order of only 0.04 nA whereas currents of around 30 nA were obtained by using $^{92}ZrF_5$.

The Injector Magnet

The Injector Magnet is a 90° dipole magnet, which acts as a first mass spectrometer selecting only the interesting mass. When the single negatively charged ions enter the magnet with a defined energy of 34 keV, they get bend by the Lorentz force. When the equilibrium of Lorentz- and Centrifugal force is reached, the ions move on circular trajectories with radius r. According to the magnetic rigidity

$$B \cdot r = \frac{\sqrt{2mE}}{q} \tag{4.1}$$

with B being the magnetic field, q the charge (for single negatively charged ions: q is equal to e = $1.602 \cdot 10^{-19}$As) and m the mass of the ion, the radius variies only with the mass for a given magnetic field, since q and E are fixed. Thus, by adjusting the magnetic field, only the ions of interesting mass (e.g. m=109 for $^{93}ZrO^-$) will be transmitted to a 18° electrostatic deflector (see Fig. 4.2. This is a capacitor which guides the ions onto the beam axis of the accelerator to a short pre-acceleration stage of 150 kV.

However, one has to keep in mind, that at this point of the separation process, any background with a identical mass is still present. Thus, if the magnet is set to $^{93}ZrO^-$, also ions, molecules and metal cluster with the same mass, e.g. ^{109}Ag, can pass the magnet. Furthermore, the system consisting of ion source, extraction and Injector Magnet has a certain limited mass resolution which means that it is not possible to select exactly one mass, but a Gaussian mass distribution with a certain full width half maximum (FWHM) is transmitted. Hence, the mass resolution of the magnet is approximately

$$\frac{\Delta m}{m} = 2 \cdot \frac{\Delta B}{B} \geq 1/400 \tag{4.2}$$

4.2.2. The Tandem Accelerator

After the pre-accelerating, the negative ions are injected into the Tandem accelerator which is a 14 MV Van-de-Graff Accelerator. The high voltage required to accelerate the ions/molecules is generated by charges which are transported to the central terminal by chains. In the terminal, which is located in the middle of the tank, the ions have to transverse a thin carbon foil with a surface density of $4\,\mu g/cm^2$. The advantage of a Tandem accelerator is, that the applied voltage can be used twice since negative ions are accelerated in the direction of the terminal, where a certain number of their electrons are stripped off in the carbon foil, so that the now positively charged ions are accelerated a second time. Additionally, the molecular bondings are cracked due to the stripping process which leads to a complete suppression of the molecular background, which is one of the important advantages of AMS compared to conventional MS.

The final energy of the ions depends on their charge state after the stripping process. The description of the responsible collision processes and the charge distribution itself after passing the foil, is not a trivial question (see also ch.7.1). However, the average charge state of heavy ions can be approximated by applying the Bohr's Criterion. It states, that there is a high probability that electrons with a orbital velocity smaller than the velocity of the ion get lost from the ion in consequence of the collisions with target atoms [43]. Though, one has to be aware of the limited validity of the Bohr criterion, so that $\bar{q}$ is often overestimated. For the general case of molecules arriving at the terminal the final energy E_f of the ions can be calculated as

$$E_f = \frac{m_{ion}}{m_{molecule}} \cdot E_{PA} + \left(\frac{m_{ion}}{m_{molecule}} + q \right) \cdot e \cdot U_T \tag{4.3}$$

with
U_T: Terminal voltage
E_{PA}: Energy of ions after the pre-acceleration stage.
q: chosen charge state

Equation (4.3) demonstrates, that the final energy of the ion decreases with increasing mass of the injected molecule. As a consequence of this, $^{93}Zr^-$ ions originating from $^{93}ZrF_5^-$ will have a lower energy after the accelerator than ions which were produced directly from metallic Zirconium for a given terminal voltage. However, especially for heavy ions with isobaric background, it is very important to obtain high energies with the accelerator in order to arrive at a maximal separation of the radioisotope and its isobar (sect. 4.2.4). Therefore, the mass and the number of ligands should be kept as low as possible. Additionally, the charge states of 15^+ or 16^+ were chosen to further increase the energy of the ions, even if the theoretically calculated yields are very low, e.g. for 15^+ only 0.63% in the case of $^{94}ZrF^-$ at a terminal voltage of 11.96 MV.

Behind the accelerator, another 90° dipole magnet, the so-called Analyzing magnet, is located. Similar to the Injector magnet, the magnetic rigidity $B \cdot r$ of the Analyzing magnet determines the ratio of the momentum of the ions over their charge p/q, that can be transmitted (compare equation (4.1)). This means, that for a given mass the charge state is chosen with the magnet. In general, the magnetic rigidity is kept, if the setup has to be changed from one isotope to another with the exception of the Injector Magnet which, apart from the electric fields of the Wien filter and the terminal voltage has to be adjusted accordingly.

4.2.3. Wien filter

To get rid of isotopic background with the same magnetic rigidity as the selected isotop, we are using several Wien filter. A Wien filter (WF) is a velocity filter which uses a magnetic and a perpendicular electric field. In total three of them are installed at

the AMS setup as can be seen in Fig. 4.2: two before the switching magnet (WFI + WFII) and a third one (WFIII) was installed in the actinide beamline in the course of a Diploma thesis [44]. Along with a photograph of WFIII, the working principle of a

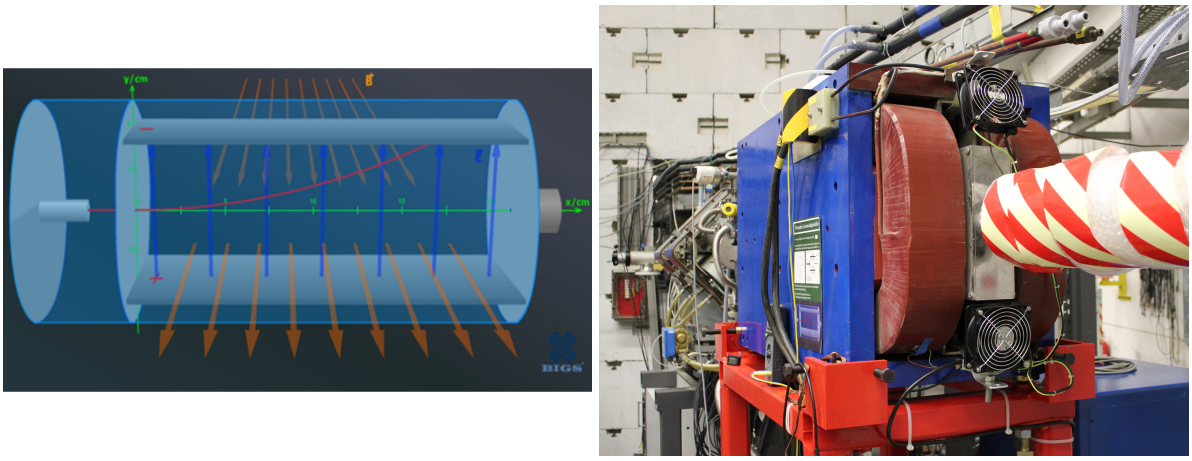

Figure 4.4.: Working principle of a Wien filter, whith the shown red path corresponding to a particle whose velocity does not match the ratio of electric and magnetic field, so that it gets deflected (left). Picture of the recently in the Actinide beamline installed Wien filter (right). Source [44].

Wien filter is demonstrated in Fig. 4.4. Only isotopes with a velocity v, which fulfill the following equilibrium condition

$$q \cdot v \cdot B = q \cdot E \tag{4.4}$$

can go straight through the Wien filter and pass the slit at the end of the filter. Ions with a different velocity are deflected and thus cannot pass the filter.

The following table, Tab. 4.1, gives an overview of the mass resolutions of the three Wien filter, which were determined within the frame of the work by maximizing the current. However, these values also depend on the position of the slits behind each

WF	$\Delta M/M$
I	1/34
II	1/8
III	1/113

Table 4.1.: Resolution of the Wien filter installed at the AMS setup

WF which is a possible explanation for the unusually low resolution of WFI and WFII. Characteristic resolutions of WFI and WFII are 1/65 and 1/45, respectively.

4.2.4. GAMS beamline

Depending on whether there is stable isobaric background expected or not, the beam is either guided to the Gas-filled Analyzing Magnet System (GAMS) detection system or to the Actinide beamline, which is equipped with a Time of Flight (TOF) path and a gas ionization chamber. Since there is a stable isobar in the case of ^{93}Zr, namely ^{93}Nb, the GAMS setup was used for the detection of Zirconium in the first place. The two main components of this beamline is a Gas-filled analyzing Magnet (GFM) on the one hand and a gas ionization chamber on the other hand. Additionally, a TOF path in front of the GFM using two microchannel plates (compare ch. 4.2.5) as start and stop detectors can be added if it is required.

Gas-filled Analyzing Magnet

The challenge of the separation of two isobars is, that they have the same p/q ratio and hence, cannot be filtered out by a usual mass spectrometer or velocity filters. The idea of the gas-filled magnet is, that an average charge state depending on the atomic number of the ion will be obtained due to collisions with the atoms or molecules of the gas in the magnet. Accordingly, the average charge state of the radioisotope and its isobar will be different so that the deflection in the magnetic field will also differ which leads to a spatial separation. The separation process is demonstrated schematically on the left side of Fig. 4.5. If the magnetic is adjusted correctly, only ions of the radioisotope have the appropriate radius to pass the slit at the exit of the GFM whereas ions of the isobar cannot enter the ionization chamber. This is, of course, an idealized consideration. In the experiment, an intensity distribution can be expected, so that the isobaric background cannot be suppressed completely. Nevertheless, the reduction of the isobaric count rate in the ionization chamber is a major advantage of the GFM. In this way, the currents from the source and thus the count rate of the radioisotope can be increased considerably before we risk a break down of the ionization chamber because of a count rate higher than 2 kHz. The right picture of Fig. 4.5 shows a photograph of the GAMS setup. At the MLL, a 135° dipole magnet with a maximal field of 1.25 T is used, whose magnet chamber is filled with several mbar of nitrogen. The gas volume is separated from the vacuum in the beamline by a 0.9 μm thick Mylar foil. Theoretically, the average charge state $\overline{q}$ can be estimated by the previously mentioned Bohr's Criterion (see ch. 4.2.2) resulting in the following dependency on the atomic number of the projectile Z_P and its velocity v_P [43]:

$$\overline{q} = \frac{v_P \cdot {Z_P}^{1/3}}{v_0} \tag{4.5}$$

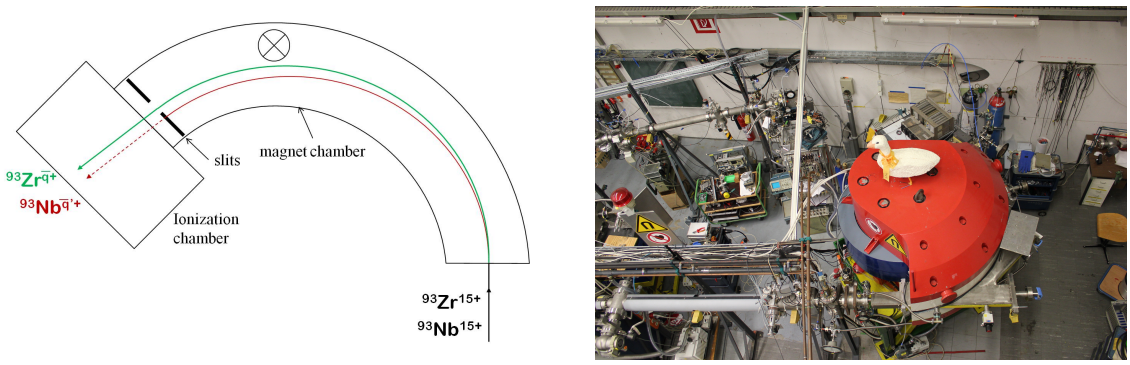

Figure 4.5.: Trajectories of the two isobars ^{93}Zr and ^{93}Nb in a gas-filled magnet (left). Top view of the GAMS magnet and the Actinide beamline in the background (right).

with

$$v_0 = \frac{e^2}{\hbar} \tag{4.6}$$

where v_0 denotes the Bohr velocity and $\hbar = h/2\pi$ with h being Planck's constant. A quite precise possibility to calculate the expected charge state is the use of the semi-empirical formula of Sayer [45] for a dilute gas:

$$\overline{q} = Z_P \cdot (1 - 1.08 \cdot e^{-(80.1 Z_P^{-0.506} \beta^{0.996})}) \tag{4.7}$$

with β being equal to v_P/c where c=$3.0 \cdot 10^8$m/s denotes the speed of light.

With the result from this formula, the magnetic rigidity $B \cdot \rho$ of the respective isotopes can be obtained, as it was done for ^{93}Zr and ^{93}Nb which is plotted depending on the initial energy of the ions in Fig. 4.6. The lower average charge state of ^{93}Zr leads to a higher magnetic rigidity. The difference in magnetic rigidity, which increases only very weakly with the energy in this case, is a measure for the separation of the two isobars by the magnet. Consequently, only a small improvement of the separation in the magnet can be achieved by choosing higher initial energies of the ions.

However, it has to be mentioned that the previous considerations do not include the width of the resulting gaussian intensity distribution which causes a worse resolution. Depending on the initial energy, the type and pressure of the gas in the magnet (typically 4-5 mbar) and the charge changing cross-sections the peaks are broadened which makes it more difficult to distinguish between the two isobars. But tuning one of these parameters in order to minimize the peak width after the GFM may cause a worse separation of the signals in the detector. For example: On the one hand, increasing the pressure in the magnet, in order to increase the number of collisions and thus decrease large fluctuations in the charge state is one possibility to reduce the peak width. On the other hand, this means that the ions loose much more energy in the magnet, so that

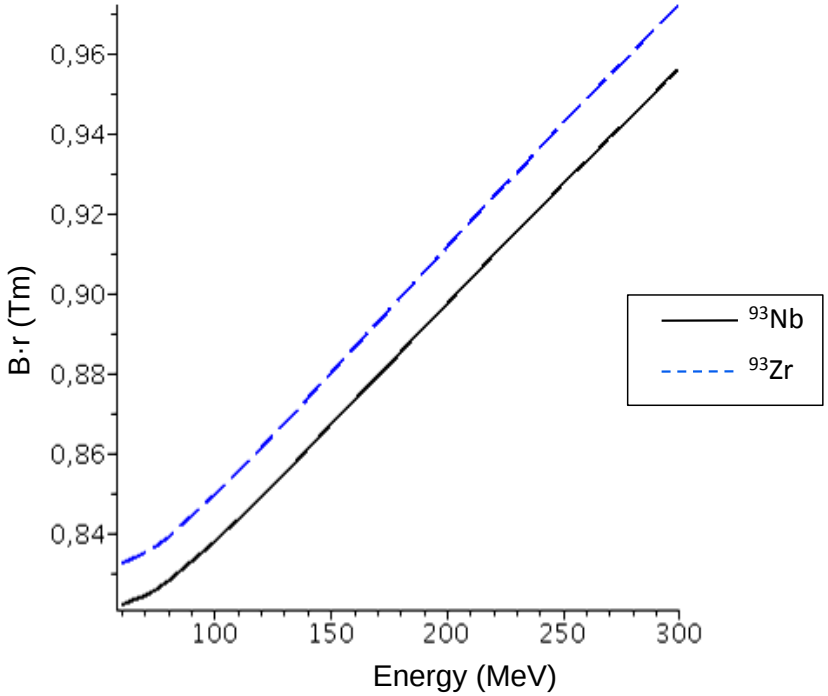

Figure 4.6.: Magnetic rigidity of ^{93}Zr and ^{93}Nb isotopes in a gas-filled magnet depending on their initial energy. The respective charge states were calculated by the Sayer parametrization.

the resolution of the subsequent Energy Loss Detector becomes worse. Therefore, it is reasonable to choose the highest initial energy of the ions which can be provided by the accelerator. For a more detailed discussion of the GFM characteristics see [46].

Energy Loss Detector

In order to identify the transmitted ions after the GFM, an energy loss detector is used, which is a ionization chamber with a segmented anode and a Frisch-grid. Fig. 4.7 shows a picture of the open detector, where the important features are marked. In this picture, the ions enter the detector, which is filled with isobutane, from the bottom. Similar to a normal ionization chamber, the ions collide with the atoms of the gas, so that those themselves get ionized. Thereby, the number of produced charge carriers is proportional to the energy of the ions, which are then collected by the anode (electrons) and by the cathode (ions). Since the drift of the ions is very slow, only the signal created by the electrons is analyzed. In the first place, all ions have the same energy which means that with regard to the energy there is no isobar separation. However, the energy loss of the ions in the gas, depends on the atomic number as described by the Bethe-Bloch-formula for completely ionized particles (see ch. 6.1.1). This means, that Nb ions are

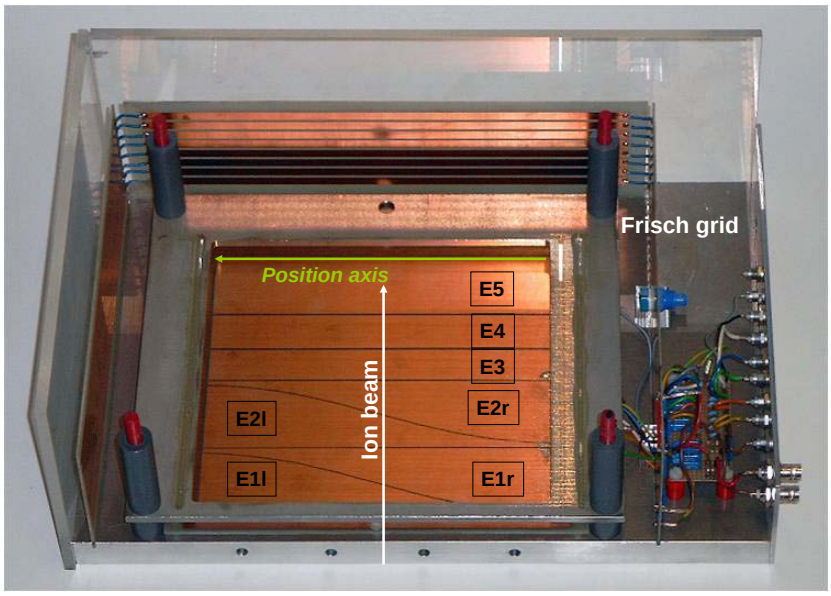

Figure 4.7.: Picture of the energy loss detector where the direction of the incoming beam, the 5 energy loss sections of the anode, the direction of the position axis and the Frisch grid are indicated. The diagonal separation of the first two sections which provides the horizontal position information, is clearly visible. Further explanations are given in the text.

decelerated more rapidly than Zr, which allows an additional differentiation of the two isobars. Therefore, the anode is divided into 5 segments perpendicular to the direction of the incoming beam. The gas pressure in the chamber is chosen, that the ions are completely stopped in the detector, i.e. in the 5th section. In this way, the complete energy of the ions is transfered to the detector gas which enhances the relative difference in energy loss of the isotopes which leads to a better separation. For the measurements of Zr the gas pressure was set to values between 45.7 and 48 mbar. Additionally, the first two sections are divided diagonally in order to obtain the horizontal position of the ions, which depends on the trajectory in the GFM. From the difference in time between the first and the third section, the vertical angle can be determined. Last but not least, the Frisch grid, which is positioned parallel to anode, measures the total energy deposited in the ionization chamber independently from the position. In total, we measure 9 parameter independently from each other. The respective signals are then amplified, digitized and read out by the Software MARaBOU [47]. Further information about the data acquisition can be found in [46]. The evaluation of the resulting data is described in ch. 4.3.

4.2.5. Time of Flight measurements in the Actinide beamline

In general, the Actinide beamline with its TOF path is used to detect very heavy isotopes, such as actinides [48] or to search for Super Heavy Elements [44]. Since there are no stable isobars for isotopes with masses larger than 209 amu, there is no need for an additional isobar separation. The ions have a fixed magnetic rigidity given by the Analyzing Magnet when entering the TOF path, which means that the following expression applies to all ions:

$$\frac{\sqrt{2mE}}{q} = \text{const.} \tag{4.8}$$

Inserting the non-relativistic formula for the kinetic energy leads to

$$\frac{m \cdot v}{q} = \frac{m \cdot L}{q \cdot TOF} \propto \frac{m}{q}. \tag{4.9}$$

where L is the length of the TOF path, E the energy of the ions and m the mass of the respective isotopes. With the TOF path fixed to L=2.9 m, the TOF is proportional to the ratio m/q which can be used to separate the ions. Ions with a comparable $\frac{m}{q}$-ratio as the radioisotope of interest can be distinguished by a ionization chamber at the end of the TOF path, similar to that of the GAMS but with only two ΔE and E_{rest}.

Fig. 4.8 shows a schematic drawing of the TOF set-up in the Actinide beamline. The

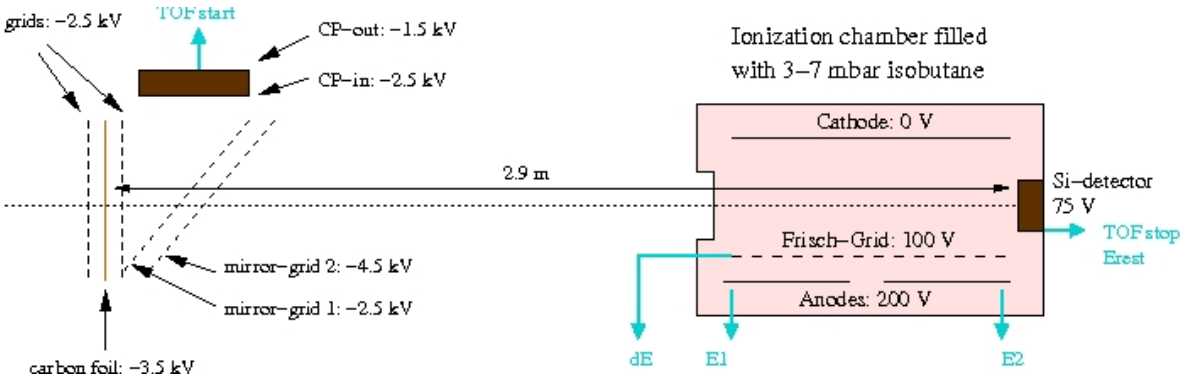

Figure 4.8.: Schematical drawing of the TOF setup, showing the micro channelplate detector on the left side and the ionization chamber with the semiconductor detector on the right side. The START signal for the TOF measurements is created if the ions pass the channelplate detector and the STOP signal is created by the ions being stopped in the Silicon detector (surface barrier detector). The ionization chamber with the segmented anode is needed to distinguish between isotopes with the same $\frac{m}{q}$-ratio. Source [44].

ions enter the TOF path by passing through a micro channelplate (MCP) detector

where the START signal is produced. The MCP consists of a 7 $\frac{\mu g}{cm^2}$ thick Carbon foil in which secondary electrons are produced by the passing ions. The electrons are then accelerated by a first grid and reflected by a 3rd grid which is at an angle of 45° to the carbon foil towards the CP where they are multiplied and finally produce the start signal. The applied voltages can be looked up in Fig. 4.8.

At the end of the TOF path, the ions have to pass the ionization chamber which is filled with 2-7 mbar Isobutane. This detector is very similar to the energy loss detector of the GAMS whose working principle is explained in ch. 3.2.4 (section "'Energy Loss Detector"'). By contrast, the anode is separated only in two sections. Again, the segmented anode detects the different energy loss of isotopes with a different atomic number whereas the Frisch grid provides a signal for the total energy loss in the chamber. The ions are stopped in a silicon surface barrier detector, where the rest energy of the ions is measured. The ions create electron-hole-pairs in the silicon, where the number of pairs depends on the energy of the ions. This signal, created by the electron-hole-pairs also serves as the STOP signal of the TOF measurement. A more fundamental description of the working principle of ionization chambers and semi-conductors detector is given e.g. in [49].

The carbon foil of the start detector causes energy straggling and hence, a broadening of the signals, which means that the resolution in the detector at the end of the TOF is worse. Furthermore, angular straggling leads to a lower transmission of ions from the MCP to the detector since the ions are scattered off the beam axis and thus do not reach the detector. However, the TOF measurements were solely performed with a passive absorber (several SiN foils) placed in front of the MCP in order to separate ^{93}Zr and its stable isobar ^{93}Nb (see ch. 7). With thicknesses between 2 and 4 $\frac{mg}{cm^2}$ the passive absorber causes energy and angular straggling to a much a higher extent, so that the contribution of the carbon foil is negligible. The resolution of the TOF measurements without passive absorber using two Constant Fraction Disciminators was 370 ps (FWHM) for ^{93}Nb.

4.3. Measurement Procedure

The previous section describes how to suppress the background and how to detect the ions of interest with the help of electrical and magnetic components of the setup. However, the spectra are rarely completely free of background which is demonstrated by a characteristic spectrum of ^{60}Fe in Fig. 4.9. The quantity, which we finally want to determine from the ^{60}Fe events in the spectrum, is

$$\frac{\text{number of ions of the radioisotope}}{\text{number of ions of the element}} = \frac{N(^{60}Fe)}{N(Fe)}. \tag{4.10}$$

Although, ^{60}Fe is an isotope frequently measured with the GAMS, it is not possible to clearly identify at first glance whether the individual events belong to the radioisotope or to the background. Thus, a careful data analysis and proceeding during the measurement are equally important. The following sections explain the characteristic procedure for an AMS measurement at the MLL, where ^{93}Zr represents any radioisotope which shall be detected by AMS in order to simplify the notation.

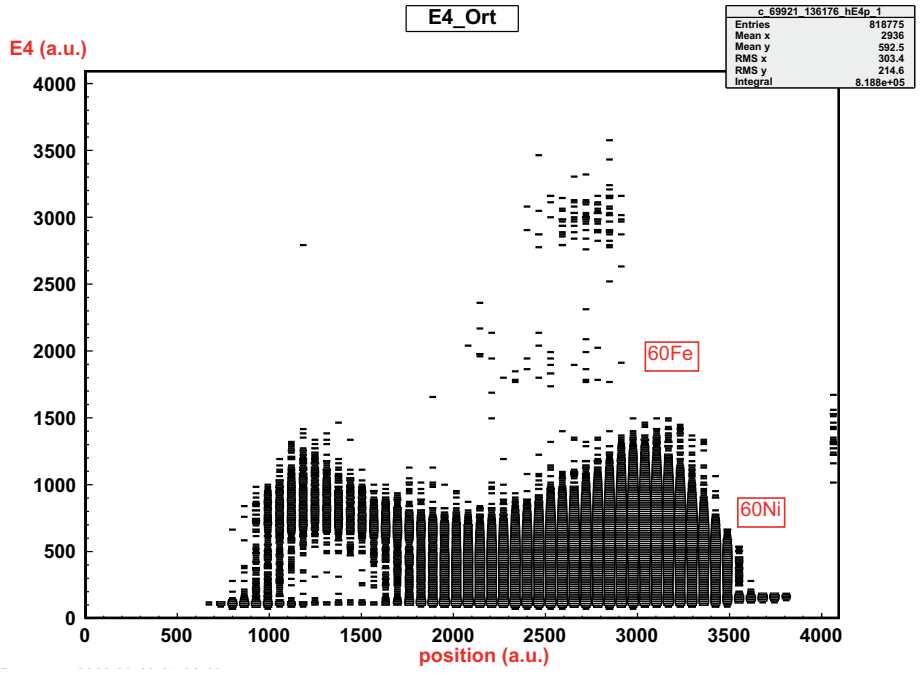

Figure 4.9.: Untreated spectrum of a sample with ^{60}Fe content, where the energy loss signal of the 4th anode depending on the position is plotted. It is not possible to identify at first sight which events belong to ^{60}Fe and which to the background. A large fraction of the background is made up of ^{60}Ni events.

First of all, we assume that we have clearly identified those events in the detector which correspond to the radioisotope, i.e. ^{93}Zr. In accordance with eq. (4.9), those events have to be related to the number of Zr ions. Additionally, the number of ^{93}Zr counts has to be normalized to the measured time and the currents provided by the source and transmitted by the beam guiding system. Both can be achieved by recording the macroscopic current of a stable isotope (e.g. ^{94}Zr) before and after the measurement of the radioisotope [2] (I_i and I_f) and to calculate the rate of Zr ions, i.e. the number of Zr ions per unit time t. By taking the average of both values, a possible change of the current during the measurement, is taken into account. This leads to the following

[2] This procedure also serves for monitoring if the current has changed significantly during the measurement

expression:

$$R(Zr) = \frac{N(Zr)}{t} = \frac{N(^{94}Zr)}{17.38\% \cdot t} = \frac{(I_i + I_f)/2}{17.38\% \cdot q \cdot e} \tag{4.11}$$

e=$1.602 \cdot 10^{-19}$As: elementary charge
q: selected charge state
17.38%: natural abundance of ^{94}Zr
R(Zr): rate of Zr ions

In order to obtain a rate of ^{93}Zr, the corresponding number of events in the detector simply has to be normalized to the measured time. The ratio of those two rates can be rewritten so that the desired concentration is obtained:

$$\frac{R(^{93}Zr)}{R(Zr)} = \frac{N(^{93}Zr)/t}{N(Zr)/t} = \frac{N(^{93}Zr)}{N(Zr)} \tag{4.12}$$

However, this consideration assumes, that all ions at the cup where the current is measured are indeed transmitted to the detector. In general, this is not the case. On the one hand, because of scattering, especially if a passive absorber is used and on the other hand, events which can not be clearly identified as ^{93}Zr have to be neglected. How is this taken into account?

Irrespective of whether the GAMS or the Actinide beamline is chosen, an AMS measurement therefore always requires a sample without radioisotopic content, a so-called blank, a sample with a defined concentration of the radioisotope, the so-called standard sample, and finally the sample whose radioisotope concentration shall be determined, itself.

The blank sample is used to adjust the different components of the setup, to optimize the beam guiding system and to analyze the background in the recorded spectra. By studying these spectra, one can conclude if there will be a strong interference with the events from the radioisotope. Although it is often possible to derive the position in the spectrum, where the ^{93}Zr events are expected from the location of the stable isotopes in the blank sample, this can be verified by measuring a standard sample. With this information, it is possible to develop a set of windows on the various signals (E1-E5, Er, TOF, etc), which is similar to a region of interest in other experiments, where the events of the radioisotope from the real sample are expected. Those windows have to be chosen such, that they are rather free from background (i.e. only few events in case of the blank sample) in order to be sure, that events from the real sample which are located in those windows have to be due to the radioisotope. This sometimes requires very narrow windows, which means that only a fraction of the Gaussian distributed events is considered as real ^{93}Zr counts. If the concentration was calculated from those events without correction, this would lead to a result which is too small.

This is taken into consideration by multiplying the number of Zr ions at the cup by the so-called transmission T, which is the percentage of particles that is really detected within the region of interest and is determined by the measurement of the standard sample. The transmission is defined in the following way (e.g. for ^{93}Zr):

$$T = \frac{\text{number of } ^{93}\text{Zr ions in the window}}{\text{number of } ^{93}\text{Zr at the cup before detector}} \tag{4.13}$$

Since the ratio of ^{93}Zr/Zr in the standard sample is known, the rate of ^{93}Zr events at the cup before the detector can be calculated from the ^{94}Zr current at the cup by rewriting eq. (4.10):

$$R(^{93}Zr) = \frac{c \cdot N(Zr)}{t} = \frac{c \cdot (I_i + I_f)/2}{17.38\% \cdot q \cdot e} \tag{4.14}$$

T is obtained by dividing the rate of ^{93}Zr events in the window by the rate of ^{93}Zr events at the cup given by eq. (4.13). It is now possible to calculate the number of Zr events corresponding to a given number of ^{93}Zr events in the windows if a real sample is investigated, leading to a correct normalization of the ^{93}Zr events to the ^{94}Zr events at the Cup.

However, measurements with ^{93}Zr and the passive absorber in the Actinide beamline required a slightly modified procedure, as currents had to be held quite low to avoid count rates much larger than 2 kHz in the ionization chamber. Thus, a current measurement was not always possible, so that events in the detector had to be normalized to the count rate of the channel plate at the TOF entrance. Further modifications of the procedure to determine the transmission are explained in ch. 7.3. where the measurements with the passive absorber are presented.

5. Sample Preparation

For a measurement with AMS, a standard sample with a defined ratio of ^{93}Zr/Zr, is required, apart from a blank sample without ^{93}Zr content[1]. Whereas the blank sample can simply be bought from almost all suppliers of chemicals, the standard material is not available. Therefore, it must be produced by irradiation of Zr with neutrons in order to obtain a measurable ^{93}Zr content by ^{92}Zr(n,γ)^{93}Zr reactions. The Radiochemistry Munich (RCM) kindly provided the blank sample and also carried out the irradiation of a piece of metallic, natural Zirconium in the Forschungsreaktor München II (FRM II). Due to the high initial activity of ^{95}Zr ($T_{1/2}$=64.0 d) the sample had to be stored for more than a year before it could be used further.

5.1. Irradiation of natural Zr

The high-purity Zr sample (99,8 %) was placed in the capsule irradiation facility for t=18 h, which is one of several irradiation systems of the FRM II [50]. The sample consisted of a small plate (m(Zr)=22,04 mg) of metallic Zr with a natural isotope ratio. In order to be able to calculate the ^{93}Zr/Zr afterwards, it is crucial to know the neutron flux during the irradiation at the respective position. Therefore, two more Zr foils were also irradiated close to the sample, serving as flux monitors to determine the thermal to epithermal flux ratio ($\Phi_{\text{thermal}}/\Phi_{\text{epithermal}}$) by the reations ^{94}Zr(n,γ)^{95}Zr and ^{96}Zr(n,γ)^{97}Zr. From the investigation of these additional Zr foils a thermal neutron flux of $(1.44 \pm 0.09) \cdot 10^{14}$ 1/cm^{2}s and an epithermal flux of $(3.14 \pm 0.19) \cdot 10^{11}$ 1/cm^{2}s could be deduced. With these information, and the initial number of ^{92}Zr atoms N(^{92}Zr) in the sample

$$N(^{92}Zr) = \frac{m(^{92}Zr)}{M(^{92}Zr)} = \frac{17.15\% \cdot 99.8\% \cdot m(Zr)}{M(^{92}Zr)} \tag{5.1}$$

where m(^{92}Zr) is the mass of ^{92}Zr in the sample and M(^{92}Zr) is the mass of a ^{92}Zr nucleus in g, one can now calculate the number of ^{93}Zr nuclei N(^{93}Zr) produced in the sample during the irradiation:

$$N(^{93}Zr) = N(^{92}Zr) \cdot t \cdot (\sigma_{\text{thermal}} \cdot \Phi_{\text{thermal}} + \sigma_{\text{epithermal}} \cdot \Phi_{\text{epithermal}}). \tag{5.2}$$

[1]The ^{93}Zr concentration in this sample has to be below the sensitivity of the setup.

The required neutron capture cross-sections $\sigma_{\text{thermal}} = (0.22 \pm 0.06)$ b and $\sigma_{\text{epithermal}} = (0.64 \pm 0.02)$ b, can be looked up in e.g. [51] or in the EXFOR database [14]. From this result, the final ^{93}Zr concentration relative to ^{92}Zr

$$\frac{N(^{93}Zr)}{N(^{92}Zr)} = (2.07 \pm 0.57) \cdot 10^{-6} \tag{5.3}$$

and in relation to the total number of Zr nuclei

$$\frac{N(^{93}Zr)}{N(Zr)} = (3.52 \pm 0.97) \cdot 10^{-7} \tag{5.4}$$

is obtained.

Whereas it was taken into account, that the number of ^{92}Zr atoms in the sample is reduced by the number of produced ^{93}Zr nuclei for the N(93Zr)/N(^{92}Zr) ratio, the number of Zr atoms in general was assumed to stay constant. In order to check if eq. (5.4) is a good approximation, the following consideration were made. Fig.5.1 shows the Zr region on the nuclide chart, in which the relevant processes during irradiation are marked. The figure demonstrates, that the absorption of neutrons does not only produce the desired ^{93}Zr, but also other unstable Zr isotopes, such as ^{95}Zr, with a much shorter lifetime than ^{93}Zr. These isotopes then decay via β^--decay into another nuclide (Nb, in this case) and therefore may reduce the overall Zr concentration of the sample.

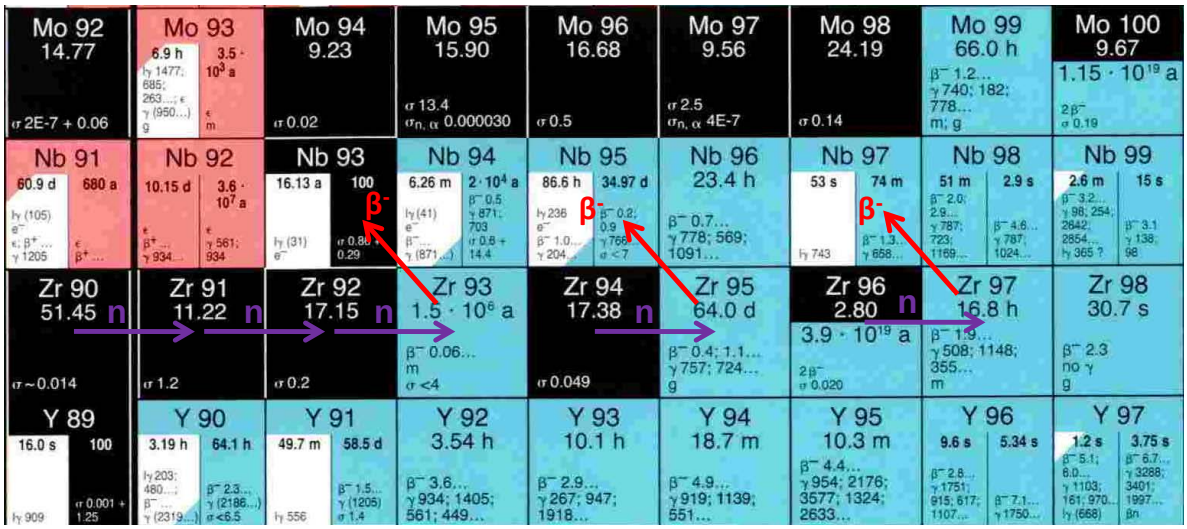

Figure 5.1.: Detail view of the nuclide chart, where the relevant nuclear processes, namely neutron absorption and β^- decay, are indicated by arrows. Modified from source [52].

However, the cross-sections for the reactions ^{94}Zr(n,γ)^{95}Zr and ^{96}Zr(n,γ)^{97}Zr are both

smaller by a factor of 10 than the cross-section for the neutron absorption of ^{92}Zr (compare Fig.5.1 or [14, 52]). Correspondingly, the ratio $\frac{N(95\mathrm{Zr})}{N(\mathrm{Zr})}$ is in the order of 10^{-8} since ^{94}Zr has a similar isotopic abundance as ^{92}Zr whereas the ratio $\frac{N(^{97}\mathrm{Zr})}{N(\mathrm{Zr})}$ will be even smaller ($\approx 10^{-9}$) due to the isotopic abundance of ^{96}Zr of only 2.80%. Thus, even if it is assumed that all ^{95}Zr and ^{96}Zr nuclei have decayed to the respective Nb isotopes in the meantime, the amount of Zr is not changed significantly and can therefore be neglected. Consequently, equation (5.4) is a good approximation.

5.2. Choice of Molecules

Besides the isobaric suppression by means of nuclear physics methods on the high energy side, also the use of the appropriate molecules in the ion source is essential. This is nicely demonstrated by the prominent example of ^{14}C whose stable isobar ^{14}N does not form negative ions, so that it is not extracted from the ion source. Due to the lack of isobaric background, measurements of ^{14}C can be done also at smaller Tandem accelerators with 1-3 MV terminal voltage. In general, elemental ions or low mass molecules (small number of light ligands) are preferred in order to obtain higher energies after the accelerator for a given terminal voltage (compare equation 4.4). However, the choice of molecules also strongly depends on the current that can be extracted from the ion source and its stability.

In the case of Zr, a suppression of Nb in the ion source is not known so far. By contrast, investigations done by other institutes show a similar behavior of Zr and Nb [53]. However, there are only little data available for the direct comparison of different Zr cathodes. Therefore, different molecules were tested with regard to the currents from the source and the ^{93}Nb interference. The following itemization gives an overview of the results of this investigation along with a discussion of further advantages and disadvantages.

Zr^- Negligible energy loss in the accelerator due to stripping, because no ligands. Injection of only the desired mass into the tandem, in agreement with [53] very small currents of 0.04 nA (^{94}Zr) at the Faraday-Cup in front of the accelerator (C1) (see Fig. 4.2).

ZrH_x^- Only small energy losses in the accelerator for all Hydrides. Currents in the order of 5 nA at C1 for all Hydrides. Consequently, neighboring isotopes are also injected into the accelerator as molecules with a lower or higher number of ligands which form a background in the detector which is difficult to discriminate from the events of interest. For example: If the injector magnet is set to $^{93}ZrH^-$ all molecules with mass equal to 94 amu pass the magnet. This means elementary

$^{94}Zr^-$ but especially $^{92}ZrH_2^-$ which can be extracted from the source with a similar current as a monohydride, are injected into the accelerator. In the detector, the events of mass 92, 93 and 94 are very close to each other (compare ch. 6).

ZrO_x^- The large mass of the ligand leads to an increased energy loss and a worse transmission through the Tandem accelerator due to Coulomb explosion [2], so that only ZrO^- comes into consideration. In comparison with other investigated Zr molecules, highest currents of 30 nA (^{94}Zr) at C1. ZrO is even at high temperatures chemically very stable. A disadvantage is, that the mass of ^{93}ZrO corresponds to the mass of ^{109}Ag which is present in the ion source due the silver powder mixed with the sample material. Thus, ^{109}Ag is directly injected into the accelerator, but can be very well distinguished from ^{93}Zr, respectively ^{93}Nb, in the detector (compare ch. 7.3).

ZrF_x^- The large mass of the ligand leads to an increased energy loss and a worse transmission through the Tandem accelerator, so that only ZrF^- comes into consideration. Currents of around 20 nA (^{94}Zr) at C1. However, it was observed in previous experiments with fluoride ions, that the performance of the ion source decreases rapidly. A possible explanation is based on the generally known high reactivity of fluoride ions. Those ions form a compound with the Tantalum atoms of the ionizer which has a lower work function for Cs^+ than the elementary Tantalum, thus reducing the efficiency of the ionizing process of the Cs atoms to Cs^+ ions. This in turn, worsens the efficiency of the sputtering process and finally reduces the currents coming from the source. However, with regard to the chemistry, Zirconium fluoride is the easiest compound to be produced from elementary Zr, as only dissolution in HF and a subsequent evaporating step is necessary (compare ch. 5.3).

Regarding these advantages and disadvantages, first measurements with the GAMS setup were performed using ZrH^- as it is essential in this case that ions enter the GAMS with the highest energy which is available from the accelerator (compare ch. 6). In a short beamtime of only three days, first measurements with a passive absorber were done with ZrF_4 powder as blank material. By contrast, for the longest beamtime lasting one week, the degradation of the ion source due to the fluoride ions was expected to be too severe, so that we switched to ZrO_2 powder as blank sample. Since the currents produced by elementary Zr are too small, it was decided to convert the elementary Zr of the standard sample into a compound. Within the scope of this Master's thesis this was only accomplishable for Zirconium fluoride.

[2] Positively charged remnants after the stripping repulse each other, since the valence electrons which were responsible for the chemical bonds are separated from the atoms [54].

5.3. Production of the ZrF_4 Standard sample

Compared to the concentrations of the standard sample of other isotopes already detected by AMS e.g. ^{60}Fe/Fe$\approx 10^{-11}$ the concentration of approximately 10^{-7} of the Zr standard sample, described in the previous section, is exceptionally high. This might cause a contamination of the ion source with ^{93}Zr, so that successive blank measurements will be misleading. Therefore, it was decided to reduce this concentration during the conversion of the metallic Zr into ZrF_4. In order to do this, the small, metallic Zr plate (compare ch. 5.1) has to be dissolved, which is only possible either with hydrofluoric acid (HF) or with aqua regia (compare ch. 4.1). In this case, the choice of HF suggests itself, since Fluoride ions are already present in the aqueous solution of HF and thus, ZrF_4 can be obtained by simply evaporating the solution.

The Inorganic Chemistry group of the Chemistry Department kindly provided their laboratory and their assistance for the handling of the HF. There, the Zr sample was first divided into two parts, of which only one of 10.2 mg was then dissolved with an excess of HF p.a.[3] (40%) in a small Platinum (Pt) crucible whereas the second half was kept for later use. The dissolution process of the Zr piece in HF took place almost instantaneously. Afterwards, the solution was heated from above by a quartz lamp to evaporate the liquid so that only ZrF_4 remains in the Pt crucible. Compared to the heating from below with a heating plate, this method has the advantage, that the solution does not start to boil, which reduces the probability that spillings escape from the crucible and cause a loss of material or serious injuries.

The ZrF_4 dried in this way was then divided again into two parts with a mass of 9.0 mg and 9.6 mg where different amounts of Zirconylchloride Octahydrate ($ZrOCl_2 \cdot 8H_20$) were added to obtain two samples which differ in the ^{93}Zr concentration. Since the Zr Hydrate has a natural isotopic ratio, one arrives at ^{93}Zr/Zr=$3.1 \cdot 10^{-8}$ by adding 0.18 g of $ZrOCl_2 \cdot 8H_20$ to the first and a ratio of ^{93}Zr/Zr=$6.7 \cdot 10^{-9}$ is obtained by adding 0.97 g of the Zr Hydrate to the second part of ZrF_4. Both samples were then dissolved in HF and subsequently evaporated several times, to make sure that the Fluoride ions entirely displace the OCl_2^{4-} ions in the compound with Zr. This is possible, since the Fluoride ions are smaller and have a higher electron affinity than the Chloride or Oxygen ions. Therefore the bonding with Fluoride is much stronger and thus preferred. Finally, one arrives at two standard samples: 0.11 g of ZrF_4 with a ^{93}Zr concentration in stable Zr of $3.1 \cdot 10^{-8}$ and 0.49 g of ZrF_4 with a ^{93}Zr concentration of $6.7 \cdot 10^{-9}$. Fig.5.2 summarizes the whole chemical processing of the Zr sample in a flow-chart.

[3] p.a. means pro analysi and denotes a higher degree of purity.

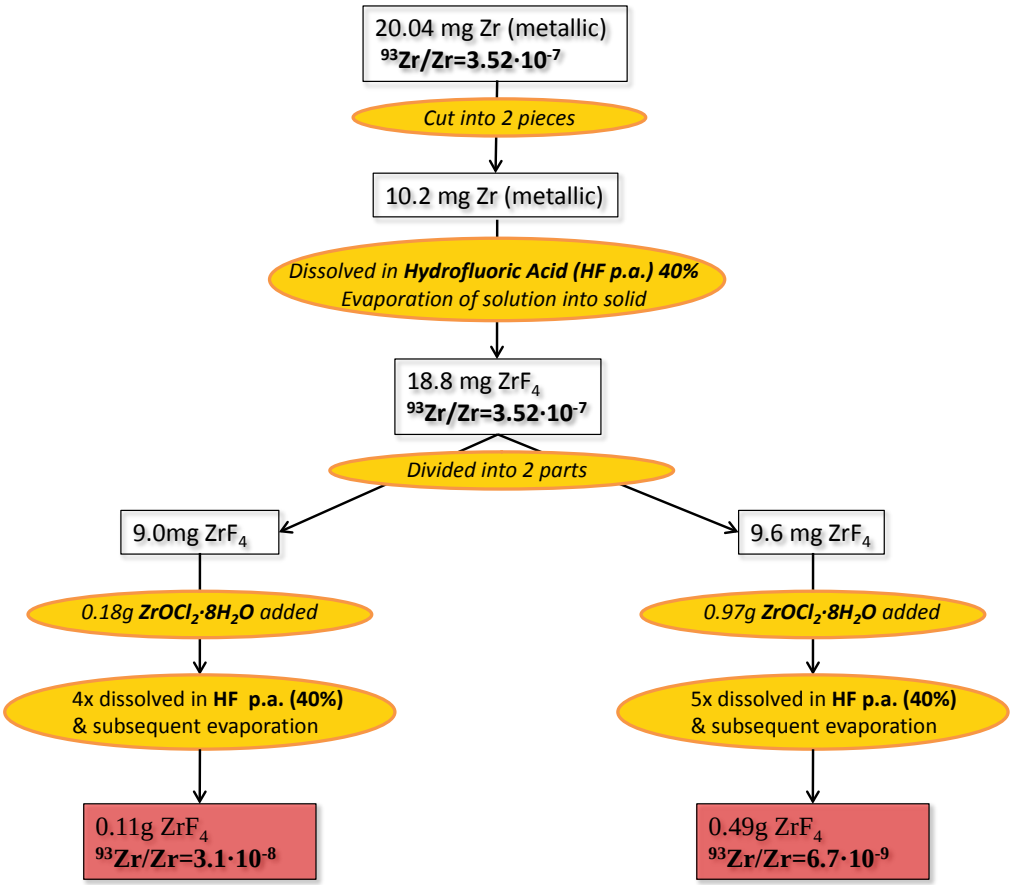

Figure 5.2.: Flow-chart of the chemistry done on the irradiated, metallic Zr sample in order to obtain 2 Standard samples of ZrF_4 with different ^{93}Zr concentration.

6. Separation of ^{93}Zr and ^{93}Nb by a Passive Absorber

The general idea is to insert a thin foil into the Actinide beamline before the TOF start detector acting as a passive absorber, in which the ions loose energy depending on their atomic number. Consequently, isobars will enter the TOF path with a different energy and therefore will cover the distance with a difference in time which can be used for isobar separation. Earlier experiments with ^{182}Hf and its isobar ^{182}W have shown promising results [55]. The question is, how thick does the foil have to be in order to achieve an optimal separation of the two signals with the current time resolution of our setup? Furthermore, one has to consider the fact, that multiple scattering in the foil causes energy and angular straggling which leads to the broadening of the peak width on the one hand, and on the other hand, it leads to a lower detection efficiency. Both effects complicate the separation of two peaks and are expected to increase with the thickness of the foil since more scattering processes take place. This means, a compromise between the difference in energy and straggling has to be found in order to obtain a optimal separation of ^{93}Zr and ^{93}Nb. Thus, simulations of the energy loss and the two kinds of straggling were performed, to find the optimal material and thickness of the foil.

Before the results of the simulations are presented, some theoretical approaches for the description of heavy ions passing through matter are discussed in the following section, in order to be able to interpret the results of the simulations and the experiment correctly.

6.1. Theoretical Background on Heavy Ions Passing Through Matter

At first it is important to clarify, what is meant by separation in this context. The relevant variables are indicated in Fig. 6.1, which shows two Gaussian distributions that represent the TOF signal of a radioisotope and its stable isobar. The difference in energy and therewith the difference in TOF is called distance D, the width of the peaks

is denoted as W and the Full Width at Half Maximum as FWHM. We define, that it is possible to clearly distinguish two peaks, if

$$D \geq 1 \cdot FWHM. \tag{6.1}$$

Thus, the width of the peaks has to be included in the considerations of the separation which is done by defining the separation S as

$$S = \frac{W}{D} \tag{6.2}$$

where W depends on FWHM by the usual expression

$$W = \frac{FWHM}{\sqrt{2ln2.}} \tag{6.3}$$

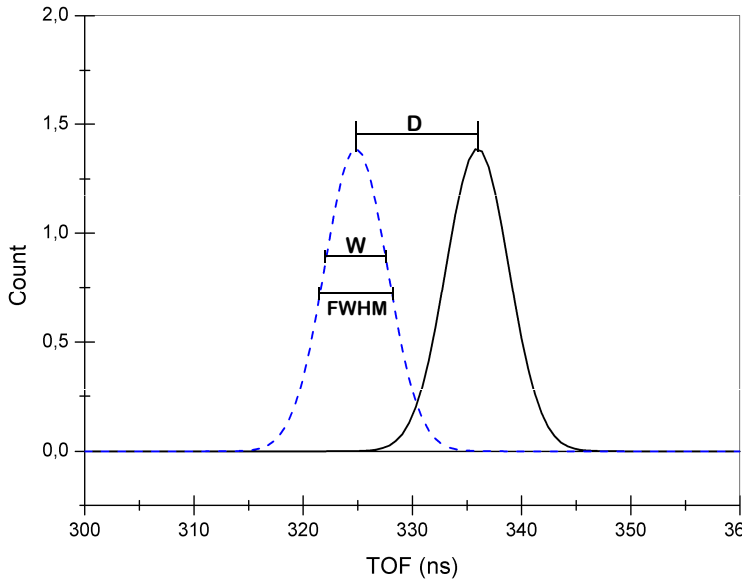

Figure 6.1.: Graphical representation of the quantities distance D, Full Width at Half Maximum FWHM and width W using the example of the Gaussian distributions corresponding to the ^{93}Zr and ^{93}Nb signals from the TOF measurement.

The passage of ions through matter and the resulting energy loss is a complex process, which is difficult to describe theoretically, since the ions get scattered repeatedly on the potentials in the solid. Naturally, this is a statistical process. Consequently, over the last century a variety of theoretical models with different regions of application depending on the initial assumptions were developed in order to derive a formula to describe the energy loss per unit path length. This quantity is called the stopping

power. The contribution of N. Bohr to this field has to be emphasized, who expressed some fundamental ideas of ion stopping around 1915 [56,57]. His work on the stopping of fission fragments lead to a comprehensive paper published in 1948 [58] covering the most important aspects of ions passing through matter. His concepts were then reviewed and amended amongst others by Bethe and Bloch, Lindhard, Scharff and Schiott [59, 60] and Northcliffe. (Semi-)empirical formulae such as the Sayer formula given in eq. (4.7) [45] could be derived by fitting the experimental data, which are very helpful for the use in experiments. Within the scope of this Masters Thesis, only the most relevant theoretical concepts can be presented in the next two sections. A detailed description of the theoretical models can be found in [61] and [62].

6.1.1. Energy Difference

If an ion passes trough matter, it is slowed down by scattering on the atoms of the target. In these collisions, energy is transfered from the ions to the target atoms, which is a complex many-particle problem. A simplification was stated by Bohr, who proposed to distinguish between the following two types of interaction [58]:

- electronic interaction: the energy of the ions is transferred to the electrons of the target, which can be assumed to be free or quasi-free.

- nuclear interaction: the energy of the ions is passed as recoil energy to the target nuclei, which can be described very well as an elastic scattering process of two screened charged particles.

The separate determination of the stopping power of both interactions and adding them up in order to obtain the total stopping power of the target is a reasonable approximation, since the response of the much heavier nuclei to the passage of a charged particle is much slower than that of the electrons. Therefore, the movement of the nuclei can be assumed to be not connected to the lattice of the solid.

Within the scope of the LSS-theory [59] (named after the authors Lindhard, Scharff and Schiott), it could be shown that in general, electronic stopping is much larger than nuclear stopping. Only for small energies, where the electronic stopping decreases linearly with the velocity, the nuclear contribution to the total stopping power becomes relevant. This is shown in Fig. 6.2 where the total stopping power of different ions in Aluminum (solid line) in addition to the electronic part (dashed line) is plotted over the initial energy per atomic mass unit (amu). A large discrepancy between the two curves can only be observed for heavy ions for energies smaller than 0.1 MeV/amu. Since in our case, the ^{93}Zr ions are accelerated to energies between 150 and 200 MeV, the major contribution comes from the electronic part, so that we will focus on the description of the electronic stopping power from now on.

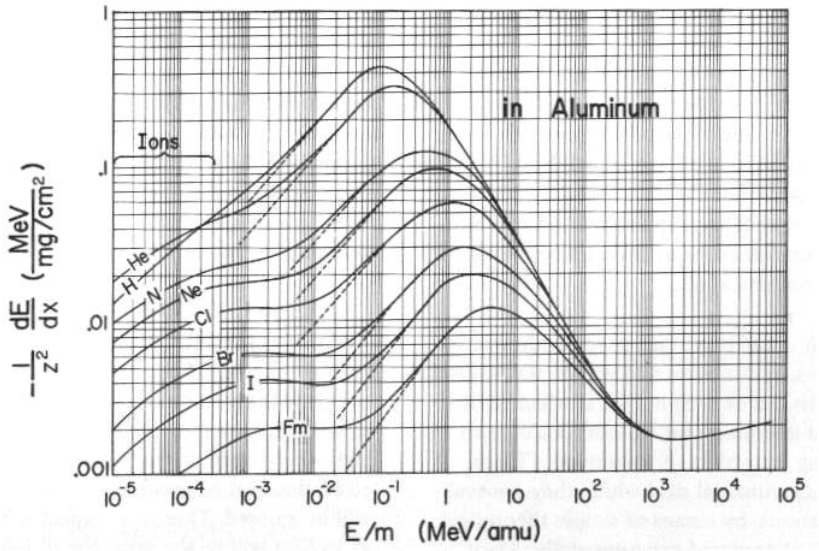

Figure 6.2.: Stopping Power of different ions in Aluminum depending on the energy. The solid line represents the total Stopping Power, the dashed line only the electronic part of it. Clearly, the nuclear stopping power is only relevant for very small energies. Source [63].

Electronic stopping combines a variety of different processes, which lead to the energy loss of the ion, e.g. excitation and ionization of the target atoms which is equivalent with an energy transfer to the strongly bound electrons, but also the excitation of band-or conduction-electrons is possible [62]. Apart from this, already Bohr pointed out, that additionally, ionization and electron capture of the ion itself may occur, which strongly influences its behaviour in the solid. Therefore, the average degree of ionization, the so-called effective charge, is an important concept in stopping theory. Depending on the effective charge, the heavy-ion stopping is divided into three energy regions, each described by a different theory [62]:

- Low-velocity regime (E $<$ 25 keV/amu): The stopping cross-section is described by the formulae derived by Lindhard and Scharff [59] or Firsov [62], which both show a direct proportionality to the velocity of the ion.

- Intermediate regime (25 keV/amu $<$ E $<$ 200 keV/amu), characterized by the effective charge which takes into account reduced shielding in close collisions. This model was developed by Ziegler [62] and is based on ideas of Brandt, Kitagawa [64] and others.

- High-velocity regime (E $>$ 200keV/amu): Scaling of the proton stopping power curve with an effective charge parameter, introduced by Bohr [43] and modified by Northcliffe [65].

- Bethe-Bloch regime (E > 10MeV/amu): The well-known Bethe-Bloch formula can be applied since the ions can be assumed to be completely ionized.

In our case, the Zr ions enter the passive absorber with energies a little higher than 2 MeV/amu and are slowed down to energies around 0.2 MeV/amu. Therefore, only a description of the high-velocity regime is required to estimate the energy loss of the Zr ions in the passive absorber. However, the Bethe-Bloch formula explains the fundamental dependencies of the energy loss on the target material, so that it will also be discussed in more detail in the next two sections apart from the high-velocity regime.

Bethe-Bloch regime

As early as 1913, Bohr was able to derive a formula describing the energy loss of charged particles in matter by simply considering the classical scattering problem where the ion and a target electron interact via the Coulomb force [56]. In order to estimate the energy transfered from the ion to the electron, Bohr adopted Rutherford's atom model for the description of the target atoms. He concluded, that the passing ions initiate a vibratory motion of the electrons with the vibration time of the electron being much larger than the collision time. Otherwise, the interaction would be adiabatic, which means that an energy transfer would not take place [58]. Therefore, he assumed the orbital frequency ν of the electrons to be distinctively smaller than the ratio V/λ where V is the velocity of the incoming ion and λ is defined in the following way [56]:

$$\lambda = \frac{qQ(M+m)}{V^2 mM}. \tag{6.4}$$

In this formula, capital letters represent quantities of the ions and small letters those of the electrons, with q denoting the charge and m the mass.

Finally, he obtained the following expression for the stopping cross-section per target electron with mass m_e for a projectile with atomic number Z_p and velocity v [66]:

$$S = \frac{4\pi Z_p^2 e^4}{m_e v^2} ln\left(\frac{C m_e v^3}{2\pi Z_p e^2 \nu}\right). \tag{6.5}$$

C is a constant which is equal to 1.1229 and e is the elementary charge.

This result is very similar to the expression for the stopping power which was obtained by Bethe, Bloch and others in the 1930s, who considered the electrons of the target atoms as quantum mechanical harmonic oscillators and solved this problem in the first Born approximation [67]. The respective expression for the stopping power reads as

follows:

$$-\frac{dE}{dx} = \frac{4\pi n_e Z_p^2 e^4}{m_e v^2}\left[ln\left(\frac{2m_e v^2\gamma^2}{I}\right) - \beta^2 - \frac{\delta}{2}\right] \tag{6.6}$$

with
$n_e = \frac{Z_T}{A_T}\rho_T N_A$: the electron density of the target
Z_T: atomic number of the target material
A_T: mass number of the target material
ρ_T: density of the target material
N_A: Avogadro's number
$\gamma = 1/\sqrt{1-\beta^2}$
$\beta = v/c$
I: mean excitation energy of the target
δ: correction term for the density effect[1]

For the calculation of the mean excitation energy, there are several empirical formulas available. The following expression, adopted from [68], differentiates between three regions with respect to the atomic number in order to take valence effects into consideration:

$$I \approx \begin{cases} 19.0eV & : \quad Z = 1 \\ 11.2eV + 11.7 \cdot ZeV & : \quad 2 \leq Z \leq 13 \\ 52.8eV + 8.71eV \cdot ZeV & : \quad Z > 13 \end{cases} \tag{6.7}$$

The ionization potential for a compound X_aY_b is calculated by using the formula

$$(a+b) \cdot ln(I_{XY}) = a \cdot ln(X_a) + b \cdot ln(Y_b) \tag{6.8}$$

which leads to the following values for the ionization potential of Silicon Nitride (SiN) and Beryllium (Be):

$$I(SiN) = 141.6\,eV$$
$$I(Be) = 58\,eV$$

For non-relativistic heavy ions, which is the case for our measurements, the Bethe-Bloch formula can be simplified, since β^2 is much smaller than one, and therefore can be neglected and γ becomes equal to one. In addition, the correction term can be left out, since the density effect is only relevant at relativistic velocities. Writing the simplified formula in terms of the initial energy E_p of the projectile, one obtains:

$$-\frac{dE}{dx} = \frac{2\pi {Z_p}^2 m_p e^4}{E_p m_e}\frac{Z_T}{A_T}\rho_T N_A ln\left(\frac{2m_e E_p}{I m_p}\right) \tag{6.9}$$

[1] An explanation of the density effect can be found in [67].

The stopping power of ^{93}Zr and ^{93}Nb in Be and SiN was calculated using eq. (6.9). Its dependence on the energy is shown in Fig.6.3. More precisely, $\frac{1}{\rho}\frac{dE}{dx}$, the mass stopping power, is plotted in this diagram. The following stopping power graphs always show the mass stopping power which is referred to by dE/dx. The picture shows the

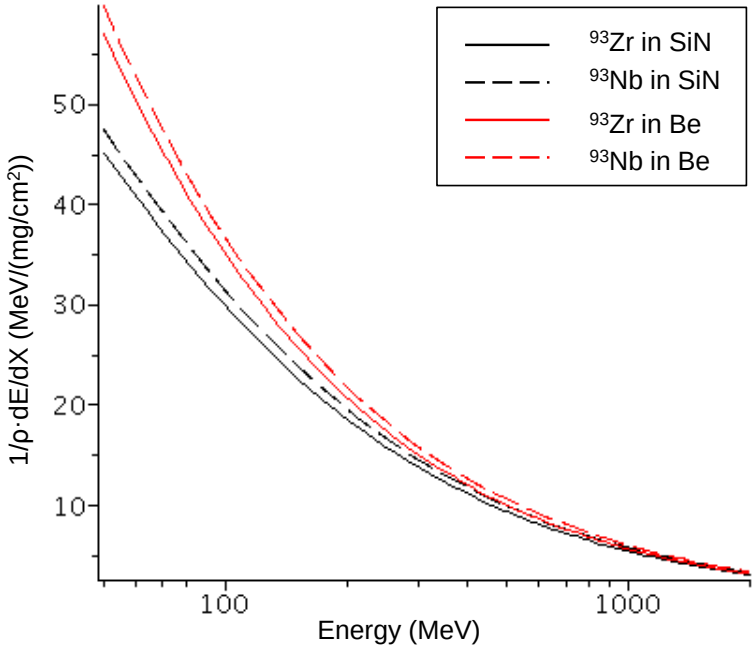

Figure 6.3.: Mass Stopping Power calculated with the non-relativistic Bethe-Bloch formula in eq. (6.9) for the two isotopes ^{93}Zr and ^{93}Nb in two different materials, SiN and Be. Due to the smaller ionization potential of Be, the stopping power is larger than that of SiN.

two main dependencies of the stopping power: Due to the higher Z/A ratio of SiN which corresponds to a higher electron density than in Be, there is a higher probability for scattering. Thus, one would expect in the first place that the ions loose their energy more rapidly in SiN than in Be. However, the considerable smaller ionization potential of Be, compensates the higher electron density of SiN, though there is only a logarithmic dependence on the ionization potential. Consequently, the electrons of Be are ionized more easily, which is the dominating energy loss process for slow heavy ions. Furthermore, the stopping power of Nb ions is larger than that of Zr ions owing to their higher atomic number. However, especially for energies below 100 MeV the stopping power curves in Fig. 6.3 differ considerably from those which were obtained experimentally [63]. The experimental curves show a flattening or even a maximum at these energies below the lower limit of validity of the Bethe-Bloch formula.

Since the energy loss increases with decreasing energy of the ions, the energy deposited in the solid reaches its maximum shortly before the ions are completely stopped i.e.

at the end of the particle tracks. In order to characterize this behaviour the stopping power is plotted depending on the penetration depth, which is called the Bragg curve. The corresponding maximum at the end of the track which rapidly drops down to 0 for higher depths, is called the Bragg peak.

The lower limit for the application of the Bethe-Bloch formula is caused by the assumption of completely ionized particles, which is not valid if the velocity of the ions has dropped to the order of the electron velocity. At these velocities charge changing effects become important which screen the nuclear charge and therefore decrease the stopping power.

High-velocity Regime

A more correct description is that the ion which passes the solid continuously absorbs and looses electrons in a large number of collisions with the target atoms and thus an equilibrium charge distribution with an average net charge arises. In the simplified picture of Bohr, which was already mentioned in ch. 4.2.4, an electron is permanently captured if its orbital velocity is larger than the velocity of the ion. By contrast, Lamb assumed the kinetic energy of the electron and the ion to be the key parameter which determines the permanent capture of an electron. However, by an extensive study of stopping power curves of different heavy ions which he related to the well-known stopping power of protons, Northcliffe was able to show that the approach of Bohr was more promising.

Since the absorbed electrons screen the nuclear charge, the idea was to derive an expression for the remaining fraction of the charge, the so-called effective charge, which is responsible for the energy loss of heavy ions. In this way, already known concepts (e.g. the Bethe-Bloch formula) should have been able to be applied by just replacing the atomic number by the effective charge of the ion. A very common method to determine the stopping power of a heavy ion (S_{HI}) with a velocity v_{HI} and an atomic number Z_{HI} is to start from the stopping power of a proton (S_P) and to scale it according to the effective charge Z^*_{HI} [62, 63]:

$$S_{HI} = (Z^*_{HI})^2 \cdot S_P. \tag{6.10}$$

where Z^*_{HI} can be expressed in terms of the atomic number by introducing an effective charge parameter γ^2

$$Z^*_{HI} = \gamma \cdot Z_{HI}. \tag{6.11}$$

The effective charge parameter γ^2 can be derived from Bohrs condition for the capture of an electron by using Thomas-Fermi atomic theory to describe the heavy ions which

leads to the expression given in eq. (4.7) for the effective charge and thus for γ

$$\gamma = \frac{v_{HI}}{v_0 \cdot Z_{HI}^{2/3}} \tag{6.12}$$

where $v_0 = \alpha \cdot c$ is the Bohr velocity, α the fine-structure constant and c the speed of light. The expression for γ which Northcliffe has obtained by fitting the experimental data [63, 65]

$$(\gamma)^2 = 1 - exp\left(\frac{-v_{HI}}{v_0 \cdot Z_{HI}^{2/3}}\right) \tag{6.13}$$

can be expanded which leads to the result of Bohr in eq. (6.12).

Fig. 6.4 demonstrates how very well the experimentally obtained data is described by the scaling technique based on Thomas-Fermi atoms. The experimentally reduced stopping which is plotted on the y-axis, which is equal to the square of the effective charge parameter γ^2, which is obtained by solving eq. (6.10) for γ when S_{HI} and S_P are determined experimentally. Correspondingly, the calculated reduced stopping plotted on the x-axis is equivalent to γ^2 calculated in eq. (6.12). The data points can be fitted very well by a straight line which is described by the equation $y = x$ indicating an excellent agreement between experiment and theory. However, below a certain velocity i.e. when the ion is almost neutral, it is not longer correctly described as a Thomas-Fermi atom, so that Bohr's formula for the effective charge is not valid for ions with $v_{HI} < 3 \cdot v_0$.

Just as the Bethe-Bloch formula, also the scaling method shows a dependence of the stopping power on the atomic number. Thus, Nb is supposed to leave a passive absorber of a given thickness d with a lower energy E_f than Zr which means that Nb ions have a lower velocity and hence, a higher TOF than Zr which enables the separation of the two isobars. Owing to the fact, that the stopping power itself is a function depending on the energy F(E), one has to solve the Differential Equation

$$F(E) = \frac{dE}{dx} \tag{6.14}$$

by separation of variables

$$\int_{E_0}^{E_f} \frac{1}{F(E)} dE = \int_0^d 1 \cdot dx \tag{6.15}$$

which can be simplified to

$$\int_{E_0}^{E_f} \frac{1}{F(E)} dE = d \tag{6.16}$$

in order to calculate the final energy of the ions after a target of thickness d. The last equation, in which E_0 is the initial energy of ions, can be rewritten to obtain an explicit expression for E_f as F(E) can be obtained by fitting the values of the Stopping Power given in tables [63] or in simulation programs (e.g. SRIM [62]). The corresponding results for Nb and Zr will be discussed in ch. 6.2.

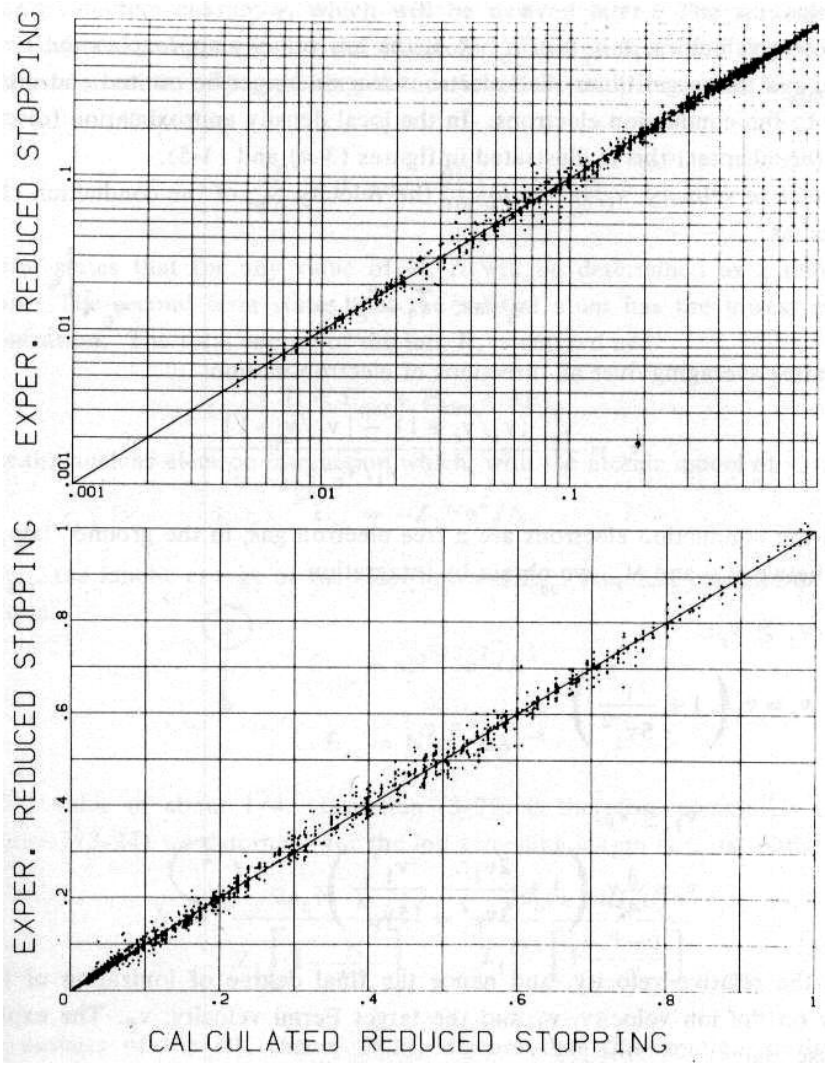

Figure 6.4.: Comparison of experimental values for γ plotted on the y-axis and theoretical values for γ plotted on the x-axis which were obtained by applying the Bohr's criterion for a Thomas-Fermi atom. For the line which fits the data very well, the equation y=x holds. Thus, there is a good agreement between theory and experiment. Source [62].

6.1.2. Energy and Angular straggling

Due to the statistic nature of the energy loss, the energies after the solid are described by a Gauss distribution. This broadening of a single initial energy to an energy distribution is called energy straggling. Furthermore, the multiple scattering processes are responsible that particles leave the solid under an angle to the beam axis, which is known as angular straggling. Particularly energy straggling worsens the resolution in the detector since the width of the signals is increased. Therefore, the separation

S of two peaks shown in Fig. 6.1 decreases and thus has also to be considered in our experiment.

One of the earliest approaches of describing energy straggling was also made by Bohr [58], who derived a formula for the variation of the energy loss just by mechanical considerations with the Coulomb force being the interacting force. Thus, he arrived at the expression for Ω which corresponds to the width (FWHM) of the resulting energy distribution

$$\Omega_B^2 = 4\pi Z_P^2 Z_T e^4 N d \tag{6.17}$$

Z_P: atomic number of projectile
Z_T: atomic number of target
d: thickness of target
N: atomic density
e: elementary charge

where the subscript 'B' denotes the straggling which is called 'Bohr straggling' from now on. The Bohr straggling shows a linear dependence on the thickness and the atomic number of the target material, which means that a thin foil with low atomic number would be favorable. However, Bohr straggling systematically overestimates the straggling for slow heavy ions, since Bohr assumed fast and fully stripped ions which is not the case according to Bohr's principle (see previous chapter). Furthermore, he approximated the electron density in the solid by using the free electron gas model. There were strong efforts in the following years to develop models for energy straggling which are based on more realistic electron distributions in the solid. For example, Chu derived a formula for the energy straggling of protons and He ions using Hartree-Fock-Slater charge distributions [69]. The disadvantage of such models is, that they are often much too complicated for the practical use.

For this purpose, empirical formulae which were obtained by fitting the experimental data are much more suitable. To estimate the energy straggling in our measurements, the Yang-formula [70] has been used which provides a correction factor to the Bohr straggling. Yang-straggling is based on the fitting of Chu's calculations where the fit has the form

$$\left(\frac{\Omega_{Chu}^2}{\Omega_B^2}\right) = \left(1 + A_1 E^{A_2} + A_3 E^{A_4}\right)^{-1} \tag{6.18}$$

where A_1-A_4 are Z_T dependent fitting factors. Similar to the stopping power, also the energy straggling of heavy ions has to be scaled according to the fractional effective charge parameter γ:

$$\left(\frac{\Omega^2}{\Omega_B^2}\right)_{HI} = \gamma^2 \cdot \left(\frac{\Omega_{Chu}^2}{\Omega_B^2}\right) + \left(\frac{\Delta\Omega^2}{\Omega_B^2}\right)_{HI} \tag{6.19}$$

The additional term takes into account correlation effects and is given by a rather complex empirical formula which can be looked up in [70]. Fig. 6.5 demonstrates graphically the dependence of the Yang straggling normalized to the Bohr straggling on the energy for the target materials Be, C, SiN, which were available for the experiments. The curves were calculated using ^{93}Zr as projectile. As expected, the Yang-straggling gets close to the Bohr straggling for high energies. However, for the energies, which were expected to occur in the experiment (starting with an initial energy of 200 MeV and slowing down to a final energy of around 20 MeV) approximating the straggling just with the Bohr straggling would not be correct, since there are large deviations expected from this graphs. Especially Be shows a very large ratio, which possibly originates from shell effects. Those have an increased importance for light atoms. Since the Bohr straggling

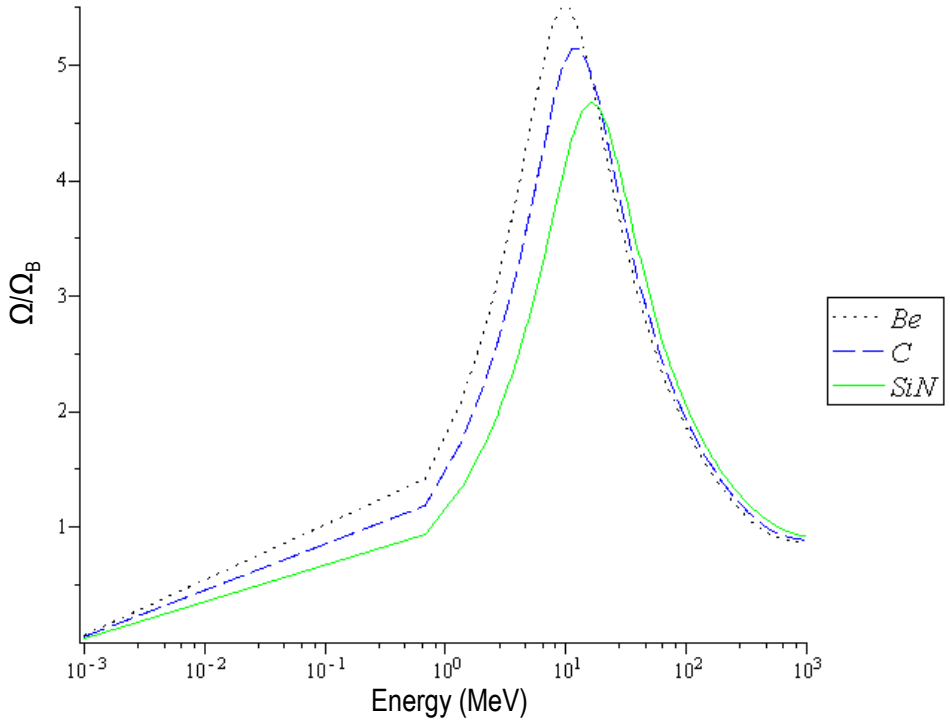

Figure 6.5.: Deviation of the empirical Yang straggling formula from the Bohr straggling for ^{93}Zr ions in the target materials beryllium (Be), carbon (C) and silicon nitride (SiN) depending on the energy of the ions. This ratio was calculated with eq. (6.19). Whereas the energy straggling can be approximated very well by the Bohr straggling for energies above 1000 MeV, it is considerably underestimated in the energy range between 200 MeV and 20 MeV which is relevant for our experiment.

does not depend on the energy (see eq. 6.17) and thus, is only a constant factor which has to be multiplied with the straggling functions shown in Fig. 6.5, the final result for

the Yang straggling which is presented in Fig. 6.6 has approximately the same shape. In the calculation using eq. 6.17, an identical surface density of 1 mg/cm^2 for all three materials was assumed. Owing to the fact, that SiN has the highest atomic number of

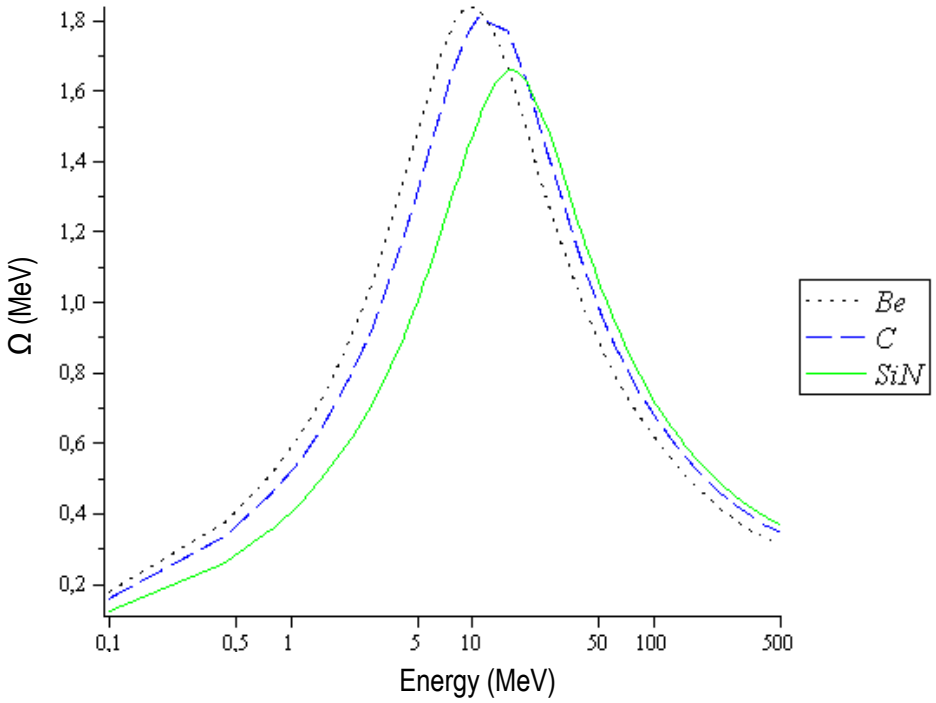

Figure 6.6.: Empirical Yang straggling for ^{93}Zr ions in the target materials beryllium (Be), carbon (C) and silicon nitride (SiN) depending on the energy of the ions. The curves were calculated by multiplying the correction factor shown in Fig. 6.5 with the corresponding, energy independent Bohr straggling (eq.6.17).

the three materials, it shows the largest energy straggling for high energies and also in the largest part of the energy range relevant for our experiment. Though, it has to be taken into account, that the Zr ions pass through each energy in the relevant energy range when they are decelerated in the solid. Therefore, it is necessary to integrate the Yang formula to compare the different materials.

Furthermore, the homogeneity with respect to the thickness of the material has to be considered. According to Besenbacher et al [71], the corresponding additional term to the straggling scales with the square of the stopping power, if it is assumed that the foil thickness distribution is Gaussian:

$$\Omega_d^2 = (dE/dx)^2(\Delta d)^2 \tag{6.20}$$

Hence, this additional term is suggested to be much larger for Be than for SiN, due to the larger stopping power which we have calculated using the Bethe-Bloch formula in eq. (6.9) and which is presented in Fig. 6.3. Furthermore, according to this expression the variations of the thickness should be kept as small as possible. It is known, that SiN foils can be produced with an outstanding uniformity which cannot be reached with C or Be foils. Since it was experienced in previous experiments that C foils are inapplicable because of this reason, only Be and SiN foils were considered in the simulations. However, this additional straggling term cannot be simulated and we are not able to calculate it, since the variations of the thickness are not known precisely. Thus, this higher term for Be might outweigh the lower Yang straggling of Be so that the total energy straggling of SiN might be lower. Consequently, we had to find out experimentally and have to keep eq. (6.20) in mind when discussing the results.

Since angular straggling does not decrease the separation in the first place, it was not a determining factor for the choice of the target material. Therefore, the theory of angular scattering was not studied in detail, but the extent which has to be expected in the experiment was estimated by simulations with SRIM03 [62] which is described in the next section.

6.2. Simulations

6.2.1. Stopping Power in SiN

The idea of doing simulations was to determine the optimal thickness of the passive absorber where the separation S has its maximum, in order to minimize the time which has to be invested in rearranging the setup during beamtime. However, the stopping power curves for ^{93}Nb and ^{93}Zr in SiN and Be which were obtained by SRIM03 and CORTEO [72], showed some interesting deviations from the stopping power curves which were calculated by using the tables provided by Northcliffe and Schilling [63]. Both results are plotted in Fig. 6.7 for comparison. Whereas the result from Northcliffe (left picture) shows the behavior which was expected from eq. (7.10), i.e. a consistently higher stopping power for Nb than for Zr owing to the $Z^{2/3}$ dependence, there is an intersection point in the SRIM03 stopping power plot (right picture) at around 165 MeV and a second one at approximately 23 MeV, indicated by two vertical lines. This difference has an essential influence on the choice of the thickness of the absorber or the initial energy of the ions.

If the Northcliffe curve describes the stopping correctly, an energy loss as large as possible would lead to the largest difference in TOF. This in turn means that the highest energy of the ions which is available should be chosen and the passive absorber

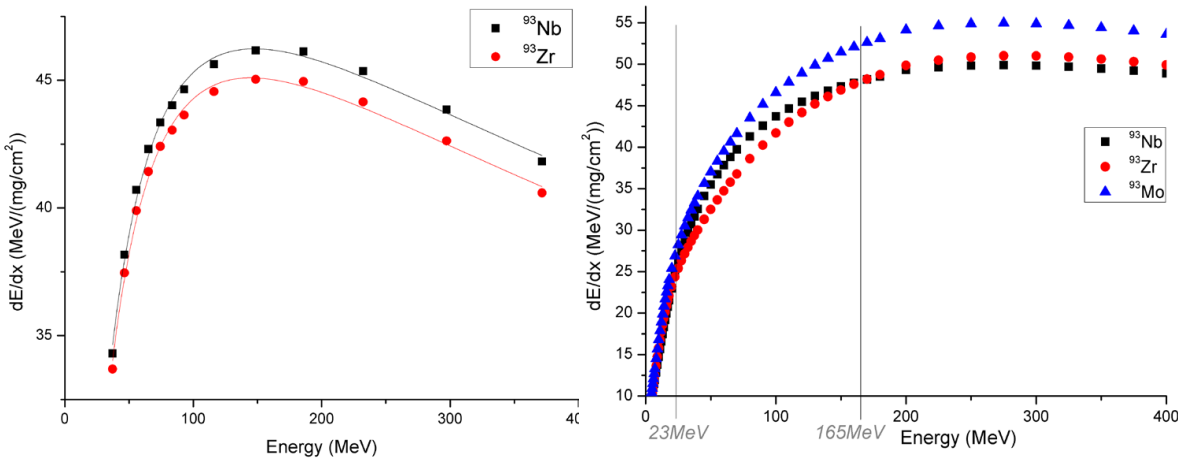

Figure 6.7.: Left: Stopping power for Nb and Zr in SiN depending on the energy calculated from the tables of Northcliffe & Schilling [63]. Right: Stopping power for Nb and Zr in SiN depending on the energy obtained from SRIM03 [62].

should be chosen as thick as possible as long as the straggling is not considered and the ions have enough energy left to be detected at the end of the TOF path. In contrast, in the case of the SRIM stopping power plot, using the maximal available energy of around 190 MeV would not cause any benefit compared to the case when the energy of the intersection point is chosen. The small difference in TOF at energies above the intersection point which is not sufficient for the separation of Nb and Zr, is reversed during slowing down in the passive absorber.

This is demonstrated in Fig. 6.8(a-d), which shows the results of the TRIM03 simulations of the energy loss of ^{93}Nb and ^{93}Zr ions with an initial energy of 210 MeV in a SiN passive absorber at different thicknesses. For this purpose, the energy distributions, which were obtained from the simulations, were converted into a Gaussian TOF distribution by using eq. (4.8). The width of the TOF distributions were calculated by quadratic error propagation from the width of the energy distribution and the amplitude was chosen arbitrarily equal to 10 (a.u.). In a real spectrum from a measurement we do not expect the ^{93}Nb and ^{93}Zr peak to have the same amplitude, since we suppose a considerably larger concentration of ^{93}Nb in the samples.

In the case of Fig. 6.8(a), the SiN is rather thin (1.0 mg/cm^2), so that the larger part of the energy loss happens in the energy range above the intersection, where the stopping power of Zr is larger than that of Nb, leading to a higher TOF of Zr than of Nb. This is reversed in the pictures Fig. 6.8(c-d), where the ions are decelerated to energies well below the intersection point. At a certain thickness, the part of the stopping with Nb having the higher stopping power starts to dominate the total energy loss. Consequently, the TOF of Nb is larger than that of Zr (Fig. 6.8(b)). With further increasing thickness of the passive absorber, the distance between the center of the Nb

peak and Zr peak also becomes larger, since the stopping power of Zr constantly stays below that of Nb in that energy range (Fig. 6.8(c+d)). Furthermore, the peaks broaden owing to the increasing energy straggling. The calculations made in (Fig. 6.8(b-d)) are consistent with the theoretical models, explained in chapter 6.1.

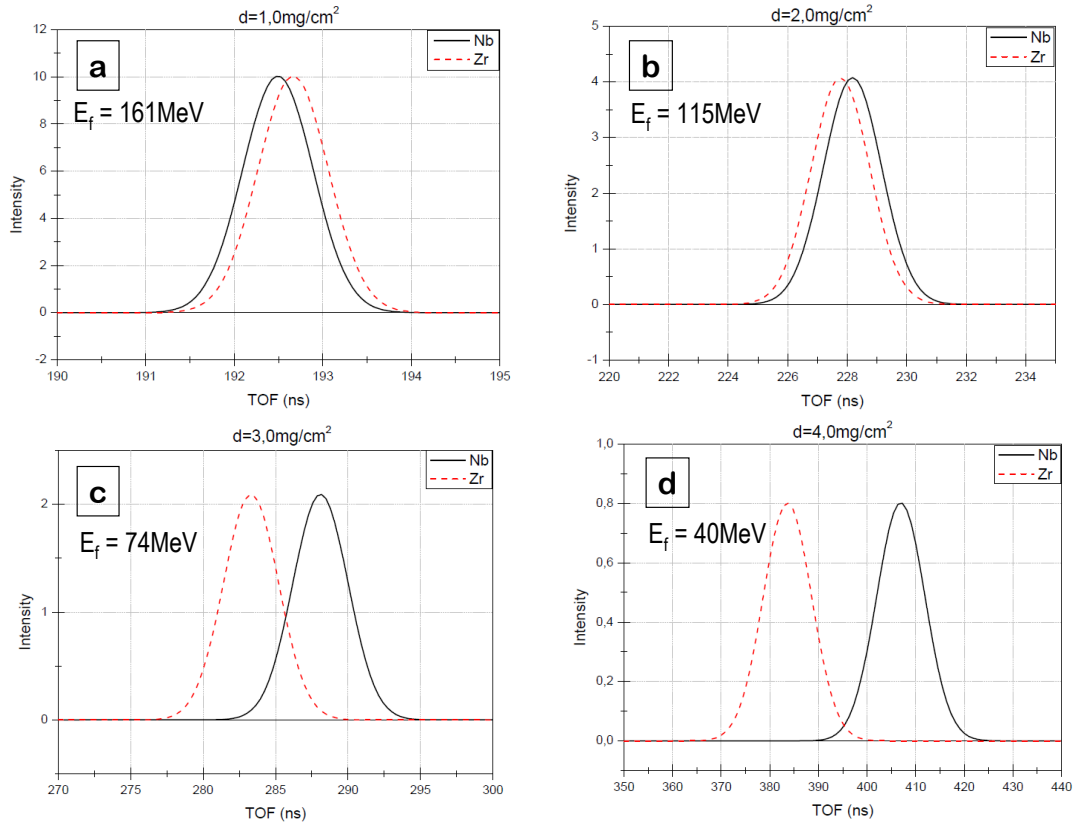

Figure 6.8.: Result of the simulations with TRIM03 for different thicknesses of SiN (a-d). The final energy E_f which corresponds to the TOF of the ^{93}Zr Gaussian is given in the pictures.

The results of the simulations presented in Fig. 6.8(a-d), in turn mean, that for a given energy the optimum of the separation S is shifted to higher thicknesses compared to the Northcliffe scenario. Hence, the maximum of S was found to be at d=4.5 mg/cm^2 by performing SRIM simulations and at d=3.5 mg/cm^2 for the Northcliffe stopping power curve. In the second case, S was obtained by fitting the stopping power which is shown in Fig. 6.7 as solid lines and integrating the corresponding functions using eq. (6.16) which was rewritten into an expression for the final energy. For the calculation of the energy straggling the Yang-formula (eq.(6.19)) was used.

The interesting question is: Which of the two scenarios does describe the energy loss correctly? The Northcliffe tables seem to be more reasonable since they are in good agreement with the theory of scaling. This point of view was also supported by J.Ziegler who explained the deviations of the SRIM stopping power in the following way: Origi-

nally the Nb stopping power obtained from theoretical modeling was between the curves of Zr and Mo, but was then modified by all the experiments, whereas there was not enough data to revise the Zr and Mo stopping [73]. It is assumed, that the program CORTEO uses the same stopping power tables as SRIM and thus arrives at the same results. Therefore, it can be expected that the stopping power of Zr and Mo should also be below the theoretical values but this has to be verified experimentally. In general, the response of J.Ziegler suggests that the Northcliffe scenario has to be applied and thus, the optimal thickness is d=3.5 mg/cm^2.

6.2.2. Stopping Power in Beryllium

Apart from the simulations for the energy loss in SiN, simulations with SRIM03 and CORTEO were also performed for Be as target material. The energy dependence of the stopping power of Zr and Nb in Be as well as in SiN are shown in Fig. 6.9 for comparison. The presence of the intersections points which were discussed in the previous section are clearly independent of the target material, as they are also present in the Be plot. The absolute value of the stopping power in Be is much larger in the energy range between 400 and 20 MeV than that of SiN, though Be has a smaller atomic number. However, this is in very good agreement with the predictions of the Bethe-Bloch formula (see ch. 6.1.1 and Fig. 6.3).

The stopping power of Be has a much steeper slope for energies below the maximum than SiN. This makes Be especially interesting as passive absorber, since the relative difference in the stopping power of Nb and Zr for a given energy will be larger in Be than in SiN, which is indicated in Fig. 6.9 for an arbitrarily chosen energy of the ions. The relative difference in the stopping power which can be read off this graph is 0.092 for Be and 0.089 for SiN. Hence, a larger difference in the TOF of the isobars can be expected if Be is used as passive absorber. In good agreement with straggling theory (compare ch.7.1.2, Fig.6.6), the SRIM and also the CORTEO simulations showed a lower energy straggling for Be than for SiN as long as the final energy of the Zr ions is above 20 MeV. If the final energy drops below this value, the straggling increases much faster than in the case of SiN. Consequently, the two peaks in Fig. 6.10(b) where the SRIM03 results for ^{93}Zr and ^{93}Nb with an initial energy of 210 MeV passing through Be with d=2.77 mg/cm^2 are better separated than in Fig. 6.8(c) with a slightly higher thickness of d=3.0 mg/cm^2. The thicknesses of the Be in the simulations were chosen according to the Be foils which were available for the experiment. These are foils with d=5μm ($\widehat{=}$0.92 mg/cm^2) and d=10μm ($\widehat{=}$1.85 mg/cm^2) which can be combined in a stack to obtain thicker absorbers. Fig. 6.10(a) shows the result from the SRIM03 simulation for Be with a thickness of 10μm which is obviously not sufficient for a clear separation of the two isobars. The maximal separation which can be achieved in the case of Be is considerably larger than that of SiN (see Fig. 6.11) and at a lower thickness, due to the larger stopping power and its sharp decline at lower energies. At higher thicknesses the

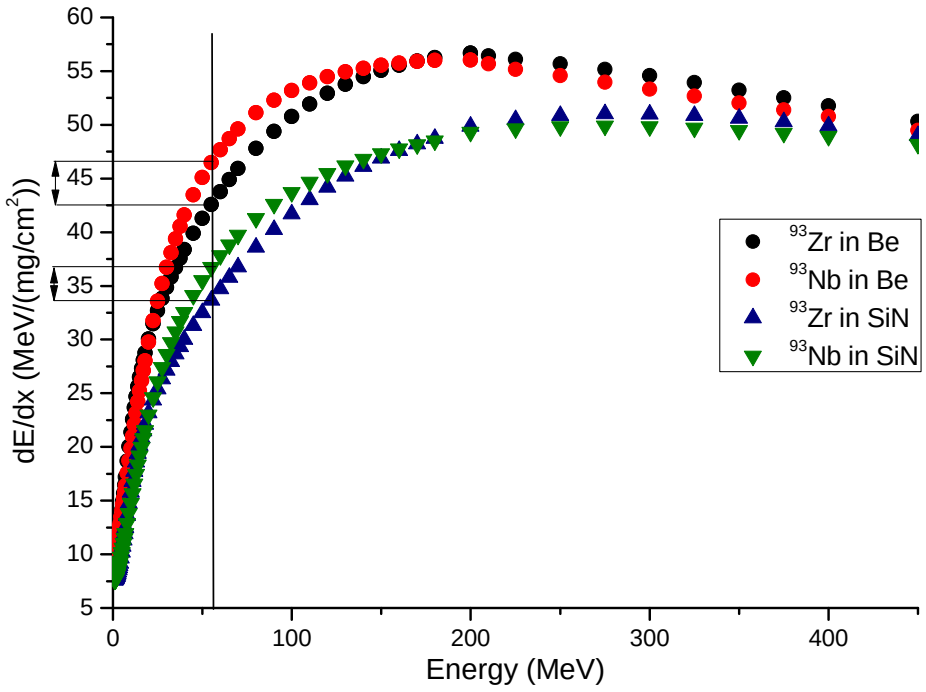

Figure 6.9.: Comparison of the Stopping Power of Zr and Nb in SiN and Be. An arbitrary energy was chosen (indicated by vertical black line) and the corresponding relative difference in stopping power of ^{93}Zr and ^{93}Nb was evaluated for SiN as well as for Be (indicated by black arrows).

separation in Be drops down to the level of SiN, which is caused by two reasons: On the one hand, the stopping power of ^{93}Nb approaches that of ^{93}Zr for small energies and on the other hand, the Yang-straggling increases to a much higher extent in the case of Be than of SiN (see Fig. 6.6). The ions in Be are slowed down to much smaller energies than ions having passed a SiN absorber of comparable thickness (compare Fig. 6.8(c) and Fig. 6.10(b)). Thus, the integrated area under the Yang-straggling curve for Be then prevail over the area under the curve for SiN.

It has to be kept in mind, that a certain final energy has to be left so that the ions can be detected, especially when we want to use the ionization chamber in addition. Hence, the final energy in case of the optimal thickness of Be obtained from the simulations of approximately 30 MeV would be too small, but similar to SiN it is expected that the maximal separation can be expected to be at lower thicknesses because of the intersection in the SRIM stopping power. Furthermore, even if not the optimal thickness of the Be absorber is used, Fig. 6.11 suggests that Be is nevertheless better suited to be used as passive absorber than SiN. However, it is known that SiN foils can be produced

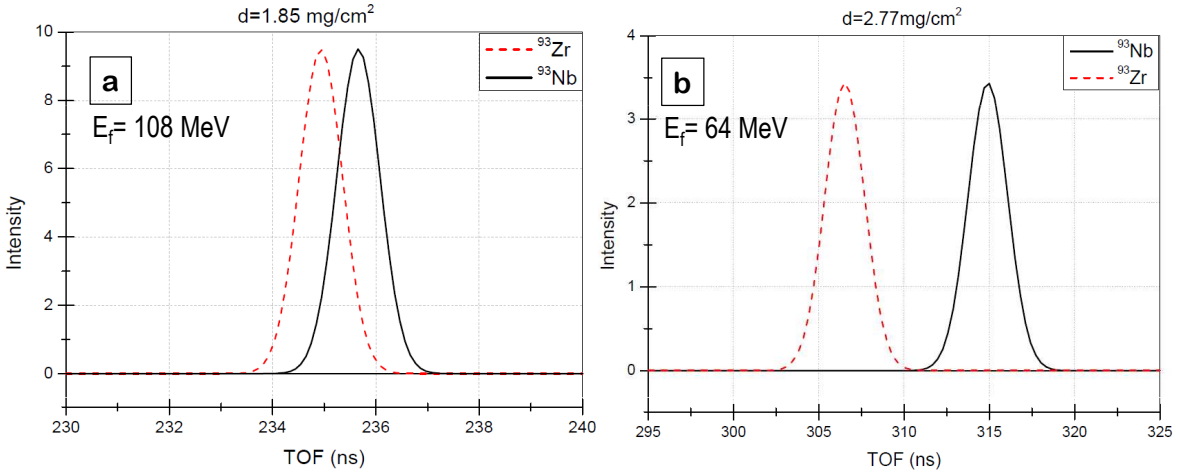

Figure 6.10.: Result of the simulations with TRIM03 for two different thicknesses of Be (a-b). The final energy E_f which corresponds to the TOF of the ^{93}Zr Gaussian, is given in the pictures.

with much higher uniformity than Be foils and thus, the straggling because of variations of the thickness should be much smaller. This additional straggling is not considered in the simulations and has to be tested experimentally. Therefore, both, SiN and Be were used as passive absorbers in the experiments.

6.2.3. Angular Straggling

Last but not least, also the angular straggling was studied with the help of the SRIM simulations. In Fig. 6.12(a) the angle distribution of ^{93}Zr ions leaving the SiN absorber is plotted for different thicknesses. It is evident, that the center of the distribution moves to larger angles with increasing thickness, since the number of collisions also increases. Consequently, also the deviation becomes larger which leads to a broadening of the peaks. This in turn means, that ions emitted under a rather large angle from the passive absorber miss the stop detector, which causes a lower transmission. In order to calculate the percentage of particles which can be detected by our STOP detector with a diameter of 2 cm, the angle distribution has to be convoluted with the spatial distribution of the beam behind the absorber, which is a Gaussian with its center on the beam axis. However, the corresponding width of several μm is negligible compared to the width of the spatial distribution at the STOP detector due to the angle distribution. For example, the maximum of the angle distribution for the 3.5mg/cm^2 thick absorber is located at an angle of 1° which corresponds to a radius of 5 cm for the TOF path of 2.9 m. For this reason, the absorber was assumed to be a point-like source. This simplifies the calculation to trigonometric considerations, which result in the radial intensity distribution at the STOP detector shown in Fig. 6.12(b). The vertical black

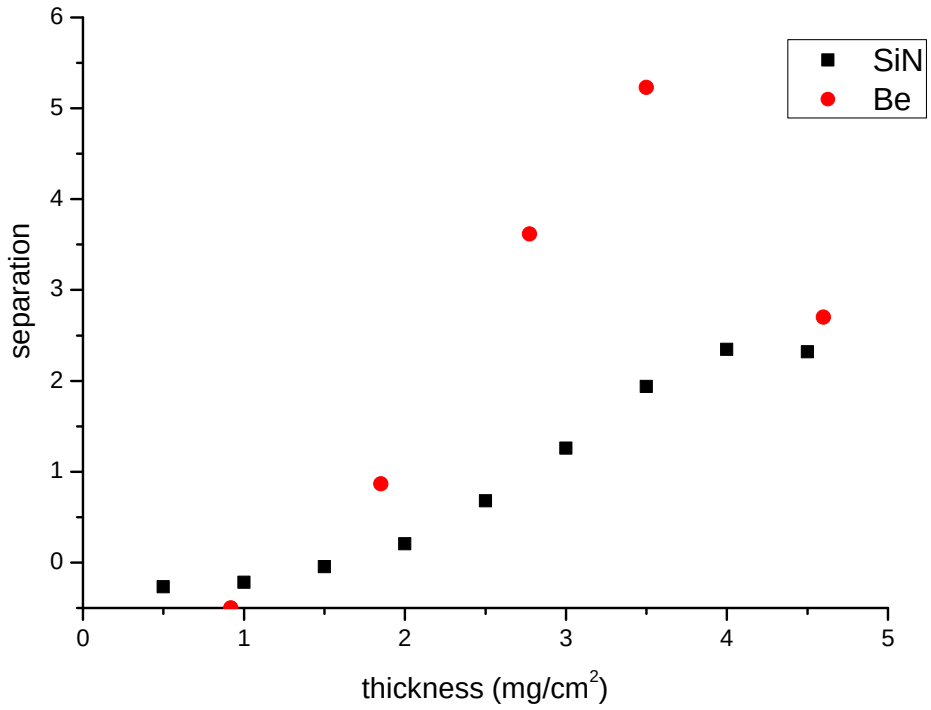

Figure 6.11.: Dependence of the separation S on the thickness of the absorber for Be and SiN. S was calculated with the data from the SRIM simulations, which leads to the negative values of S for small thicknesses. From this plot Be looks much more feasible as passive absorber than SiN.

line indicates the acceptance of our detector. To calculate the percentage of ions which can be detected with this active area, the respective curves have to be integrated from zero to the radius of our detector and have to be divided by the total area under the curve. The results obtained in this way are listed in Tab. 6.1.

For a thickness of 1.0 mg/cm^2 which is well below the calculated optimal thickness, the transmission already is very small. Assuming, that the transmission is 100% without any absorber, the further decrease in transmission by using an 2.5 mg/cm^2 thick SiN absorber instead of a 1.0 mg/cm^2 thick one is relatively small. Thus, we can conclude, that once a passive absorber is placed into the beam a further increase of the thickness does not worsen the transmission considerably, as long as the thickness is in the order of magnitude of the simulated thicknesses.

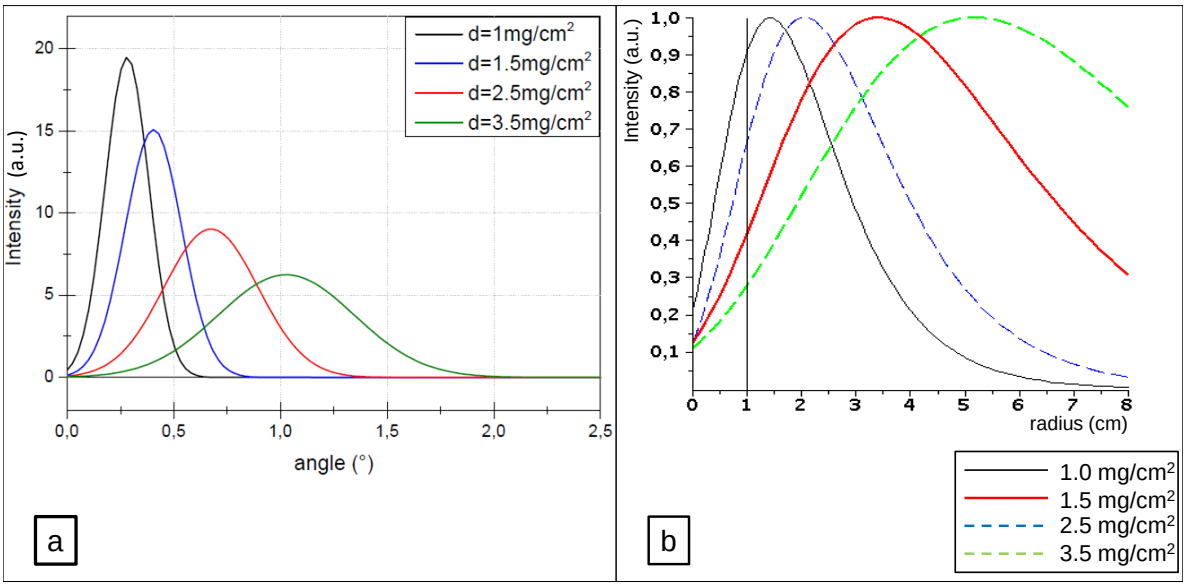

Figure 6.12.: (a) Angle distribution of ^{93}Zr ions at the exit of a SiN absorber, presented for different thicknesses, simulated with SRIM03. (b) Corresponding radial distribution of the ^{93}Zr ions at the entrance of the STOP detector.

thickness (mg/cm^2)	**Transmission** (%)
1.0	6.1
1.5	2.2
2.5	0.5
3.5	0.2

Table 6.1.: Theoretical transmission from the START to the STOP detector of the TOF path.

6.3. The Experiment

6.3.1. The Settings

For the experiment, a stack of SiN foils with the maximal available thickness of 1μm each were placed into a holder which in turn was fixed at a target ladder. SiN foils of a larger thickness are not produced by the supplier Silson Ltd., as intrinsic stress builds up and limits the stability of the foil. However, the use of a stack of thin foils instead of one thicker absorber provides a higher flexibility during the experiment. Since the thickness of the absorber for the optimal separation could not be exactly determined by the simulations, it had to be found out experimentally by varying the number of foils inserted into the beam. Fig. 6.13 shows a photography of the target ladder before it was installed in front of the START detector for the TOF path. The horizontal white

line indicates the lowest position which can be placed into the beam with the current setup. Two of the four positions available are equipped with different numbers of SiN foils and one position with a 10μm ($\hat{=}$1.85 mg/cm^2) Be foil. At the position left, a 4.3 mm aperture is installed for beam adjustment. In total, we investigated the energy loss of ^{92}Zr, ^{94}Zr and ^{93}Nb in a 10μm thick Be foil and in 6, 7, 8 and 13 foils of SiN, in order to determine the maximal separation.

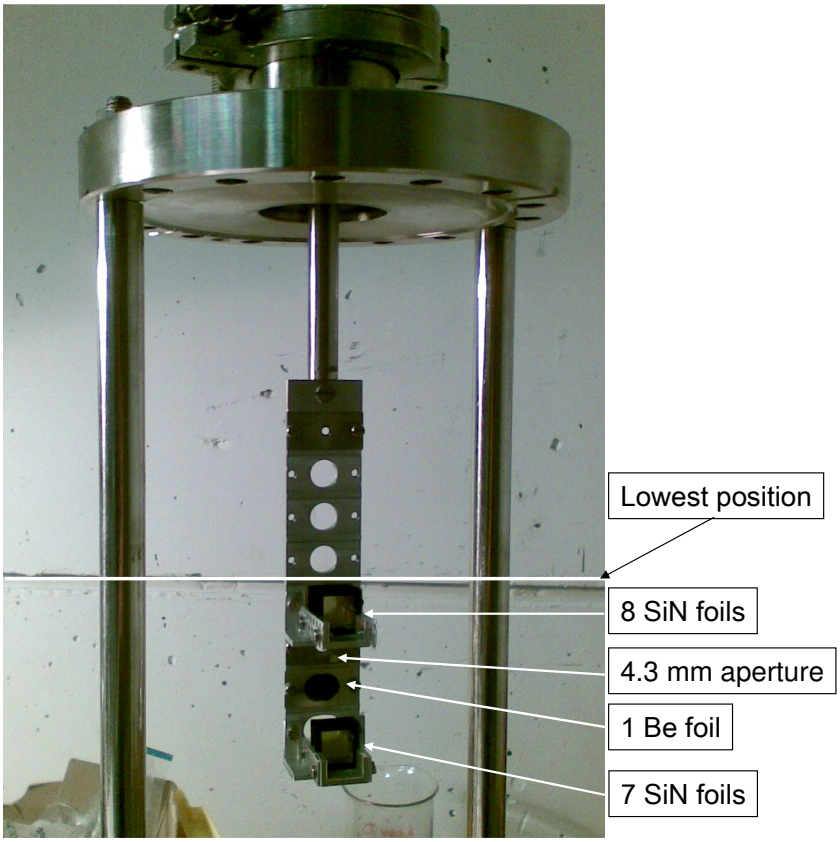

Figure 6.13.: Photo of target ladder with already installed passive absorbers, a Be foil and 2 different numbers of SiN foils. The horizontal white line marks the lowest position which can be placed into the beam.

When the magnetic rigidity of the transmitted ions is fixed, it is possible to compare the spectrum of ^{92}Zr, ^{94}Zr and ^{93}Nb. Even the use of the Blank sample where oxide ions are extracted, along with the Standard sample which was available as a Fluoride does not pose a problem, since the position of the ions in the detector have to be the same in both cases. For this purpose, the magnetic field of the analyzing magnet (B=767.893 mT) was kept constant when the setup was switched from one isotope to another. Consequently, the magnetic field of the Injector Magnet, the terminal voltage of the accelerator and the settings of the Wien filter were adjusted accordingly. In general, stable isotopes which give a measurable current at the Faraday cups in front of the detector, lead to a count rate in the detector considerably higher than 2 kHz which the ionization chamber cannot cope with. Therefore, an attenuator has to be placed in

the beam, which is a plate made out of tungsten with certain number of holes which determines the attenuation factor. There are 2 attenuators available, which reduce the count rate by a factor of 1000 each and one by a factor of 33. This factor has to be considered in the calculation of the concentration of the radioisotope.

Due to the uncertainties concerning the stopping power of ^{93}Nb and ^{93}Zr which were discussed in ch. 7.2, we decided to investigate the energy loss of the ions in the passive absorber at two different energies, i.e. we selected the charge states 14^+ and 15^+. Furthermore, we tested the influence of gas in the detector on the separation of ^{93}Nb and ^{93}Zr. In general, the use of the ionization chamber is preferable, since it provides 3 additional signals which can be evaluated to distinguish between the isobars. Otherwise, only the TOF and the E_{rest} signal of the surface-barrier-detector have to be sufficient for the separation.

6.3.2. Qualitative Discussion of the Measurement Results

In contrast to what was expected from the simulations and theory, the energy straggling of the Be foil (peak width of $^{92}Zr^{15+}$: σ=6.72 ns) observed in the experiment was much larger than the straggling caused by 6 SiN foils (peak width of $^{92}Zr^{15+}$: σ=0.57 ns) which have a comparable surface density. A spectrum of $^{92}Zr^{15+}$ events depending on their TOF and E_{rest} after passing through the Be foil is shown in the left picture of Fig. 6.14. For comparison, the corresponding spectrum of 6 SiN is given in the right picture Fig. 6.14. Both spectra were detected with a gas pressure of 11 mbar in the ionization chamber. From measurements without passive absorber, we were able to calibrate the TOF axis in ns and the E_{rest} axis in MeV, since in this case the energy and the TOF of the detected ions is known. Fig. 6.14 demonstrates that the energy loss of the $^{92}Zr^{15+}$ ions in Be is considerably larger than for SiN, which is in a good agreement with the results from the simulations (see ch. 6.2). The observation of a large energy straggling suggests a low uniformity of the Be foil with considerable variations of the thickness. This leads to an additional energy straggling that was already mentioned in ch. 6.1.2. It is obvious from Fig. 6.14, that the usage of the Be foil as passive absorber is not feasible due to the large peak width. Therefore, further experiments were done with SiN foils only. However, first measurements with a stable Zr isotope demonstrated, that the energy left after passing 13 SiN foils is not sufficient for the identification of the peaks with the ionization chamber. Furthermore, the peak width was also very broad, so that separation with 13 SiN foils was not further investigated, but we concentrated on 6, 7 and 8 SiN foils, which seemed much more promising.

From the measurements with the settings on ^{92}Zr and ^{94}Zr using a blank sample, the expected position of ^{93}Zr in the spectrum was determined by linear interpolation between the two detected isotopes. The difference between this calculated position and the actually detected ^{93}Nb ions was used to qualify the separation of ^{93}Zr and ^{93}Nb. In

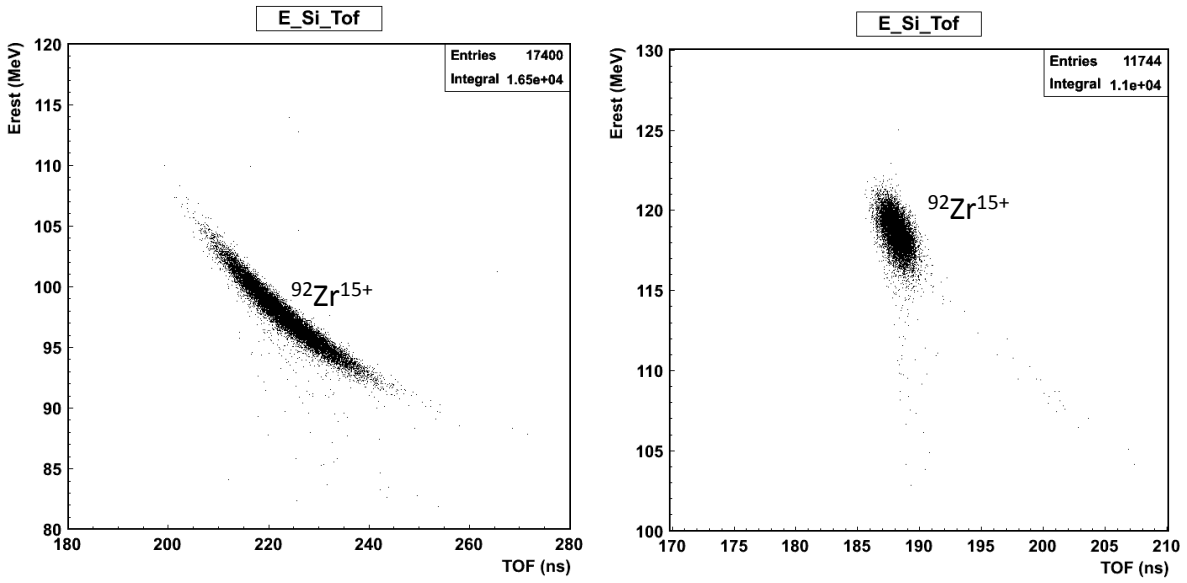

Figure 6.14.: Two Erest over TOF spectra of $^{92}Zr^{15+}$ after having passed a 1.85 mg/cm^2 thick Be foil (left picture) and a 1.8 mg/cm^2 thick SiN passive absorber, respectively (right picture). Especially the TOF distribution in case of the Be foil possesses a much broader width than the peak resulting from the SiN foils.

order to demonstrate the separation at the different settings graphically, the spectra of ^{92}Zr, ^{94}Zr and ^{93}Nb were superimposed in Fig. 6.15 and Fig. 6.16, where the first figure presents the measurements with charge state 15^+ and the second one those with charge state 14^+. Those two charge states correspond to an initial ion energy of approximately 193 MeV and 168 MeV. Each picture does not show one measurement with the settings to m=93 but three, which were done after another with the settings either on m=92, m=93 or m=94. The black square indicates the interpolated position of ^{93}Zr. The width of the square was taken to be $2 \cdot \sigma$ of the ^{92}Zr and ^{94}Zr peaks which is demonstrated in Fig. 6.15(d) using the example of a Zr^{92} TOF distribution. Consequently, the square represents only a fraction around the peak's maximum of the entire Zr^{93} distribution. In the Fig. 6.15(a-c) and Fig. 6.16(a-b) E_{tot} is plotted on the y-axis which is the sum of the rest energy E_{rest} detected by the Silicon detector and the energy loss ΔE in the ionization chamber. In Fig. 6.16(c) E_{rest} is plotted, since this spectrum was recorded without gas in the ionization chamber. Thus, in this case E_{tot} and E_{rest} are identical as there is no energy loss in the ionization chamber. ΔE itself is plotted in Fig. 6.16(d) for ions with an initial energy of 168 MeV and using 8 SiN as passive absorber.

In the green spectra, which corresponds to the settings on m=93, in addition to the ^{93}Nb in the center, peaks with a lower intensity in the upper right corner are visible. It can be assumed, that these counts are artefacts of ^{109}Ag which is also injected into the accelerator (compare ch. 4.2.1). However, those counts do not interfere at the po-

sition where $^{93}Zr^{15+}$ is expected and hence, do not pose a problem. Complementary to Fig. 6.15 and Fig. 6.16, Tab. 6.2 lists the relevant parameters for each of the measurements and the distance between the center of the measured ^{93}Nb peak and the interpolated ^{93}Zr peak for comparison.

picture	**# SiN foils**	**E (MeV)**	$p_{\mathbf{gas}}$ **(mbar)**	**ΔTOF (ns)**	$\Delta\mathbf{E_{rest}}$ **(a.u.)**
Fig. 6.15(a)	6	193	11	2.23	85.0
Fig. 6.15(b)	7	193	11	3.27	74.4
Fig. 6.15(c)	8	193	11	4.13	65.6
Fig. 6.16(a)	7	168	11	4.28	48.4
Fig. 6.16(b)	8	168	11	6.32	40.5
Fig. 6.16(c)	8	168	0	5.90	66.5

Table 6.2.: Settings during the measurements shown in Fig. 6.15 and Fig. 6.16, with # SiN foils being the number of SiN foils inserted into the beam, E the initial energy of the ions, p_{gas} the gas pressure in the ionization chamber. Additionally, the difference in TOF (ΔTOF (a.u.)), and the difference in E_{rest} (ΔE_{rest}), of the ^{93}Nb and the calculated ^{93}Zr peak center is listed.

It is obvious from the spectra and also from ΔTOF-column in Tab. 6.2, that a better separation in the TOF can be expected by using an initial energy of only 168 MeV. Though, the difference in E_{rest} decreases, because the energy of the ions itself is lower, the separation in all the plots of Fig. 6.16 seems to be increased with respect to the plots in Fig. 6.15 due to a larger difference in the TOF. However, this suggests the conclusion, that the 'share' in the difference in stopping power of higher energies is negligible or even negative. Consequently, this observation can be better explained with a stopping power curve as it is implemented in the SRIM03 program (see ch. 6.2). The only possibility to verify this observation, is to detect actual ^{93}Zr ions at varying energies in order to experimentally determine the corresponding stopping power curve. For this purpose, we first have to be able to definitely identify the ^{93}Zr events, where a first approach was done with this work.

Within the uncertainties, there is no difference in the separation of ^{93}Zr and ^{93}Nb regarding to the TOF between a measurement with 11 mbar gas pressure in the ionization chamber (Fig. 6.16(b)) and without gas in the chamber (Fig. 6.16(c)). However, the background due to ^{92}Zr and ^{94}Zr seems to be reduced in the second case. The advantage of applying a gas pressure in the ionization chamber is that we have an additional dE signal on which we can apply a window for ^{93}Zr (compare ch .6.3.4). Fig. 6.16 (d) shows that the separation of ^{93}Nb and the region of interest is very good, but mainly with respect to the TOF. In general, the distance between the maximum of the ^{93}Nb peak and the calculated center of the ^{93}Zr distribution is increasing with increasing number of SiN foils. This is rather hard to see in the spectra, but whereas the ^{93}Nb peak shows the same TOF as the ^{94}Zr peak in Fig. 6.15(a), it is shifted to higher TOF

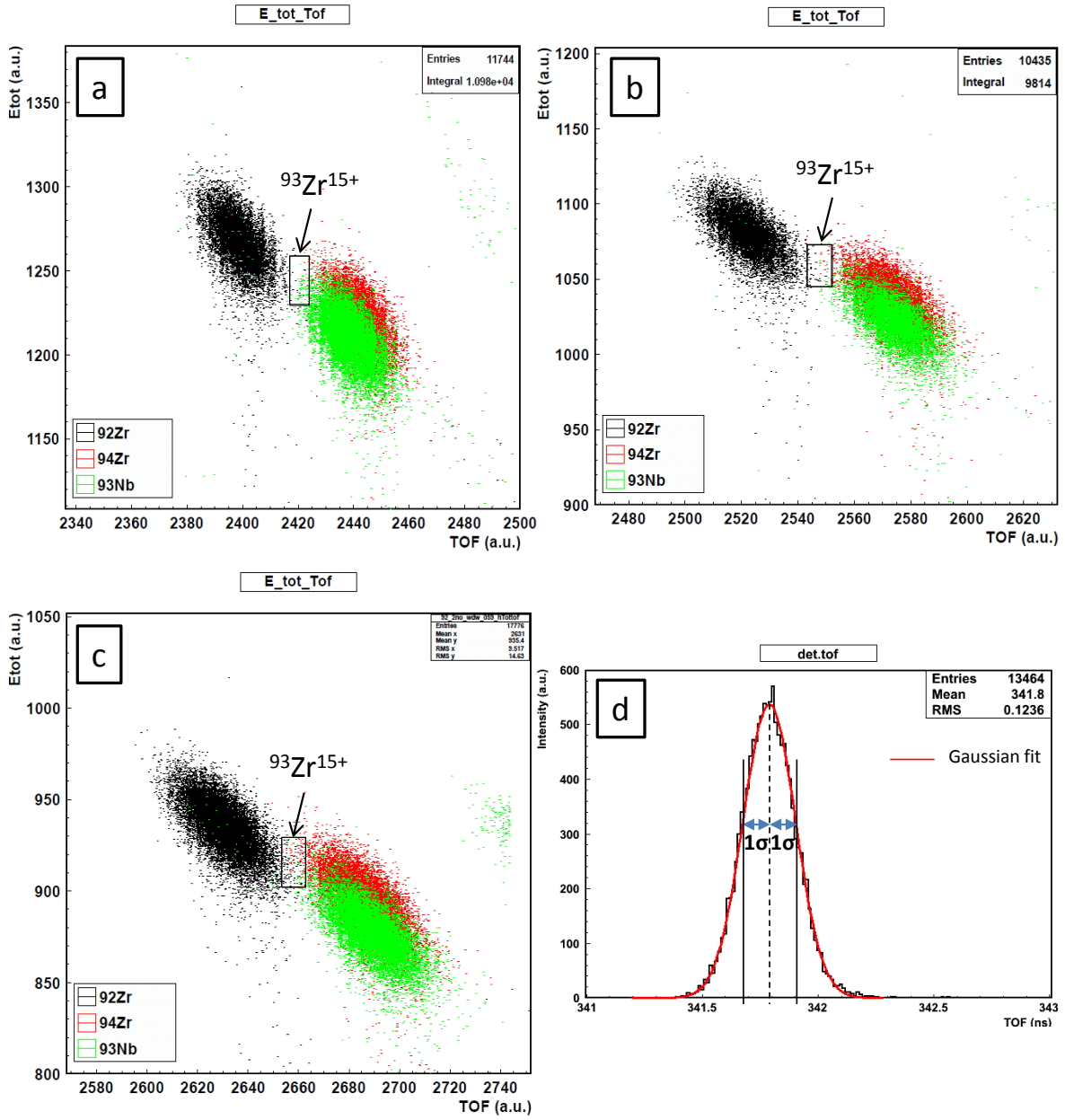

Figure 6.15.: Superimposed are the spectra obtained from the measurements with settings on m=92 amu (black), m=94 amu (red) and m=93 amu (green) with an initial ion energy of 193 MeV using 6 SiN foils (a), 7 SiN foils (b) and 8 SiN foils (c). A gas pressure of 11 mbar isobutane was applied in the ionization chamber. Picture (d) demonstrates the choice of the region of interest, indicated by the black square in picture (a-c). The black square indicates the expected position of $^{93}Zr^{15+}$. 8.6 a.u. on the x-axis correspond to a TOF of 1ns and 27 a.u. on the y-axis correspond to 1 MeV E_{rest}.

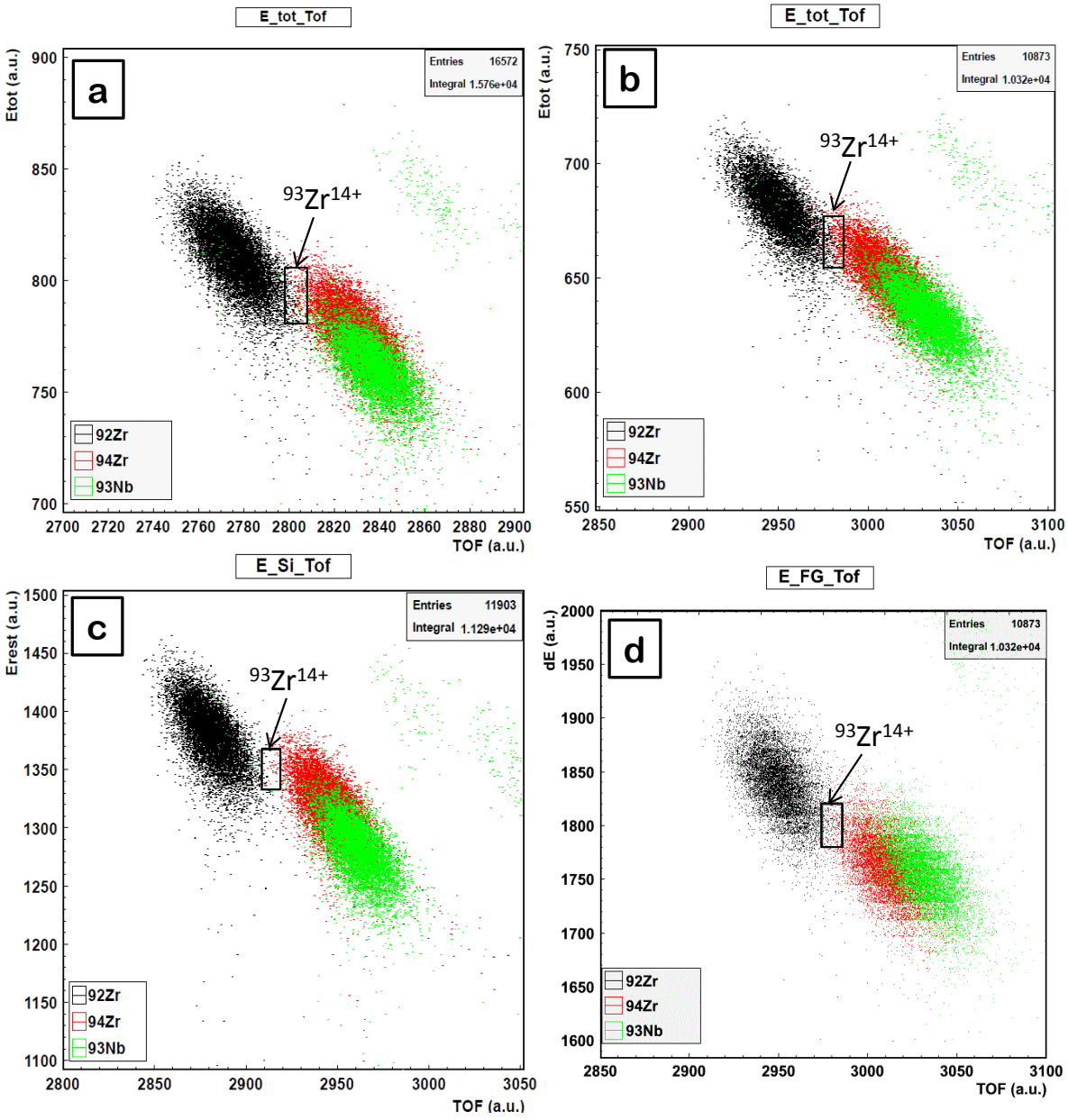

Figure 6.16.: Superimposed are the spectra obtained from the measurements with settings on m=92amu (black), m=94amu (red) and m=93amu (green) with an initial ion energy of 168 MeV using 7 SiN foils (a), 8 SiN foils (b) and 8 SiN foils (c). A gas pressure of 11 mbar isobutane was applied in the ionization chamber for picture (a) and (b) whereas (c) was detected without gas in the ionization chamber. Picture (d) presents the energy loss signal dE versus TOF spectrum for 8 SiN foils. The black square indicates the expected position of $^{93}Zr^{14+}$. 8.4 a.u. on the x-axis correspond to a TOF of 1ns and 28 a.u. on the y-axis correspond to 1 MeV E_{rest}.

with respect to the center of the ^{94}Zr distribution. The same behaviour can be observed in Fig. 6.16(a) and (b).

To sum up, one can conclude from this very qualitative considerations, that the best choice for the detection of ^{93}Zr are 8 SiN foils, using an energy of 168 MeV and no gas in the detector. However, it has to be kept in mind, that so far there was no normalization on time or the ion current, so that measurements with different statistics (but differing less than one order of magnitude) were compared, leading to a quite subjective comparison. For this purpose, usually the transmission from the cup where the current of a stable Zr isotope is measured to the detector has to be determined. However, the currents of stable isotopes we could extract from the ion source were particularly low (5 nA of ^{109}Ag at Cup 1). Although, this was an advantage for the runs with the settings on mass 93 amu since we did not have to use an attenuator to stay below a rate of 1 kHz, the currents in the Actinide beamline were hardly measurable. Therefore, we decided to normalize the events in the ionization chamber to the number of ^{92}Zr at the channel plate, the START detector of the TOF measurement. Hence, the following chapter describes the determination of the transmission from the START to the STOP detector.

6.3.3. Transmission from the START to the STOP detector

As explained in ch. 4.3 the transmission of the setup, which is necessary to calculate the concentration of the radioisotope in the sample from the events in the detector, can be determined with the help of a standard sample. The low transmission calculated from the angle distribution of the SRIM simulations of 0.5 % to 6 % because of angular straggling should be verified experimentally. Due to the low currents, we decided to insert the standard sample with the higher ^{93}Zr concentration of $3.1 \cdot 10^{-8}$ (compare ch.5.3). Unfortunately, no $^{93}Zr^{15+}$ event could be detected before the measurement had to be stopped after approximately one hour because of technical problems on the low energy side. The corresponding E_{rest} versus TOF spectrum is presented in red in Fig. 6.17 superimposed on a spectrum of a ZrO^- blank spectrum(in black) extracted from a ZrO_2 sample with the settings also on m=93 amu. The black square again indicates the position where we would have expected the ^{93}Zr events, but in which no events from the standards are located. The second intensive peak in the ZrO^- blank spectrum is again assumed to originate from ^{109}Ag events (see ch. 4.2.1). The accumulation of events left of the ^{93}Nb peak in the ZrF^- spectrum are located at a distance to the region of interest, so that those events do not come into consideration as ^{93}Zr events. The current data suggest, that those events are scattered ions.

However, there is one event from the standard sample which is very close to the expected position of $^{93}Zr^{15+}$. How do we know, that this count is not a real ^{93}Zr event but belongs to the background? Actually, we cannot tell definitely, but a simple estimation shows,

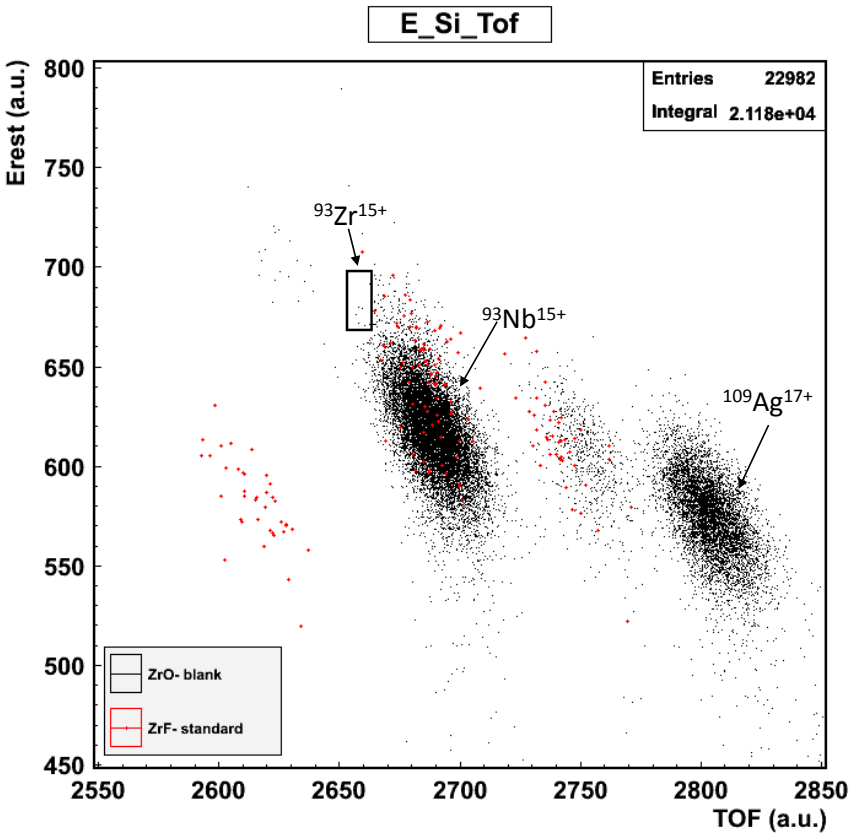

Figure 6.17.: Spectrum of a ZrF_4 standard sample with a concentration of $3.1 \cdot 10^{-8}$ (in red) superimposed onto a spectrum of a ZrO_2 blank sample (in black). 8.06 a.u. on the x-axis correspond to a TOF of 1ns and 25 a.u. on the y-axis correspond to an energy of 1 MeV. The black square indicates the expected position of $^{93}Zr^{15+}$, in which no event from the standard is located. The standard sample could only be measured for a short time (1h) at a low count rate.

that statistically there was only a small probability for ^{93}Zr counts from the standard sample within the measured time. Since the rate of ^{93}Zr events R(^{93}Zr) is related to the rate of Zr events in total R(Zr) by the known concentration c(^{93}Zr), the following equation can be set up:

$$\frac{R(^{93}Zr)}{c(^{93}Zr)} = \frac{R(^{94}Zr)}{c(^{94}Zr)}. \tag{6.21}$$

With the rate of ^{94}Zr events R(^{94}Zr) from the run done before the standard measurement and the isotopic ratio c(^{94}Zr)=17.38% inserted into the equation, a rate of $1.2 \cdot 10^{-4}$

^{93}Zr events per second is obtained. Based on a Poisson distribution of N events

$$P(N) = \frac{\lambda^N}{N!} \cdot e^{-\lambda} \tag{6.22}$$

where λ corresponds to the rate of ^{93}Zr events per hour, we arrive at an probability of 27.9% for detecting one event after measuring 1 h.

Therefore, it is not possible to use this measurement of the standard to monitor the transmission. Instead, we used the ^{93}Nb events for this purpose, assuming equal negative ion yield from the ion source for NbO^- and ZrO^- [53]. In order to do this, first, the ^{93}Nb concentration in the ZrO_2 sample had to be determined. This was estimated by relating the rate of ^{93}Nb to the rate of ^{92}Zr or ^{94}Zr events similar to eq. (6.21), which is only reasonable for measurements done with similar conditions (e.g. same charge state, same number of SiN foils, etc.). The number of events of each isotope was obtained by fitting the respective peaks in the E_{rest} over TOF spectra with a Gauss fit. Thus, eq. (6.21) can be rewritten accordingly

$$c(^{93}Nb) = \frac{R(^{93}Nb) \cdot c(^{94}Zr)}{R(^{94}Zr)}. \tag{6.23}$$

which leads to a ^{93}Nb concentration in the ZrO_2 of $(15.0 \pm 8.3)\,\mathrm{ppm}^2$ averaged over all evaluated runs. The error given is the standard deviation due to the averaging.

Now, we have a sample with a defined concentration of ^{93}Nb, which means we can apply the procedure, which was described in ch. 4.3 to the ^{93}Nb distribution. Hence, the Transmission T is now defined in the following way:

$$T = \frac{\text{rate of } ^{93}\text{Nb ions in the window}}{\text{rate of } ^{93}\text{Nb at the channel plate detector}} \tag{6.24}$$

Consequently, a window which is applied to the ^{93}Zr distribution, has to be applied to the ^{93}Nb distribution in exactly the same way as well. Therefore, it is reasonable to define windows for ^{93}Zr always with respect to the maximum of the Gaussian, so that this window simply has to be shifted to the maximum of the ^{93}Nb distribution, to calculate the corresponding transmission. In order to calculate the rate of ^{93}Nb at the channel plate detector, eq. (4.13) has to be adapted accordingly

$$R(^{93}Nb) = \frac{c(^{93}Nb) \cdot N(Zr)}{t} = \frac{c(^{93}Nb) \cdot (R_i(^{94}Zr) + R_f(^{94}Zr)/2}{17.38\%} \tag{6.25}$$

where $\mathrm{R}_i(^{94}\mathrm{Zr})$ and $\mathrm{R}_f(^{94}\mathrm{Zr})$ are the rates of ^{94}Zr measured at the channel plate detector before and after the run with settings on m=93 amu and t denotes the time. The results for the transmission which were obtained in this way are listed in Tab.6.3, where d is the total thickness of the SiN passive absorber, q the selected charge state and $\mathrm{p}_{\mathrm{gas}}$ the gas pressure in the ionization chamber. The reasonable transmission of 77% without passive

# SiN foils	d (mg/cm^2)	E (MeV)	p_{gas} (mbar)	transmission (%)
0	-	193	11	**77**
6	1.8	193	11	**5.0**
7	2.1	193	11	**3.2**
7	2.1	193	11	**7.6**
8	2.4	193	11	**6.2**
7	2.1	168	11	**5.1**
8	2.4	168	11	**1.8**
8	2.4	168	0	**1.6**

Table 6.3.: Transmission from the CP to the ionization chamber in %, depending on the number of SiN foils (# SiN foils), the total thickness of the SiN foils (d), the initial energy of the ions (E) and the gas pressure in the ionization chamber (p_{gas}).

absorber but with the 4.3 mm aperture placed into the beam, justifies the presented method to determine the transmission by using the ^{93}Nb distribution.

As it was expected, the small angular scattering in the SiN foils lead to a considerable broadening of the beam spot and therewith to a reduction of the transmission compared to the measurements where the 4.3 mm aperture was placed into the beam. The listed transmissions with a passive absorber are all in the same order of magnitude and are in a reasonable agreement with the values obtained from the simulations in ch. 7.2.3. However, it has to be noticed that there is only a small decrease of the transmission if one SiN foil is added. By contrast, there will be a considerable decrease in transmission when the windows drawn in Fig. 6.15 and Fig. 6.16 are applied on the spectra. This is quite evident if those windows are imagined to be placed on the center of the ^{93}Nb peak, which then cut out only a small fraction of the total ^{93}Nb events and hence, decreases the transmission accordingly. Since the aim was to develop a method for the detection of ^{93}Zr, we were not short of sample material, so that a small transmission was considered a secondary issue.

From a theoretical point of view, there is no explanation why the transmission should be lower with no gas in the ionization chamber than with gas. It is to be expected, that the transmission of the last two line in Tab. 6.3 should be at least equal. Consequently, this deviation can be considered as uncertainty of the transmission and hence, give the order of magnitude of the corresponding error.

[2]ppm: parts per million.

6.3.4. Upper limit of ^{93}Zr concentration

Since we did not detect any ^{93}Zr event we are only able to present an upper limit of the ^{93}Zr concentration in the samples by choosing the windows such, that they are free from background. In this case, that gives us a minimal concentration of ^{93}Zr which we could distinguish from background and hence, would be measurable with the current settings. Consequently, this is a more objective way to evaluate the measurement results shown in Fig. 6.15 and Fig. 6.16. In general, this concentration is calculated as it was explained in ch. 4.3, but with the measured currents of the stable isotope replaced by its count rate at the channel plate. As already pointed out, the counts in the window, N(^{93}Zr), of a blank sample is zero if the windows are chosen correctly which, of course, corresponds to a concentration of zero, too. Since this is a low-statistics problem, it is not possible to estimate the dominating statistical error (ΔN(^{93}Zr)) according to the error of the Gauss distribution

$$\Delta N(^{93}Zr) = \pm\sqrt{N(^{93}Zr)}, \tag{6.26}$$

but the error interval according to Feldman and Cousins [74] at a $1\,\sigma$ ($\hat{=}\,68.27\%$) confidence level has to be used. Thus, the detection of zero events corresponds to an error interval from 0.00 to 1.29 events. The resultant error of the concentration is then calculated by quadratic error propagation, where the upper limit of the error interval is equivalent to the detectable concentration of ^{93}Zr and is therefore denoted by c(^{93}Zr). Tab. 6.4 lists the obtained results of c(^{93}Zr) for the corresponding pictures in Fig. 6.15 and Fig. 6.16 along with the relevant parameters, such as the initial kinetic energy of the ions E, the gas pressure p_{gas}, the rate of Zr ions at the channel plate, R_{CP}(Zr), and the transmission T for the corresponding set of windows.

picture	**# SiN foils**	**E (MeV)**	**p_{gas}** (mbar)	**R_{CP}(Zr)** (Hz)	**T (%)**	**c(^{93}Zr)**
Fig. 6.15(a)	6	193	11	$6.8 \cdot 10^7$	0.0036	$\mathbf{2.0 \cdot 10^{-7}}$
Fig. 6.15(b)	7	193	11	$6.8 \cdot 10^7$	0.073	$\mathbf{1.3 \cdot 10^{-8}}$
-	7	193	11	$1.6 \cdot 10^6$	1.5	$\mathbf{5.0 \cdot 10^{-8}}$
Fig. 6.15(c)	8	193	11	$3.1 \cdot 10^6$	0.66	$\mathbf{1.5 \cdot 10^{-8}}$
Fig. 6.16(a)	7	168	11	$1.0 \cdot 10^7$	0.99	$\mathbf{1.1 \cdot 10^{-8}}$
Fig. 6.16(b)	8	168	11	$1.3 \cdot 10^7$	0.56	$\mathbf{7.0 \cdot 10^{-9}}$
Fig. 6.16(c)	8	168	0	$4.9 \cdot 10^6$	0.65	$\mathbf{5.7 \cdot 10^{-9}}$

Table 6.4.: Upper detection limit for ^{93}Zr (last column) along with the corresponding count rate of Zr at the CP (R_{CP}(Zr)), the transmission of the final set of windows (T) and the used settings (see text for further explanations).

The results are grouped according to the settings and changes of the setup, e.g. between the first two groups the beamline had to be opened to replace the 6 SiN foils by 8 and WFI and II were off line in the first group. Therefore, 7 SiN foils are listed twice,

but with a different upper detection limit. The second measurement leads to a higher detection limit since the zero counts in the window are compared to a smaller rate of Zr ions, although the transmission is considerably larger. If the transmissions are compared to the values given in Tab. 6.3, the transmission of the first group has decreased to a higher extent than the other groups which indicates that in the first case the windows had to be chosen more restrictive to achieve the aim of being background-free. In general, the upper detection limit calculation confirms the observation which were made from Fig. 6.15 and Fig. 6.16, that the background at the expected position of ^{93}Zr is lowest if the charge state 14+, i.e. an initial energy of 168 MeV and 8 SiN foils are chosen.

It has to be kept in mind, that the concentrations given in the last column of Tab. 6.4 must not be taken as absolute values as only the statistical error is considered. However, there are several other uncertainties which were not taken into account, since many quantities as the transmission and the concentration of ^{93}Nb only are estimates. The determination of the ^{93}Nb concentration for example, assumes that Nb ions are extracted from the ion source in the same way as Zr ions. Although we cannot proof this, it can be expected since both elements show a very similar chemical behaviour and previous investigations observed a similar behaviour in the ion source with respect to the molecule formation [53]. Furthermore, as already pointed out, the ion source was quite unstable in this beamtime, which has a considerable influence on the particle currents. Therefore, an exact error analysis is not reasonable as it is hard to estimate the error corresponding to the mentioned uncertainties. Consequently, the values given for the upper detection limit in Tab. 6.4 shall demonstrate the order of magnitude only and can only be compared relative to each other.

7. Measurements with the GAMS

Previous measurements of ^{93}Mo with the GAMS, which has a very similar isotopic and isobaric background situation as ^{93}Zr, were very promising. An upper concentration limit of ^{93}Mo/^{92}Mo $< 10^{-9}$ could be measured [75]. Therefore, we did complementary measurements with the GAMS setup in addition to the measurements using a passive absorber in order to detect ^{93}Zr. However, those measurements have not been finished, yet. The primary aim of this first experiment to clearly identify the position of ^{92}Zr, ^{94}Zr and ^{93}Nb and to deduce a region of interest for ^{93}Zr. Similar to the approach which was chosen for the passive absorbers, this region of interest should be calculated from the center and width of the ^{92}Zr and ^{94}Zr peaks by linear interpolation. With this expected position of ^{93}Zr the distance to the center of the ^{93}Nb distribution should be investigated qualitatively at varying parameters such as pressure in the detector and in the Gas-filled Magnet (GFM) and the energy of ions according to the discussion in ch. 4.2.2 and in [46]. Furthermore, the GFM provides the opportunity to suppress the isobar if the magnetic field is chosen correctly, since then the ^{93}Nb ions are prevented from reaching the ionization chamber by an aperture due to their higher magnetic rigidity. However, Fig. 4.6 already suggests, that the difference in the magnetic rigidity is quite small, so that we are not able to shift the ^{93}Nb events completely out of the spectrum without loosing a considerable part of the ^{93}Zr distribution.

Since the ^{93}Nb count rate has a large share in the total count rate of particles with m=93 amu, its reduction by the GAMS has the additional advantage, that higher currents of ions with m=93 amu can be extracted from the ion source compared to the measurements with the passive absorber. In this way, higher count rates of the radioisotopes could be detected without having to use an attenuator to protect the ionization chamber, which could lead to scattered particles. Consequently, the suppression of ^{93}Nb depending on the magnetic field was investigated. For this purpose, no quantitative measurement of a ^{93}Zr sample was done, but blank samples only were used.

7.1. The settings

In this beamtime, we tested ZrH_2 as blank material, which was extracted from the ion source as ZrH^- (compare ch.5.2). In accordance to the discussion in ch. 4.2.4 we

chose the high charge states of 15^+ and 16^+ which corresponds to energies of 198 and 225 MeV, although the expected stripping yield is only 2.45% and 0.95%, respectively. The low stripping yields even were an advantage in this case as the count rate of ^{93}Nb was reduced, so that we were able to detect the full ^{93}Nb distribution without having to use attenuators. Thus, all measurements of ions with a mass of 93 amu could be done without attenuators. We recorded spectra for 2 different gas pressures in the detector, 45.7 and 48 mbar. In general, one would assume, that a higher pressure leads to a better separation. However, if the density of the gas is too high, in the worst case both isobars are already stopped in the fifth segment (see Fig. 4.7) of the anode and hence both naturally deposit an energy there which is equal to zero. Thus, the last segment E5 does not provide any information about the separation and cannot be used to set windows. Furthermore, we tried the three different gas pressures of 3.5, 4.5 and 5.5 mbar in the GFM in order to study its effect on the separation in the ionization chamber.

Both Wien filters located before the switching magnet were used for these measurements. However, Fig. 7.1 demonstrates, that WFI and WFII were not sufficient to completely suppress the isotopic background, since there are two different species of events to be seen in this E2 versus position spectrum, although the setup was adjusted to m=93 amu. As charge state 16^+ was chosen and the detector pressure was set to 45.7 mbar. In order to identify the two peaks, we inserted a Tantalum sample into the ion source, which is a chemical homologue to Niobium, which means that an increased concentration of Nb can be expected but no Zr. Those measurements with the settings on m=93 showed a peak at the same position in the spectrum as the peak with the lower E2 value, which suggests that these events are $^{93}Nb^{16+}$ events. With the settings on m=92 amu using again a ZrH_2 blank sample, we detected a peak at the position of the upper peak. However, the peaks of the respective isotopes are positioned very close together and thus, a proper identification of the events is quite difficult from this spectrum which is why a question mark is put on the labels in Fig. 7.1. It has to be mentioned, that the separation in the rest of the energy loss segments is even worse. Furthermore, there ought to be also ^{94}Zr events, since they are injected into the accelerator as metallic $^{94}Zr^-$ ions because of the use of Zirconium Hydrides. In order to separate the events originating from different masses, the TOF path in front of the GAMS was added. For a fixed magnetic rigidity of the beam guiding system we can clearly identify the peaks corresponding to the masses m=92 amu, m=93 amu and m=94 amu with the help of the expression

$$\frac{m \cdot l}{q \cdot TOF} = \text{const.} \tag{7.1}$$

In the TOF spectrum presented in Fig. 7.2 which was recorded with the settings on $^{93}Nb^{16+}$, the three peaks are labeled accordingly. The width of the peaks in this spectrum of approximately 480 ps FWHM could be further decreased to 260 ps FWHM by using a Pico-Timing Discriminator in the electronics for the data processing. This TOF spectrum demonstrates, that both neighbouring isotopes reach the ionization chamber.

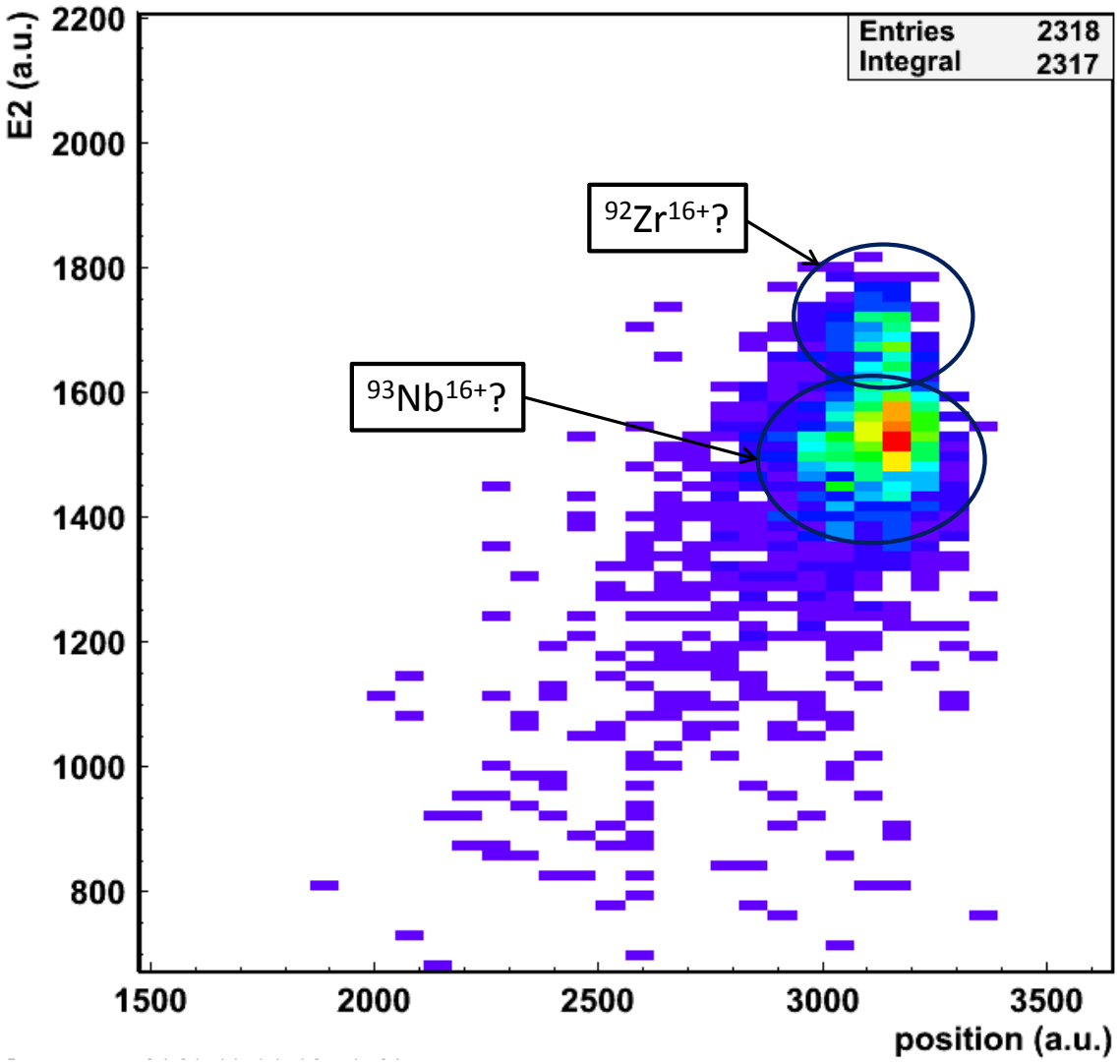

Figure 7.1.: 2 dimensional spectrum (E2 versus position) of the detected events with the settings on m=93 amu. Two different species of events are visible and are marked with black circles. The identification of the peaks was based on the measurement of a Tantalum sample and of the ZrH^- with the settings on m=92 amu and has to be verified. For further explanations see text.

Thus, the ^{94}Zr have also to be present in Fig. 7.1, but probably are covered by the ^{93}Nb events. Since the peaks of the three masses are very well separated from each other, we are now able to select only those events with m=93 amu by applying a window on the peak in the middle. A possible choice of this window is represented by the two vertical black lines in Fig. 7.2. Similar to the procedure explained in the chapter on the passive absorber, events with m=93 amu in the wings of the Gauss distribution are neglected which reduce the transmission from the channel plate detector to the ionization chamber. However, this procedure ensures that the isotopic background is efficiently

suppressed in the spectra of the ionization chamber.

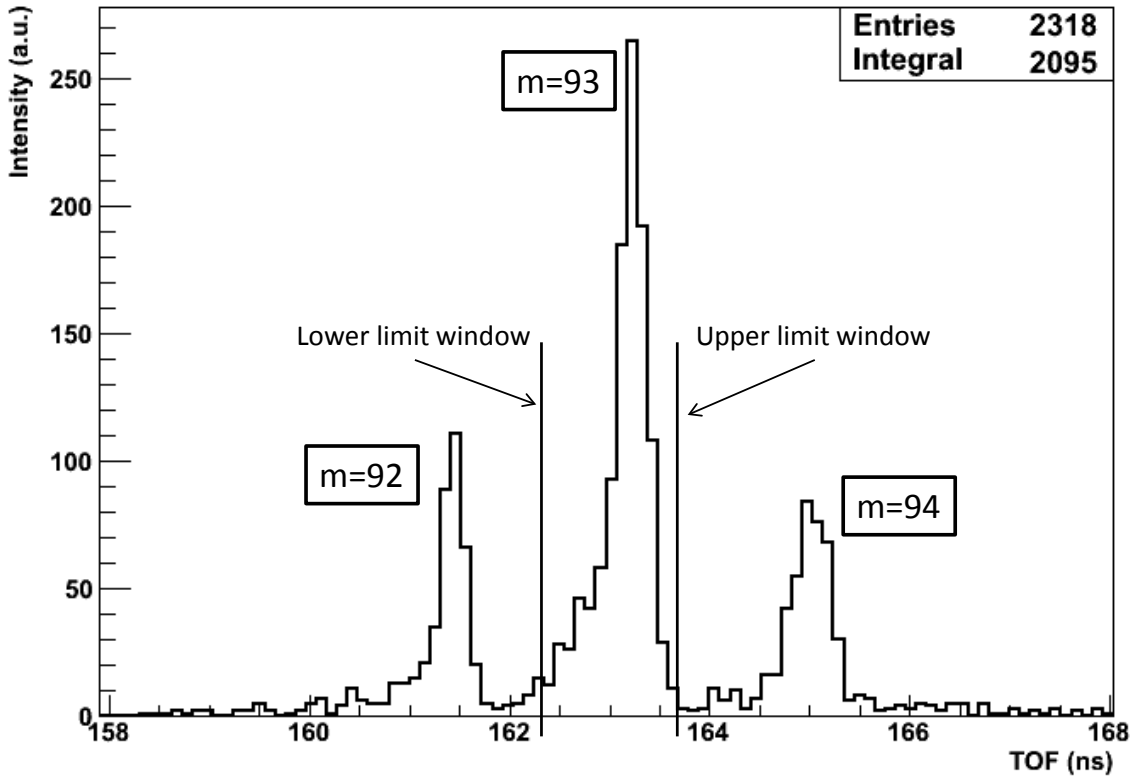

Figure 7.2.: TOF spectrum corresponding to the spectrum shown in Fig. 7.1. The three peaks of m=92 amu, m=93 amu and m=94 amu are labeled. The two vertical black lines indicate a possible choice of the limits for a window on m=93, to reject the isotopic background.

7.2. Results

Fig. 7.3 shows the resulting E2 over position spectrum, if the window indicated in Fig. 7.2 was applied to the spectrum in Fig. 7.1. Only one peak is left, which has then to correspond to the ^{93}Nb ions. Similar to the distributions in Fig. 7.1, also the present one has a rather long tail towards lower energies and larger radii corresponding to smaller positions in the spectrum (compare Fig. 4.7) which is due to scattering of the ions on the gas molecules of the GAMS. By repeating this procedure for the masses 92 amu and 94 amu, the position of the two isotopes in all the available spectra (E1-E5 over position) can be obtained and hence, we could calculate a region of interest for the ^{93}Zr events by linear interpolation which is indicated by the black square in Fig. 7.3.

The width was chosen to be 1σ in each direction, which was calculated from the width of the ^{92}Zr and ^{94}Zr distributions. It became obvious, that the peak of ^{94}Zr is located at the same energy as ^{93}Nb and at a slightly smaller position. Consequently, the peak labeled with '^{93}Nb' in Fig. 7.1 actually is composed of the two peaks of ^{93}Nb and ^{94}Zr. Thus, the 1 sigma region of interest for ^{93}Zr is also positioned on the wing of the ^{93}Nb

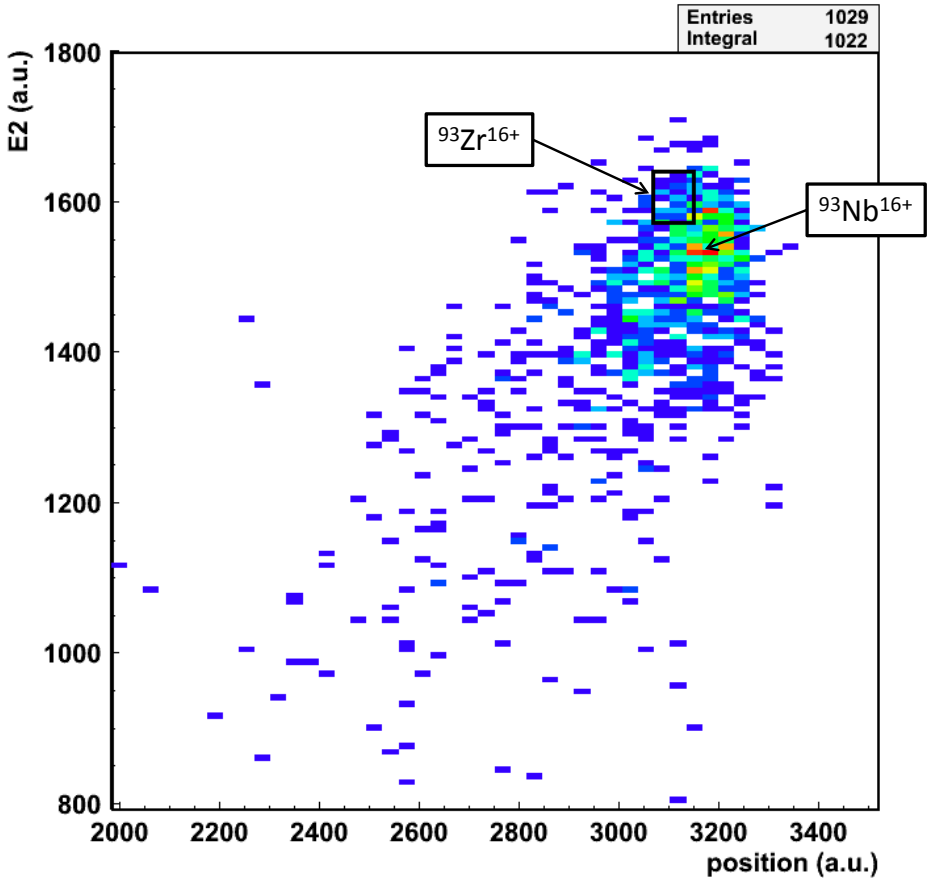

Figure 7.3.: E2 versus position spectrum of Fig. 7.1 after a window was placed on the peak corresponding to the events with m=93 amu in Fig. 7.2. Only the peak of ^{93}Nb is left, since events with different masses are discarded. This peak has a long tail towards smaller energies and larger radii caused by scattered ions. The black square indicates the expected position of ^{93}Zr with a $1\,\sigma$ confidence level.

distribution. The spectra of the other energy signals look similar, so that it is very difficult to obtain a background-free spectrum for the detection of ^{93}Zr with this set of windows which is centered around the interpolated maximum of the ^{93}Zr peak.

Since the background is only interfering from one direction, it is more promising to shift the window to the wing of the ^{93}Zr distribution which is opposite of the background. In order to demonstrate this graphically, Fig. 7.4 shows two Gaussians depending on the

energy which represent the ^{93}Nb distribution in Fig. 7.3 and a possible ^{93}Zr distribution projected onto the energy axis. The amplitude of the two distributions was chosen arbitrarily. The yellow area in the left picture demonstrates the current choice of the window on E2, where we expect a huge level of background due to the very close ^{93}Nb peak. The corresponding peak-to-background ratio of A(^{93}Zr)/A(^{93}Nb)=2.0 can be estimated by integrating both peaks in the limits of the window. If we now shift this window to the left wing of the ^{93}Zr peak which is presented in the right picture, we are able to significantly reduce the background by 98 % compared to the original choice of the window. Since we have background coming only from the low energy side, we can further expand the window to lower energies to increase the transmission, which explains the larger width of the window. This leads to a considerably improved peak-to-background ratio of A(^{93}Zr)/A(^{93}Nb)=19.3. However, even if the larger window is applied, the transmission is only approximately 20 % of that in the left picture. As it was explained in the chapter about the measurements with a passive absorber, this is not a problem in the first place, since for the development of the method there is enough material available.

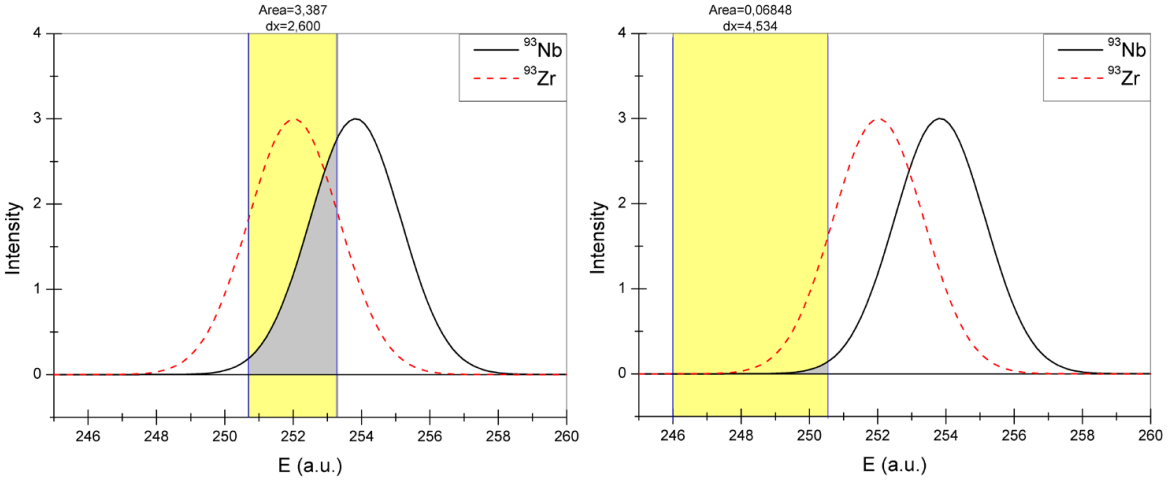

Figure 7.4.: The two pictures demonstrate, how the level of background (grey shaded area) due to a closely positioned ^{93}Nb peak (black line) interfering with a ^{93}Zr distribution (dashed, red line) can be reduced by choosing the window at the wing of the ^{93}Zr peak (right picture) instead of choosing it around the center of the ^{93}Zr peak (left picture). The yellow area represents the chosen window.

In addition, the ^{93}Nb peak can be shifted to even smaller bending by increasing the magnetic field of the GFM, so that it is stronger cut off by the entrance slit in front of the detector. But, due to the limited separation of ^{93}Nb and ^{93}Zr which can be achieved by adjusting the pressure in the GFM (see ch.4.2.4 and [46]) a considerable part of the ^{93}Zr events will also miss the entrance into the ionization chamber. This results in a

lower transmission similar to shifting the window to the left wing of the peak in the right picture of Fig. 7.4. In order to get an idea of how many orders we are able to suppress the isobaric background, we studied the rate of ^{93}Nb events detected by the ionization chamber at varying magnetic field, pressure in the GFM and charge state. Those rates were normalized to the rate of ^{94}Zr in the detector, to be independent of the current. The resulting ratios were all related to the ^{93}Nb rate of a measurement where a low magnetic field of 975 mT was chosen, so that the entire ^{93}Nb peak was located in the spectrum. The inverse of this ratio was called the ^{93}Nb suppression and is plotted on the logarithmic y-axis of Fig. 7.5 depending on the magnetic field of the GFM. The two different symbols represent the measurements with a kinetic energy of the ions of 198 MeV and 225 MeV. As it was expected from the formula for the

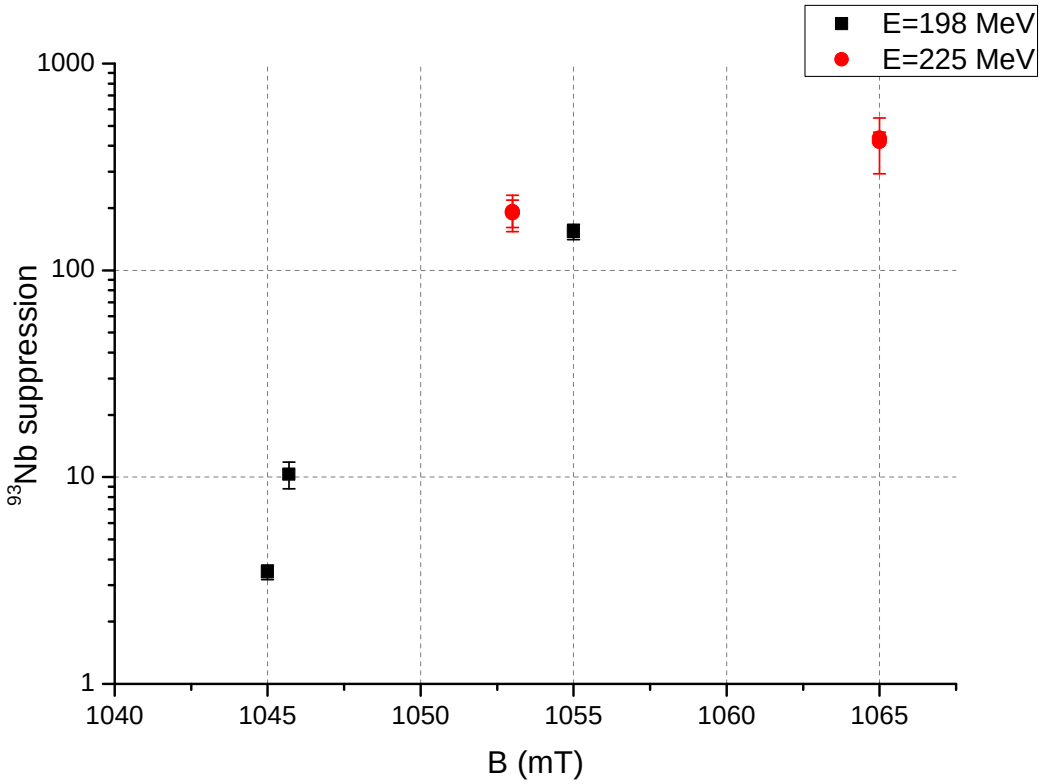

Figure 7.5.: The ^{93}Nb suppression in the ionization chamber is plotted depending on the magnetic field of the GFM for the an energy of 198 MeV and 225 MeV. For the interpretation of this data see text.

magnetic rigidity eq. (4.1) with increasing B-field, the center of the ^{93}Nb peak is shifted to smaller radii, so that a higher percentage of ions cannot pass the entrance slit to the ionization chamber resulting in a higher suppression of ^{93}Nb. However, the slope of the suppression seems to decrease at magnetic field above 1050 mT which suggests, that the maximum of the ^{93}Nb peak is already cut off by the aperture. In general, Fig. 7.5 suggests that the suppression is better for the higher energy of 225 MeV, which is not

readily understandable from theory. Inserting eq. (4.6) for the average charge state in eq. (4.1) leads to an expression for the magnetic rigidity which does not depend on the energy of the ions. However, if we look at Fig. 4.6, where the average charge state was calculated with the formula of sayer, an energy dependence of the magnetic rigidity can be noticed. But increasing the energy leads to a higher magnetic rigidity of the ions, which means that the radius of the trajectory in the magnet increases for a given magnetic field. This is in contrast to our observation, since a higher suppression of ^{93}Nb requires a smaller radius, so that the ^{93}Nb peak is stronger cut off by the slit.

It has to be mentioned, that in general the gas pressure in the GFM was not kept constant, which might be an explanation for the higher suppression for the ions with the higher energy. In this case, the gas pressure in the GFM was considerable higher, e.g. there was a different of 2 mbar between the black data point at B=1055 mT and the two red points at 1053 mT. Thus, we have a better separation from the expected position of ^{93}Zr (see [46]) on which the setup was adjusted. Furthermore, due to the higher density of the gas, we assume more angular straggling, which decreases the transmission into the ionization chamber. Hence, the better suppression for the red data points could be a consequence of the higher gas pressure in the GAMS and not of the higher energy. Higher energies of the ions are advantageous for the separation of the isobars (compare p.34-35).

For each pair of red data points at the same magnetic field, the gas pressure in the GFM was left unchanged. Here, the only varied parameter was the pressure in the detector which does not have, as expected, a significant influence on the ^{93}Nb suppression. The error bars contain two sources of uncertainties: On the one hand, the error of the number of events in the Gaussian distribution which was used to fit the ^{93}Nb peak and the instability of the count rate measured at the MCP, on the other hand, which was assumed to cause an uncertainty of 5% to the count rate. The total error of the suppression was calculated by quadratic error propagation. It has to be pointed out, that the initial ^{93}Nb peak which was used to estimate the unsuppressed ^{93}Nb count rate possibly includes ^{92}Zr events, since the TOF path was not used for this measurement. Consequently, the absolute value of the suppression might be smaller than it is shown in Fig. 7.5.

Similar to the experiment with the passive absorber, we wanted to derive an upper detection limit also for the measurements with the GAMS in order to compare the runs which were done with different parameters, i.e. different gas pressure and/or magnetic field in the GFM (p_{GFM}, B_{GFM}), charge state (q) and gas pressure in the ionization chamber (p_{det}). However, since we do not detect the entire ^{93}Nb distribution with the GAMS, we cannot proceed as described in ch. 6.3.3. to determine the transmission from the channel plate to the ionization chamber. The following approach enabled us to get a rough estimate of the transmission nevertheless.

The general idea was again to apply the windows for ^{93}Zr on the ^{93}Nb distribution but

to introduce a factor which takes into account the suppression. This means, we assume the 'virtual' ^{93}Zr distribution to be completely detected by the ionization chamber. This assumption is valid as long as the magnetic field of the GFM and the windows are chosen as it was done for Fig. 7.3, but if we go to higher magnetic fields, also the ^{93}Zr window is shifted to the right and thus, also ^{93}Zr ions are blocked by the entrance slit to the ionization chamber. This factor is called the GAMS factor and relates the number of detected events in the ionization chamber (N_{det}) to the events detected at the channel plate (N_{CP}):

$$G := \frac{N_{det}}{N_{CP}} \tag{7.2}$$

In contrast to the ^{93}Nb suppression considered in Fig. 7.5 the GAMS factor does not distinguish between the isotopes. Therefore, we cannot not tell if the count rate in the detector is lower than at the channel plate because ^{93}Nb events were pushed out of the spectrum or because ^{92}Zr events were suppressed. Consequently, it is assumed that the ^{93}Nb count rate is suppressed in the same way as the overall count rate. Of course, this leads to considerable uncertainties, which unfortunately cannot be estimated. Hence, an exact error analysis is not reasonable with the current data.

To obtain a transmission of the ^{93}Zr events, the ^{93}Nb events in the windows were additionally divided by the GAMS factor. With only a window on the TOF, to filter out events of m=93 amu, this method yielded a transmission between 20 % and 35 %. It is interesting, that the GAMS factor which is listed in the 6th column of Tab. 7.1 is smaller for a higher magnetic fields in the GFM which is opposite to the result for the ^{93}Nb suppression shown in Fig. 7.5. This could be explained by an increased suppression of the isotopes ^{92}Zr and ^{94}Zr in the case of higher B-fields. Apart from the application of the GAMS factor, the method to estimate the upper detection limit was identical to that described in the ch. 6.3.4. The corresponding results are also listed in Tab. 7.1 along with the relevant measurement parameters, the Zr count rate at the channel plate and the transmission for the final set of windows. Only measurements where an energy of 225 MeV was selected, were evaluated in this way, because the Constant Fraction Discrimators (CFD) with the resolution mentioned in ch. 7.1 were available for those TOF measurements only. Otherwise, the resolution of the TOF spectra was too low to apply resonable windows on the mass.

The concentration of ^{93}Nb in the ZrH_2 was estimated with the help of measurements with the injector magnet set to ZrH_2^- and ZrH_3^- and the ^{93}Nb peak was not suppressed in the ionization chamber. Thus, ^{92}Zr, ^{94}Zr and ^{93}Nb could be identified in the spectra, even without using the TOF path. However, the currents we could extract from the ion source were very small, i.e. approximately 1 nA at Cup 1. A ^{93}Nb/Zr ratio of $6 \cdot 10^{-5}$ was obtained. Since this result was calculated from only two measurements, the uncertainties are accordingly high.

In general, the resulting values for the upper detection limit are rather high, although

$\mathbf{B_{GFM}}$ (mT)	$\mathbf{p_{GFM}}$ (mbar)	**E(MeV)**	$\mathbf{p_{det}}$ (mbar)	$\mathbf{R_{CP}(Zr)}$ (Hz)	**G**	**T** (%)	$\mathbf{c(^{93}Zr)}$
1065	4.5	225	45.7	$1.21 \cdot 10^8$	$1.2 \cdot 10^{-3}$	1.50	$\mathbf{7 \cdot 10^{-7}}$
1065	4.5	225	48	$1.16 \cdot 10^8$	$1.1 \cdot 10^{-3}$	0.72	$\mathbf{2 \cdot 10^{-6}}$
1053	5.5	225	48	$6.20 \cdot 10^7$	$8.1 \cdot 10^{-4}$	1.58	$\mathbf{1 \cdot 10^{-6}}$
1053	5.5	225	45.7	$5.19 \cdot 10^7$	$8.3 \cdot 10^{-4}$	8.04	$\mathbf{3 \cdot 10^{-7}}$

Table 7.1.: Upper detection limit for ^{93}Zr (last column) along with the corresponding count rate of Zr at the CP (R_{CP}(Zr)), the transmission of the final set of windows (T), the Gams-factor (G), the gas pressure in the ionization chamber (p_{det}), the gas pressure in the GFM (p_{GFM}) and the magnetic field in the GFM (B_{GFM}).

those results must not be directly compared to results of the passive absorber or measurements where a standard sample was used to determine the transmission. In this first attempt, the windows were chosen asymmetrically around the expected maximum of ^{93}Zr. In case of the spectra listed in the second line in Tab. 7.1, it was not possible to choose the windows such, that they were free from background without reducing the transmission to zero. In order to calculate the upper detection limit, the error interval according to Feldman and Cousins considering the presence of background had to be used [74]. Thus, applying windows according to the right picture of Fig. 7.4 may cause an improvement. Since the transmission will drop considerably in this case, the samples have to be measured much longer at the same settings than it was done during this beamtime. It has to be mentioned, that without having measured a standard sample and having thus detected real ^{93}Zr events, the choice of windows is governed by a certain level of subjectivity.

However, since we proceeded in exactly the same way for the four measurements listed above, we can compare the results relative to each other. These results suggest, that using a lower magnetic field but a higher gas pressure in the GFM is more promising. Even though, the upper detection limit in the first line of Tab. 7.1 is quite similar, the transmission is considerably lower, which means that the window had to be chosen narrower in oder to obtain no counts. However, in case of the run in the 3rd line, no ^{94}Zr events were detected in the 5th segment of the anode, which means the ions were stopped before. Consequently, there was no separation in the E5 signal which caused the higher upper detection limit.

8. Conclusion and Outlook

Within this Master's Thesis, the detection of fission products by AMS has been tested for the first time using the example of ^{93}Zr, which is especially challenging due to its isobaric background in addition to the isotopic background. For this purpose, two different approaches were studied: On the one hand, we used a passive absorber to separate the isobaric background from the interesting events, which seemed to be very promising since we thus could achieve an upper detection limit of $6 \cdot 10^{-9}$, and on the other hand we did first experiments with the GAMS setup where we could efficiently suppress the isotopic background by adding TOF measurements. With the GAMS setup a preliminary upper detection limit of $3 \cdot 10^{-7}$ was obtained. However, those experiments have not been finished, yet. The GAMS measurements showed that we can suppress the isobaric background to approximately 0.16% of the initial ^{93}Nb count rate. From the performed simulations and measurements with the passive absorber the optimal material and thickness for the detection of ^{93}Zr ions at an energy of 190 MeV, i.e. 2.4 mg/cm^2 of silicon nitride, was determined. By comparing the stopping power of ^{93}Zr and ^{93}Nb from the simulations with those calculated with tables, a significant discrepancy was observed with our current data favoring the stopping power curves implemented in the simulation programs.

With the passive absorber, an upper detection limit was achieved, at which the ^{93}Zr events from the standard sample can be distinguished from the background. Consequently, the next step to develop this method further is to really detect ^{93}Zr counts to determine the transmission reliably. Especially for future investigations of sea water samples with regard to their ^{93}Zr concentration, we need to improve the detection limit even further, since we expect concentrations which are at least two order of magnitude lower. In the first place, we may increase the currents from the ion source, since we were well below the upper limit for the count rate in the ionization chamber. To avoid this upper limit which is given by the speed of the data acquisition and the charge collecting time, it is possible to use the surface-barrier-detector without the ionization chamber, since the measurements showed no enhancement of the upper detection limit if the ionization chamber is used (see ch.7.3.4). According to what we have learned from the simulations, Be foils would be a better choice as passive absorber material than silicon nitride if they could be produced very thin and highly uniform. Hence, Be foils from other producers should be tested.

In the case of the GAMS setup a run with a standard sample is necessary for a significant

determination of the upper detection limit, which should be done next. We have learned from those experiments done within the scope of this Master's thesis, that adding a TOF measurement to the usual measurements with the GAMS is essential to suppress the isotopic background. In order to keep the isotopic background extracted from the ion source as low as possible, it is proposed to extract Zr from the ion source using a molecule different from ZrH^- as ^{92}Zr and ^{94}Zr cannot be suppressed by WFI and WFII sufficiently and thus cause a considerable background. However, the possible candidate ZrF_4 is known to reduce the performance of the ion source and during the last beamtime using ZrO_2 we frequently observed electrical discharges in the ion source, whose origin still is not completely understood. We assume, that ZrO_2 which is electrically and thermally isolating, forms an isolating layer on the ionizer, which may explain the electrical discharges. Therefore, a thorough study of the behaviour of ZrO_2 in the ion source is recommendable. Furthermore, ZrC^- may also be a feasible candidate which should be tested.

Another idea is to combine both methods, the usage of a passive absorber and the GAMS setup. For this purpose, the passive absorber has to be installed in front of the GFM, which has to be evacuated, since the gas in the magnet further decreases the energy of the ions and increases the energy straggling. The energy difference of the isobars caused by the passive absorber leads to trajectories with different radii, which then can be distinguished by their position in the ionization chamber. We are aware of the fact, that we are limited by the position resolution of our ionization chamber. Another challenge is the focusing of the beam which has to be done by the beam guiding system, since the GAMS magnet itself is a dipole magnet and thus does not perform this task. Furthermore, if the magnet is evacuated, we have to select only one charge state which reduces the count rate of the radioisotope in the ionization chamber and thus increases the measuring time. As a first step, it is suggested to estimate the required position resolution before doing test experiments which would require changes to the setup. However, to be able to do this, we have to settle the question on the stopping power curves of ^{93}Zr and ^{93}Nb. This could be done by using the passive absorber setup in the Actinide beamline and detecting ^{93}Zr ions at different energies after having passed through a rather thin SiN foil to keep the error made by interpolating the energy loss linearly over the thickness of the foil as low as possible. The energy of the particles after the foil can be deduced from measuring the TOF.

List of Figures

List of Tables

Glossary

Notation	Description	
ADS	Accelerator Driven System	11
AGB	Asymptotic Giant Branch	20
AMS	Accelerator Mass Spectrometry	7
BMBF	Bundesministerium für Bildung und Forschung	7
FP	Fission Products	9
FR	Fast Reactor	11
FRMII	Forschungsreaktor München II	8
FWHM	Full Width at Half Maximum	28
GAMS	Gas-filled Analyzing Magnet System	30
GFM	Gas-filled Magnet	30
HF	Hydrofluoric Acid	16
HLW	High Level Waste	7
ILW	Intermediate Level Waste	7
LLFP	Long Living Fission Products	13
LLW	Low Level Waste	7
MA	Minor Actinides	12
MCP	Micro channelplate	35
MLL	Maier-Leibnitz-Laboratory	8
MOX fuel	Mixed Oxide fuel	12
MS	Mass Spectrometry	23
NPP	Nuclear Power Plants	9
P&T	Partitioning and Transmutation	13
RCM	Radiochemistry Munich	41

Notation	**Description**	
TOF	Time of Flight	30
TRAKULA	Transmutationsrelevante kernphysikalische Untersuchungen langlebiger Aktinide	7
TRU	Transuranic Elements	9
TUM	Technische Universität München	7
WF	Wien filter	29

Bibliography

[1] J.R.Maiorino. Accelerator driven system (ADS): An innovative reactor to be used as dedicated waste burner and a multipurpose neutron source. the status of the art. *INAC*, 2005.

[2] M.Keilhacker et al. Elektrizität: Schlüssel zu einem nachhaltigen und klimaverträglichen Energiesystem. Technical report, Deutsche Physikalische Gesellschaft, 2010.

[3] J.Magill et al. Impact limits of partitioning and transmutation scenarios on the radiotoxicity of actinides in radioactive waste. *Nuclear Energy*, 42(5), 2003.

[4] Strahlenschutz Bundesamt für Endlager Asse II - Aktueller Stand der Arbeiten zur Stabilisierung und sicheren Schließung. Technical report, Bundesamt für Strahlenschutz, 2010. urn:nbn:de:0221-201007142816.

[5] L.H. Baetsle. Application of partitioning / transmutation of radioactive materials in radioactive waste management. In *Workshop on Hybrid Nuclear Systems for Energy Production, Utilisation of Actinides and Transmutation of Long-lived Radioactive Waste*, 2001.

[6] K. Tuček. *Neutronic and Burnup Studies of Accelerator-driven Systems Dedicated to Nuclear Waste Transmutation.* PhD thesis, Royal Institute of Technology, KTH Stockholm, 2004.

[7] M.J.Salvatores. Physics and safety of transmutation systems. a status report. Technical Report 6090, OECD-NEA Report, 2006.

[8] Y.Kadi and J.P.Revol. Design of an Accelerator-Driven System for the Destruction of Nuclear Waste. In *Workshop on Hybrid Nuclear Systems for Energy Production, Utilisation of Actinides and Transmutation of Long-lived Radioactive Waste*, 2001.

[9] Z.Zhao. Status of Researches on Advanced Nuclear Energy System in China. In *Actinide and Fission Product Partitioning and Transmutation, Seventh Information Exchange Meeting Jeju, Republic of Korea*, October 2002.

[10] D.Warin. Status of the French Research Programme for Actinides and Fission Products Partitioning and Transmutation. In *Actinide and Fission Product Partitioning and Transmutation, Seventh Information Exchange Meeting Jeju, Republic of Korea*, October 2002.

[11] A.V.Lopatkin and V.V.Ignatiev. Overview of Current Russian Activities in P&T Area. In *Actinide and Fission Product Partitioning and Transmutation, Seventh Information Exchange Meeting Jeju, Republic of Korea*, October 2002.

[12] J.W.Herczeg. The Advanced Fuel Cycle Initiative: The Future Path for Advanced Spent Fuel Treatment and Transmutation Research in the United States. In *Actinide and Fission Product Partitioning and Transmutation, Seventh Information Exchange Meeting Jeju, Republic of Korea*, October 2002.

[13] V.McLane, C.L.Dunford, and P.F.Rose. *Neutron Cross Sections*, volume 2 - Neutron Cross Section Curves. Academic Press, INC., 1988.

[14] http://www-nds.iaea.org./exfor/exfor.htm, May 2011.

[15] C.Rubbia et al. Conceptual Design of a Fast Neutron Operated High Power Energy Amplifier. *CERN/AT/95-44 (ET)*, 1995.

[16] A.Stanculescu. IAEA Activities in the area of Partitioning and Transmutation. In *Actinide and Fission Product Partitioning and Transmutation, Seventh Information Exchange Meeting Jeju, Republic of Korea*, October 2002.

[17] Irish E.R. and W.H.Reas. The PUREX process - A Solvent Extraction Reprocessing Method for Irradiated Uranium. Technical report, Hanford Atomic Products Operation - General Electric, 1957.

[18] H.Takano and T.Ikegemi. Activities on R&D of Partitioning and Transmutation in Japan. In *Actinide and Fission Product Partitioning and Transmutation, Seventh Information Exchange Meeting Jeju, Republic of Korea*, October 2002.

[19] N.Müller-Hoeppe and R.Gauglitz. Ein neuer Ansatz zur Bewertung der Wirksamkeit von Barrieren im Endlager (02 E 9087) - Grundlage der Bewertung von Hydroxylapatit als chemische Barriere gegnüber Schwermetallen. Technical report, Deutsche Gesellschaft zum Bau und Betrieb von Endlagern für Abfallstoffe MBH (DBE), 1999.

[20] A.F.Holleman and E.Wiberg. *Lehrbuch der Anorganischen Chemie*. Walter de Gruyter, 1985.

[21] http://www.chemicool.com/elements/zirconium.html, July 2011.

[22] Accuratus. *Zirconium Oxide, ZrO2 Material Properties*, 2005.

[23] Alfa Aesar GmbH&Co KG, Postbox 11 07 65, 76057 Karlsruhe, Germany. *Sicherheitsdatenblatt Zirconium powder*, 2010.

[24] Lenntech BV - Water Treatment Solutions. *Zirconium - Zr.* Data sheet.

[25] ATI Wah Chang - Allegheny Technologies. *Reactor Grade Zirconium Alloys for Nuclear Waste Disposal*, 2003. Technical data sheet.

[26] C.M.Baglin. Nuclear Data Sheets, 2011.

[27] P. Cassette, F. Chartier, H. Isnard, C. Fréchou, I. Laszak, J.P. Degros, M.M. Bé, M.C. Lépy, and I. Tartes. Determination of 93zr decay scheme and half-life. *Applied Radiation and Isotopes*, 68(1):122 – 130, 2010.

[28] EVS Argonne National Laboratory, ˙Zirconium. Human Health Fact Sheet, August 2005.

[29] http://www-nds.iaea.org/sgnucdat/c1.htm#92-u-235.

[30] W.Koelzer. *Lexikon zur Kernenergie.* Forschungszentrum Karlsruhe GmbH, 2001.

[31] S.Häkkinen and P.B.Rhines. Decline of Subpolar North Atlantic Circulation During the 1990s. *Science*, 304(5670):555–559, 2004. published online: http://www.sciencemag.org/content/304/5670/555.short, 06.09.11.

[32] R.E.Moritz, C.M. Bitz, and E.J. Steig. Dynamics of Recent Climate Change in the Arctic. *Science*, 297(5586):1497–1502, 2002.

[33] R.Michel et al. Kartierung von Tc-99, I-129 und I-127 im Oberflächenwasser der Nordsee. Technical report, Bundesamt für Seeschifffahrt und Hydrographie (BSH), Zentrum für Strahlenschutz and Radioökologie, Risø-National Laboratory, Norwegian Radiation Protection Authority, Ion Beam Physics, Paul Scherrer Institute and ETH Zurich, 2008.

[34] G.Tagliente and the n_TOF Collaboration. The $^{92}Zr(n,\gamma)$ reaction and its implications for stellar nucleosynthesis. *Phys. Rev. C*, 81, 2010.

[35] http://www.kadonis.org/, May 2011.

[36] K. Knie, G. Korschinek, T. Faestermann, E. A. Dorfi, G. Rugel, and A. Wallner. ^{60}Fe Anomaly in a Deep-Sea Manganese Crust and Implications for a Nearby Supernova Source. *Phys. Rev. Lett.*, 93:171103, Oct 2004.

[37] C.Tuniz, J.R.Bird, D.Fink, and G.F.Herzog. *Accelerator Mass Spectroscopy - Ultrasensitive Analysis for Global Science*. CRC Press, 1998.

[38] L.K.Fifield. Accelerator mass spectrometry and its applications. *Rep. Prog. Phys.*, 62:1223–1274, 1999.

[39] D.Fink. AMS-11 in Rome, 2008: Past achievements, current and future trends. *Nucl. Instrum. Methods B*, 268, 2010.

[40] R.Middleton. A versatile high intensity negative ion source. *Nucl. Instrum. Methods*, 1982.

[41] G.Rugel, W.Assmann, I.Dillmann, T.Faestermann, G.Korschinek, J.Lachner, M.Poutivtsev, and M.Schubert. A Modified Negative Ion Sputter Source for AMS and its Efficiency for Plutonium. *Maier-Leibnitz-Laboratorium - Annual Report*, 2008.

[42] G.Rugel. *Retrospektive Bestimmung der Fluenz schneller Neutronen in Hiroshima*. PhD thesis, Ludwig-Maximilians-Universität zu München, 2002.

[43] H.D.Betz. Charge States and Charge-Changing Cross-Sections of Fast Heavy Ions. *Rev.Mod.Phys.*, 44:500–523, 1972.

[44] P.Ludwig. Search for Superheavy Elements in Nature with Accelerator Mass Spectrometry. Master's thesis, TUM, 2010.

[45] R.O.Sayer. Semi-empirical formulas for heavy-ion stripping data. *Revue de Physique Appliquée*, 1977.

[46] K.Knie. *Beschleunigermassenspektroskopie mit Isobarenseparation in einem dedizierten gasgefüllten Magneten*. PhD thesis, Technische Universität München, 1996.

[47] R.Lutter, O.Schaile, K.Schöffel, K.Steinberger, P.Thirolf, and C.Broude. MARABOU - A MBS abd ROOT Based Online/Offline Utility. http://www.bl.physik.uni-muenchen.de/marabou/html/.

[48] J.Lachner. Suche Nach Primordialen Radionukliden Mittels Beschleunigermassenspektroskopie. Master's thesis, Technische Universität München, 2008.

[49] G.F.Knoll. *Radiation Detection and Measurement*. John Wiley & Sons, 2 edition, 1989.

[50] J.Neuhaus, I.Lommatzsch, and A.Voit, editors. *Experimental facilities - Forschungs-Neutronenquelle Heinz Maier-Leibnitz (FRMII)*. Board of Directors,

Forschungs-Neutronenquelle Heinz Maier-Leibnitz (FRMII), Technische Universität München, 2011. www.frm2.tum.de/wissenschaftliche-nutzung/experimental-facilities-buch/index.html, 31.08.2011.

[51] S.F.Mughabghab. Thermal Neutron Capture Cross Sections, Resonance Integrals and g-Factors. Technical report, International Nuclear Data Commitee (IAEA), February 2003.

[52] G.Pfennig, H.Klewe-Nebenius, and W.Seelmann-Eggebert. Karlsruher Nuklidkarte. Forschungszentrum Karlsruhe GmbH, 1998. 6. edition.

[53] R.Middleton. A negative-ion cookbook. www.pelletron.com/cookbook.pdf, 13.01.11, 1990.

[54] R.Annou and V.K.Tripathi. Femtosecond laser pulse induced Coulomb explosion. *arXiv:physics*, 2005. http://arxiv.org/abs/physics/0510014, 13.10.2011.

[55] C.Vockenhuber et al. Development of isobar separation for ^{182}Hf ams measurements of astrophysical interest. *Nucl. Instrum. Methods Phys. Res. B*, 2007.

[56] N.Bohr. On the theory of the decrease of velocity of moving electrified particles on passing through matter. *Phys. Mag. Series 6*, 25(145), 1913.

[57] N.Bohr. On the decrease of velocity of swiftly moving electrified particles in passing through matter. *Phys. Mag. Series 6*, 30(178), 1915.

[58] N.Bohr. The Penetration of Atomic Particles Through Matter. *Mat. Fys. Medd. Dan. Vid. Selsk*, 18(8), 1948.

[59] J.Lindhard, M.Scharff, and H.E.Schiott. Range Concepts and Heavy Ion Ranges. *Mat. Fys. Medd. Dan. Vid. Selsk*, 33(14), 1963.

[60] J.Lindhard and M.Scharff. Energy loss in matter by fast particles of low charge. *Mat. Fys. Medd. Dan. Vid. Selsk*, 27(15), 1953.

[61] P.Sigmund. *Stopping of heavy ions: A theoretical approach*. Springer Verlag, 2004.

[62] J.F.Ziegler, J.P.Biersack, and U.Littmark. *The Stopping and Range of Ions in Solids*, volume 1. Pergamon Press, 1985. More information on http://www.srim.org/#SRIM.

[63] L.C.Northcliffe and R.F.Schilling. *Range and Stopping-Power Tables for Heavy Ions*, volume 7. Academic Press, Inc., 1970.

[64] W.Brandt and M.Kitagawa. Effective stopping-power charges of swift ions in condensed matter. *Phys. Rev. B*, 25(9), 1982.

[65] L.C.Northcliffe. Energy Loss and Effective Charge of Heavy Ions in Aluminum. *Phys. Rev.*, 120:1744–1757, 1960.

[66] P.Sigmund. Low-speed limit of Bohr's stopping power formula. *Phys. Rev. A*, 54(4), 1996.

[67] C.Leroy and P.-G.Rancoita. *Principles of Radiation Interaction in Matter and Detection.* World Scientific Publishing Co. Pte. Ltd, 2004.

[68] J.E.Turner. *Atoms, Radiation, and Radiation Protection.* WILEY-VCH Verlag GmbH&Co KGaA, 3 edition, 2007.

[69] W.K.Chu. Calculation of energy straggling for protons and helium ions. *Phys. Rev. A*, 13(6), 1976.

[70] Q.Yang and D.J.O'Connor. Empirical formulae for energy loss straggling of ions in matter. *Nucl. Instrum. Methods B*, 61:149–155, 1991.

[71] F.Besenbacher, J.U.Andersen, and E.Bonderup. Straggling in Energy Loss of Energetic Hydrogen and Helium Ions. *Nucl. Instrum. Methods*, 168, 1980.

[72] F.Schiettekatte. Fast Monte Carlo for ion beam analysis simulations. *Nucl. Instr. and Meth. B*, 266(8), 2008.

[73] Privat communication, email from J. Ziegler, 31.05.2011.

[74] G.J.Feldman and R.D.Cousins. A Unified Approach to the Classical Statistical Analysis of Small Signals. *Phys. Rev. D*, 57(7), 1998.

[75] G.Rugel et al. Measurement of the Activation Product ^{93}Mo via AMS. Technical report, Maier-Leibnitz-Laboratory - Annual Reports, 2007.

A. Acknowledgments

This last section is dedicated to all the people who made it possible that I could write and finish this thesis. I would like to thank the following people in particular because they supported me in many ways.

- Thomas Faestermann and Gunther Korschinek for offering the opportunity to work on this exciting subject. Your assistance and your knowledge about the setup, theory, electronics and... was extremely helpful. I also appreciated the intense discussions with both of you about beamtime results and other issues. I especially want to thank you, Gunther, for helping me to focus on the essential questions.

- Georg Rugel, for his thorough introduction to AMS and the setup at the MLL, his commitment during the beamtimes, for answering all my questions (sometimes even twice) and for introducing me to the AMS group in the first place. It's a pity, that you left...

- Leticia Fimiani and Peter Ludwig, for the pleasant working atmosphere even late in the night, for being always available for answering questions and for supporting me in so many ways. I really enjoy working with you!

- Florian Kraus and Sebastian Baer from the anorganic chemistry chair who spend a whole day to help me preparing the standard sample and who tried to familiarize me with HF.

- Rudi Lutter and Otto Schaile for helping with computer and especially root problems.

- The operators, for their help during the difficult Zr beamtimes. Especially, Peter Ring for not giving up to get at least some pA of Zr to C1.

- Walter Carli for his help with the 3rd WF.

- My family and David Herrmann, for their private support, their confidence in me, their sympathy and their understanding when I came home in a bad temper, because things didn't work as they should.